Influence of Electrode Formulation in Silicon Microparticle Electrodes for Lithium-Ion Batteries

by

Anita Li

A dissertation submitted in partial fulfillment
of the requirements for the degree of
Doctor of Philosophy
(Materials Science and Engineering)
in the University of Michigan
2023

Doctoral Committee:

Professor Alan I. Taub, Chair
Professor Yang-Tse Cheng, University of Kentucky
Assistant Professor Yiyang Li
Professor Wei Lu

Anita Li

luonga@umich.edu

ORCID iD: 0000-0002-4751-416X

Dedication

To anyone who endeavors to learn something new – this thesis will likely be of only very little help (if any). Instead, I'd like to share with you these two Bible verses, which I am confident will be of great help as they have been to me in my life.

Trust in the LORD with all your heart,
and do not lean on your own understanding.
In all your ways acknowledge him,
and he will make straight your paths

Proverbs 3:5-6 (English Standard Version)

Oh, the depth of the riches and wisdom and knowledge of God! How unsearchable are his judgments and how inscrutable his ways!

"For who has known the mind of the Lord,
Or who has been his counselor?"
"Or who has given a gift to him
That he might be repaid?"

For from him and through him and to him are all things. To him be the glory forever. Amen.

Romans 11: 33-36 (English Standard Version)

Acknowledgements

My PhD has surely not been a solitary journey. This dissertation would not be possible without all the people who have helped, encouraged, and supported me along the way, and I am incredibly thankful for every one of them

To **Alan Taub**, my research advisor, without whom I would surely not be where I am today. Contrary to the innumerable, terrifying, and intimidating stories I heard about him from nearly every GM colleague who ever had to endure a Red Team Review, Professor Taub turned out to be an unfailingly encouraging and supportive advisor. There is not a part of my research mind that has not been shaped by him, and I am ever-grateful for that. I am honored to be his first non-traditional PhD student.

To my many colleagues **GM Fuel Cell** and **GM R&D**, who through their everyday example, taught me so much and helped me to grow as an engineer and a researcher.

To **Nicole Ellison**, **Bradley Frieberg**, **Mike Balogh**, **Bob Conell**, **Xiaosong Huang**, **Jiazhi Hu**, and **Lei Wang**, who have each invested their time and energy to help get me started in field of silicon anodes, enabling me to become a functional and capable researcher.

To **Jeff Rock** and **Yeh-Hung Lai**, for their mentorship and the many ways they have helped me grow as an engineer. I am so grateful that they always made time to answer my questions and to teach me about mechanics and mechanical engineering design.

To **Bill Osad**, **Andy Galant**, and **Craig Grunewald**, who with their ingenuity, breadth of knowledge, and diligence have helped immensely to get, and more importantly, keep things running in the lab.

To **Craig Gittleman** and **Mark Mathias** for taking a chance on me and giving me the opportunity to pursue my PhD while working at General Motors.

To **Yang-Tse Cheng**, who has an inexhaustible enthusiasm for materials science and who has kindly pointed me in the right direction countless times throughout my PhD journey.

To **Jacob Hempel**, for his mastery in AFM techniques and for sharing in this PhD journey with me. I am so glad we met!

To **Katharine Beach**, **Jorge Barreda**, **Nancy Senabulya**, **Tao Ma**, **Bobby Kerns**, **Tony Chinnici**, and **Jeff Williams**, who willingly and generously gave their time to teach me and help me, even though those projects did not work out as planned.

To the Taub Lab group, with whom I have shared great camaraderie: **Wes**, **Yipeng**, **Avi**, **Maya**, **Caleb**, **Aaron**, **Xun**, **Jay**, **Ankush**, **Anshul**, **Amy**, **Aaron**, **Randy**, **Daney, Kanat**, **Jon**, **Jaime**, **Loulou**. They say your lab mates are like your academic brothers and sisters – I could not have asked for better academic siblings.

To **Yiyang Li**, for always saying hi to me at seminars and department events, for his helpful suggestions on this dissertation, and for his honest perspectives on life in academia.

To **Wei Lu**, for his willingness to serve on my committee and his helpful questions.

To **Renee Hilgendorf**, who has kindly and patiently shepherded me through this graduate program.

To **Ellen Kampf**, who is the only one who knows where Taub will be on any given workday and who far exceeds her job responsibilities to keep our lab group (and all our research institutes) running.

To my many Ann Arbor friends. If I were to name every person, and the reasons I am thankful for them, I would need to add another appendix to this dissertation.

Bruna Scheuher, Shannon Qin, Elaine Liu, Grace Haeun Lee, Nancy Wu, Maria Kim, Emily Ahn, Chelsea Reighard, Hope Schaeffer, Sara Timberlake, Jasmine Jones, Jessica Jones, for being great listeners and great encouragers. **James Tan**, for enriching my life in so, so, SO many ways. **Marissa Linne** for welcoming me to MSE at Michigan and to the Ann Arbor climbing community. **Alan Chien** and **Emily Chang**, for the many belays. **Tianjiao Lei**, for being my first MSE homework buddy. **John Wang, Troy Zhu, Josh Cheng, Joel Tan, Sam Chen, Mark Dong, Jay'de Degraffinried, Torre Puckett, Zach Fritts, Michelle Tang, Steve and Joy Hwang, Peter Sun, Jessica Kim, Junshik Kim, Brian Purnomo, Dominic Caballero, Hee Sung Kim and Dorcas Choo, Brandon Woo, Grace Song, Michael Lee, Grace Chen, Esther Lee, Liz Choe**, and so, so, so many more. You all have made Ann Arbor home to me.

To my family: **my parents**, who love me and have supported me in my every endeavor. I treasure your words of wisdom. **Alina**, who is the funniest person I know. My **grandma**, for driving me everywhere when I was a kid and for showing me how strong and capable grandmas can be! And my **Aunt Nu**, for spoiling me with all her delicious food every time I visit home. I am thankful for my entire family – for all the joyfulness and color they have brought into my life.

To **Peter Li**, my husband and the love of my life. He is my greatest supporter and my greatest motivation to finish this dissertation.

Table of Contents

Dedication ii

Acknowledgements iii

List of Tables x

List of Figures xi

List of Appendices xv

Abstract xvi

Chapter 1 Introduction 1

1.1 Discovery and Development of Silicon Battery Electrodes 2

1.1.1 Nano- vs. Micro- Silicon Particles 4

1.2 Electrode Formulation 4

1.2.1 Development of Binder Chemistries for Silicon Anodes 6

1.2.2 Conductive Additive Morphologies 8

1.3 Development Targets and Current Status 10

1.4 Dissertation Scope 12

Chapter 2 Effect of Binder Content 14

2.1 Introduction 14

2.2 Experimental Methods 16

2.2.1 Electrode Preparation and Cell Construction 16

2.2.2 Electrochemical Testing 18

2.2.3 Porosity Measurement 18
2.2.4 Electrical resistivity measurements 19
2.2.5 Mechanical Testing 19
2.2.6 Scanning Electron Microscopy 20
2.2.7 X-ray Diffraction 20
2.2.8 Atomic Force Microscopy 20
2.3 Results 21
2.3.1 Pristine Electrode Properties 21
2.3.2 Electrochemical Performance 25
2.3.3 Post-Mortem Analysis 29
2.4 Discussion 34
2.4.1 Initial Lithiation 34
2.4.2 Cycling and Capacity Retention 35
2.4.3 Rate Testing 37
2.5 Conclusions 38
Chapter 3 Influence of Conductive Additive Content 40
3.1 Introduction 40
3.2 Methods 42
3.2.1 Electrode Preparation 42
3.2.2 Porosity Measurement 43
3.2.3 Scanning Electron Microscopy (SEM) 43
3.2.4 Electrical Conductivity 43
3.2.5 Mechanical Testing 45

3.2.6 Electrochemical Testing 45

3.2.7 X-ray diffraction (XRD) and Atomic Force Microscopy (AFM) 46

3.3 Results 46

3.3.1 Electrode Structure 46

3.3.2 Pristine Electrode Properties 48

3.3.3 Electrochemical Performance 50

3.3.4 Post-Mortem Analysis of Silicon Utilization 52

3.4 Discussion 54

3.4.1 Mechanical Behavior 55

3.4.2 Fast-Charge Capability 56

3.4.3 Cycle Life Performance 58

3.4.4 Silicon Utilization 60

3.5 Conclusions 61

Chapter 4 Magnetic Force Dilatometry of Silicon-NMC622 Lithium-Ion Coin Cells – the Effects of Binder, Capacity Ratio, and Electrolyte Selection 64

4.1 Introduction 64

4.2 Methods 68

4.2.1 Electrode preparation and coin cell fabrication 68

4.2.2 Electrochemical Test Procedures 70

4.2.3 Magnetic Dilatometry 70

4.3 Results 74

4.3.1 Binder Content vs. Cell Expansion 78

4.3.2 Capacity Ratio vs. Cell Expansion 79

4.3.3 Binder Selection and Electrode Formulation vs. Cell Expansion 81

4.3.4 Electrolyte Selection vs. Cell Expansion 81

4.4 Discussion 84

4.4.1 Influence of Binder Content on Cell Expansion 85

4.4.2 Influence of Capacity Ratio on Cell Expansion 86

4.4.3 Influence of Binder Chemistry and Electrode Formulation on Cell Expansion 86

4.4.4 Influence of Electrolyte Selection 87

4.4.5 Influence of Cell Expansion on Volumetric Energy Density 89

4.5 Conclusions 90

Chapter 5 Conclusions and Future Work 93

5.1 Summary 93

5.2 Future Work 96

5.2.1 Measuring Lithium-Ion Diffusion through Polymeric Binders 96

5.2.2 Understanding Degradation Mechanisms 96

5.2.3 Understanding Cell Expansion 97

5.2.4 Emphasizing Development of High-Throughput Characterization Techniques 98

Appendices 99

Bibliography 109

List of Tables

Table 1: Energy density of three lithium-ion anode materials.....1

Table 2: Summary of Silicon Electrodes with Polyimide Binder in Literature.....8

Table 3: Brief Literature Review of Functional Capacity vs. Cycle Number for Silicon-Containing Lithium-Ion Anodes, to Capture Functional Capacity of Electrodes after Extended Cycling.....11

Table 4: Electrode formulations utilized to study effect of binder content.....17

Table 5: Electrode formulations used in the Conductive Additive Content study.....42

Table 6: Minimum voltages and plated capacities during half-cell lithiation to 1500 mAh gSi-1 53

Table 7: Comparison of fracture toughness and peel force ranges measured in this and previous work.....55

Table 8: Electrode Formulations for Cell Expansion Study.....69

Table 9: Electrolyte Compositions for Cell Expansion Study.....69

Table 10: Cell Configurations for Cell Expansion Study.....70

Table 11: Pristine cell thicknesses, to, cell thicknesses after formation, t3, and the difference in cell thickness between those points, Δt, for the cell configurations studied in this work.....77

Table 12: Pristine electrode coating thicknesses, to, electrode coating thicknesses at end-of-test, tEOT, and the difference in electrode thickness between these points, Δt.....77

List of Figures

Figure 1. Schematic of composite silicon electrode cross-section 5

Figure 2. Secondary electron scanning electron micrograph of a composite silicon electrode. 6

Figure 3. Plot of cycle number vs functional capacity loadings as reported in literature. Performance of the electrodes from in this work is denoted by the orange triangle (1 x PI formulation) and magenta circle (3 x PI formulation) symbols. The red X denotes the USABC target for 2025 production. 12

Figure 4. SEM images of 1/3 x PI (left column), 1 x PI (middle column), and 3 x PI (right column) electrodes in their pristine state (top row), after formation in the delithiated state (middle row), and after 50 cycles in the delithiated state (bottom row). The scale bar applies to all images. 22

Figure 5. Isolated and connected porosity of pristine electrodes for each formulation (n = 3). ... 23

Figure 6. SEM of scratched surfaces on the electrodes. 23

Figure 7. (a) Fracture toughness from scratch tests and ($n \geq 3$) and (b) peel force from 180° peel tests on pristine electrodes of each formulation ($n \geq 5$). 24

Figure 8. Typical peel strength vs peel length curves. 25

Figure 9. Electrical conductivity of pristine electrodes with varying binder content (n = 3). 25

Figure 10. (a) Discharge capacity per gram of silicon and (b) coulombic efficiencies for electrodes with varying binder content, cycled at C/5 (n = 3). A close-up of the coulombic efficiencies for the first ten cycles is provided in the bottom right plot. 26

Figure 11. Initial coulombic efficiency (left), initial discharge capacity after formation (middle), and number of cycles to 80% capacity retention (right) for cells with varying binder content. 27

Figure 12. Charge voltage profiles for electrodes with varying binder content: (a) 1st formation cycle, (b) 1st cycle after formation, (c) 100th cycle, and (d) 200th cycle. 28

Figure 13. (a) Constant current charge capacity vs. cycle during rate testing, with charge rates listed across the top of the chart and (b) semi-log plot of charge capacity vs. C-rate (n = 3). 29

Figure 14. Typical XRD spectra on pristine and cycled electrodes with varying binder contents. 30

Figure 15. (a) Discharge capacity and (b) silicon amorphization after the 1st formation cycle and after 50 cycles for electrodes with varying binder content. (n ≥ 2).....31

Figure 16. Calculated capacity of the amorphized silicon after formation in electrodes with varying binder contents. Error bars represent the propagated error from XRD and discharge capacity measurements.....32

Figure 17. The left column contains AFM pull-off adhesion maps and right column contains PFTUNA maps of cycled electrodes: (top) 1 x PI electrode after 100 cycles, (middle) 3 x PI electrode after 50 cycles, and (bottom) 1/3 x PI electrode after 50 cycles.....33

Figure 18. Comparison between SEM and AFM imaging on a cross-section of a 1x PI electrode after 100 cycles. Top row: SEM of imaged area on electrode cross-section. Bottom row: (left) AFM topography map (middle) pull-off adhesion map and (right) PFTUNA map.....33

Figure 19. Electrode capacity (a) (left axis) and capacity retention (right axis) and gravimetric energy density of the electrode (b) vs. binder content.....39

Figure 20. Bode plot of real impedance during PEIS on electrodes with varying GNP content...44

Figure 21. Bode plot of real impedance during potentiostatic electrochemical impedance spectroscopy (PEIS) of the 10 vol% GNP electrodes at various voltage amplitudes. Note the y-axis scale compared to Figure 20.....44

Figure 22. Bode plot of phase angle during PEIS on electrodes with varying GNP content. 45

Figure 23. Total porosity (a) and thickness (b) of electrodes with varying conductive additive content. 47

Figure 24. Secondary electron SEM images of cross-sections of pristine electrodes with 10 (a) and 25 (b) vol% GNP, showing more preferential stacking of GNP in the latter than the former electrode.....47

Figure 25. Electrode conductivity of electrodes with various conductive additive content.....48

Figure 26. Photographs of peel test surfaces in electrodes with varying GNP content. Peeled area is denoted by the curly bracket.....49

Figure 27. Peel force (a) and fracture toughness from microscratch (b) tests. 49

Figure 28. Peel force comparison between two electrodes of the same formulation. 50

Figure 29. Discharge capacities in C/3 cycle life testing for electrodes with ≤ 10 vol% GNP (a) and ≥ 10 vol% GNP (b) 50

Figure 30. Coulombic efficiency during C/3 cycle life testing for the first 10 cycles (a) and cycles 1 to 200 (b) for electrodes of varying GNP content. 51

Figure 31. Initial coulombic efficiency (a), initial discharge capacity (b), and number of cycles to 80% capacity retention (c) in the C/3 cycle life test of electrodes with varying conductive additive content. 51

Figure 32. Constant current charge capacity in fast charge testing for electrodes with ≤ 10 vol% GNP (a) and ≥ 10 vol% GNP (b). 52

Figure 33. Voltage profiles of the first 2C charge for one cell of each level of GNP content. 52

Figure 34. Initial coulombic efficiencies of half cells lithiated to 1500 mAh gSi-1 in electrodes with varying GNP content. 54

Figure 35. Percentage silicon amorphization after lithiating to 1500 mAh g_{Si}^{-1} (a) and cell voltage after open circuit rest after lithiation (b) in electrodes with varying GNP content. Error bars represent standard deviation. 54

Figure 36. Total gravimetric energy density of electrodes with varying GNP content after 3 and 200 cycles. 60

Figure 37. Photograph of magnetic dilatometer for coin cells. Photograph by W. Osad (GM R&D), May 3, 2023 71

Figure 38. Schematic of magnetic dilatometry test hardware (a) before and (b) after cell expansion. Force is inversely related to the distance between the magnetic components; therefore, if $x_1 < x_2$, then $f_1 > f_2$. 71

Figure 39. Illustration of reversible (a) and irreversible (b) expansion. 73

Figure 40. Comparison of coin cells with austenitic (conventional) and ferritic spacers. Coin cells were otherwise the same. Cells with Y2 electrolyte (a). Cells with C1 electrolyte (b). Cells with B1 electrolyte (c). 75

Figure 41. Position of the ferritic spacer vs. time. Positions are zeroed at the cell thickness at the start of C/3 cycling. 75

Figure 42. Stacked plots showing synchronization between cell cycling and cell expansion. Cell #1 of the PAN electrode cells (left) and cell #1 of the B1 electrolyte cells (right). 76

Figure 43. Discharge capacity (a), % reversible expansion scaled by discharge capacity (b), % irreversible expansion vs. cycle (c), and % irreversible expansion vs. cumulative irreversible capacity (d) for the 1 x PI and 3 x PI cells. 79

Figure 44. Discharge capacity (a), % reversible expansion scaled by discharge capacity (b), % irreversible expansion vs. cycle (c), and % irreversible expansion vs. cumulative irreversible capacity (d) for the 1 x PI cells at N/P = 2.00 and N/P = 1.50. 80

Figure 45. Voltage drop during the 15-minute OCV rest after charging and before discharging vs. cycle count for the 1 x PI electrodes with Y2 electrolyte at N/P = 2.00 and N/P = 1.50. 80

Figure 46. Discharge capacity (a), % reversible expansion scaled by discharge capacity (b), % irreversible expansion vs. cycle (c), and % irreversible expansion vs. cumulative irreversible capacity (d) for the 1 x PI and PAN cells at N/P = 1.5 81

Figure 47. Discharge capacity (a), % reversible expansion scaled by discharge capacity (b), % irreversible expansion vs. cycle (c), and % irreversible expansion vs. cumulative irreversible capacity (d) for the 1 x PI cells with Y2, C1, and B1 electrolytes. 82

Figure 48. Reversible expansion, in microns, vs. cycle. 83

Figure 49. Irreversible expansion, in microns, vs. cycle. 84

Figure 50. Volumetric energy density vs. cycle for cell configurations tested in this study 89

Appendix Figure 51. TEM image of silicon wafer that was lithiated in a coin cell and delithiated prior to imaging. Top layer = capping layer, middle layer = amorphized silicon (previously lithiated region), bottom layer = crystalline silicon wafer 108

List of Appendices

Appendix A: Calculation of Theoretical Binder Layer Thickness..... 100

Appendix B: Definition of Cell Expansions for Calculation of True Energy Density..... 101

Appendix C: Additional Details on Data Calibration and Processing Procedures for Magnetic Dilatometry..... 102

Appendix D: Connected Electrode Porosity Calculation..... 105

Appendix E: Toward Measurement of Lithium-Ion Diffusion Coefficients in Thin Film Polymeric Binders..... 107

Abstract

Commercialization of silicon anodes could be a critical step towards increasing electric vehicle adoption among consumers. Silicon has the potential for three times the volumetric capacity, ten times the gravimetric capacity, are more amenable for fast-charge, and can be made using similar manufacturing processes as the incumbent, widely commercialized graphite anodes. To achieve such high capacities, silicon forms amorphous alloys with lithium during lithiation. To accommodate the alloying lithium, the silicon will expand up to three times its original volume, kicking off a cycle of degradation involving particle cracking and irreversible solid electrolyte interphase growth. Although nanosizing or nano-structuring can circumvent this degradation pathway, nanomaterials are not suitable for near-term commercialization due to high material cost and safety concerns. Therefore, to meet battery cell cost targets of $75/kWh, development efforts have shifted towards improvement of microparticle silicon electrodes.

Many milestones in the development of silicon anodes were enabled by breakthroughs in electrode formulation. The most prominent of these have been the advancements in binder chemistry and conductive additive integration. Comparatively few studies are devoted to understanding the influence of electrode formulation – the relative ratios of electrode components – on electrode properties and performance.

This thesis examines the influence of formulation on structure-properties-performance relationships in silicon microparticle electrodes for lithium-ion batteries. We track how formulation affects porosity, mechanical properties, and electrical conductivity, and identify correlations between these characteristics and electrochemical performance. Full cells with industrially relevant capacity loadings (4.5 mAh cm^{-2} at beginning of life) were evaluated using three critical performance metrics: fast-charge capability, capacity retention, and gravimetric

energy density. We build upon the literature by utilizing diffraction techniques to detect silicon amorphization, thus utilization, and understand how this is affected by formulation and cycling.

We also utilize first-of-its-kind operando magnetic dilatometry to explore the effects of formulation, capacity ratio, and electrolyte selection on cell expansion in coin cells. We track reversible and irreversible cell expansions. Our measurements reveal that reversible expansions scale with cell discharge capacity and are most sensitive to the mechanical properties of the electrode. Meanwhile, irreversible expansions are a symptom of cell degradation mechanisms, with electrolyte composition showing the strongest influence. Ultimately, these measurements shed light on how volumetric energy density evolves with cycling—an important metric for battery integration.

The insights gained through the course of this work are expected to inform continued electrode and cell optimizations, guide definition of product specifications for commercialization, and serve as a catalyst for future research and development of silicon anode electrodes for lithium-ion batteries.

Chapter 1 Introduction

Consumer demand for battery electric vehicles (BEVs) is rapidly increasing[1,2]. In response, battery manufacturers are planning a ten-fold increase in battery plant capacity in North America over the next ten years, particularly concentrated along the I-75 corridor[1]. Although the demand is increasing, three main barriers prevent widespread consumer adoption of battery-electric vehicles: range, charge time, and cost[1–4]. Since the introduction of electric vehicles, significant improvements have been made. From 2010 to 2020, the sales-averaged all electric range for BEVs increased from 75 to 290 miles[1]. Charging times have decreased from >10 hours to 30 minutes, under certain conditions, for 200 miles of range[5]. However, the price of BEVs has steadily remained above that of internal combustion engine (ICE) vehicles[1,4]. In 2020, the sales-weighted average price of a BEV was $55,000, while the average expenditure for an ICE light-duty vehicle was only $40,000[1].

One moderate-risk cost-reduction strategy is to shift the anode electrode active material from graphite to silicon. Unlike in graphite, where lithium-ions intercalate between the carbon layers, silicon is an alloying anode, forming a compound with silicon during lithiation, thus resulting in a significant advantage in energy density[6,7]. The maximum lithium stoichiometry in graphite is C_6Li, while approximately $Li_{4.4}Si$ in silicon.

Table 1: Energy density of three lithium-ion anode materials

Anode Material	Gravimetric Capacity ($mAh\ g^{-1}$)	Volumetric Energy Density ($Wh\ mL^{-1}$)
Graphite (LiC_6)	372	2.7
Silicon ($Li_{15}Si_4$)	3579	4.7
Lithium	3860	---

*Calculated at 100% volume expansion vs. 3.75 V cathode; assumed graphite = 10% volume expansion at full lithiation and silicon = 300% volume expansion at full lithiation[7].

Other advantages to silicon are its earth-abundance[8] and potential for fast-charge[5]. For electric vehicle consumers, these properties could translate to reduced vehicle mass, reduced battery pack volume (more vehicle design flexibility), reduced vehicle cost, increased energy efficiency, increased vehicle range, and faster charge times. When paired with a high-capacity, high-voltage cathode, such as nickel-rich nickel manganese cobalt oxides, early cost projections estimate that the cell cost could reach < $125/kWh[9,10]. Moreover, silicon could be a drop-in replacement for graphite, as silicon electrodes can be produced using the same manufacturing processes as graphite, thereby significantly reducing the capital investment required to make the swap.

However, significant challenges must be solved before silicon-dominant anode electrodes can be commercialized—namely poor cycling stability and poor calendar life[11]. Silicon and lithiated silicon surfaces are inherently very reactive in the presence of liquid electrolytes, especially at low voltages, which increase the driving force for electrolyte side-reactions. When new silicon surface is exposed due to lithiation volume expansion, electrolyte side reactions can occur and result in degradation of the electrode performance via electrolyte depletion, resistance buildup, and pore clogging. Because of these issues, electric vehicle OEMs have yet to commercialize silicon-dominant anodes in BEVs. However, the potential benefits of silicon remain alluring and continue to attract great research attention and catalyze major investments in a plethora of start-up companies[12–14].

1.1 Discovery and Development of Silicon Battery Electrodes

The feasibility of using silicon as a reversible alloying anode material was first demonstrated by Sharma and Seefurth at General Motors in 1976[15,16]. At this stage, lithiation and delithiation of silicon used molten salt electrolytes, necessitating very high operating temperatures (650 to 750 K). Nevertheless, this pioneering work elucidated fundamental thermodynamic properties of the lithium-silicon system.

Many developments in the understanding of the lithium-silicon system quickly followed. In 1981, high temperature chemical diffusion coefficients in the intermediate phases of the lithium-silicon system were measured by Wen and Huggins using potentiostatic intermittent titration experiments[17]. The chemical diffusion coefficients across all four equilibrium phases, $Li_{12}Si_7$, Li_7Si_3, $Li_{13}Si_4$ and $Li_{22}Si_5$, is on the order of 6.0 x 10^{-5} cm^2 sec^{-1} at 415°C. However, the high operating temperatures and aggressively corrosive electrolyte materials remained an issue.

By the 1990s, substantial developments in layered metal oxide cathode materials, liquid electrolytes, and carbonaceous anodes made modern-day lithium-ion batteries a reality[18], and researchers around the world began investigating silicon as a next-generation lithium-ion anode material. However, achieving acceptable reversibility in silicon electrodes was a challenge. The expansion and contraction of silicon during the charge/discharge process resulted in extensive particle cracking. Over time, this causes the silicon particles to disconnect from the current collector and capacity fading ensues.

The first few publications where silicon was successfully incorporated into a lithium-ion anode involved forming a composite electrode of carbon and silicon. In 1996, Wilson et al. achieved a capacity of 600 mAh g^{-1} by using nano-dispersed silicon in pre-graphitic carbons using chemical vapor deposition (CVD)[19]. Unfortunately, the silicon content was limited to 11 wt%, due to its propensity to form inactive silicon carbide under CVD conditions. In 1998, Wang et al. reported > 1000 mAh g^{-1} (and 800 mAh g^{-1} after 10 cycles) in electrodes made by ball milling carbon and silicon together[20]. The high capacity was attributed to the nano-sized particles (~50 nm), which was achieved after extensive ball milling (150 hours). The electrode formulation was 73.6 wt% carbon, 18.4% silicon, and 8 wt % PTFE binder. This was the first demonstration of the benefits of nano-sizing silicon, following after the demonstration of this concept in Sn, Sb, and Ag-based alloy anode materials by Yang et al[21]. Size confinement (< 150 nm) in nanostructures resists particle cracking in electrodes, enabling significant improvements in cycling stability[22].

One of the earliest functional electrodes with majority silicon content was published by Hong Li et al[23]. This electrode featured silicon nanoparticles ball milled with carbon black, with a

formulation of 40 wt% silicon (78 nm diameter), 20 wt% carbon black, and 20 wt% PVDF binder. This electrode achieved 1700 mAh g^{-1} over 10 cycles. Building off this development, remarkable performance has been achieved by using nano-sized silicon structures in battery electrodes. Using nanowires, Chan et al. was able to achieve > 3,000 mAh g^{-1} over 10 cycles – extremely near to the theoretical capacity of silicon[24]. Other notable nanostructures include core-shell structures[25], nanoporous silicon[26,27], and hollow nanospheres[28].

There are many review articles on silicon as a lithium-ion anode active material that can be referred to for further detail on the subject[6,7].

1.1.1 Nano- vs. Micro- Silicon Particles

Despite the exceptional performance of silicon nanostructures, several drawbacks have kept industrial research focused on microparticles instead. Nanoscale size confinement results in a higher surface area-to-volume ratio, which creates more surfaces for solid-electrolyte interphase (SEI) formation, consuming electrolyte and lithium[29]. Slurries containing nanoparticles also require higher solvent content to maintain a suitable coating viscosity, which then requires additional energy expenditure to dry during in the case of slurry-made electrodes manufacturing[30,31]. If dry-electrode manufacturing processes are used, the safety hazards of airborne nanoparticles must be considered[32]. Nanosized powders also have low tap density, i.e., compacted mass per volume, which ultimately limits the volumetric energy density achievable. Moreover, the manufacturing cost for nanomaterials remains prohibitively high for consumer applications, due to time-intensive production routes, low yields, and scale-up issues[33]. Because of these disadvantages, development activities aimed at near-term production have focused on electrodes using micron-scale silicon structures.

1.2 Electrode Formulation

Subsequent landmark developments in commercially relevant silicon electrodes largely surrounded breakthroughs in the inactive components. We will focus on composite electrodes, as

they can be manufactured using well-established, high-throughput methods such as roll and slot-die coating, making this electrode type suitable for large-scale commercialization. These electrodes are a porous mixture of active material (silicon), conductive additive (typically carbon), and polymeric binder coated onto a copper current collector. A schematic of a composite silicon electrode cross-section is shown in **Figure 1.**

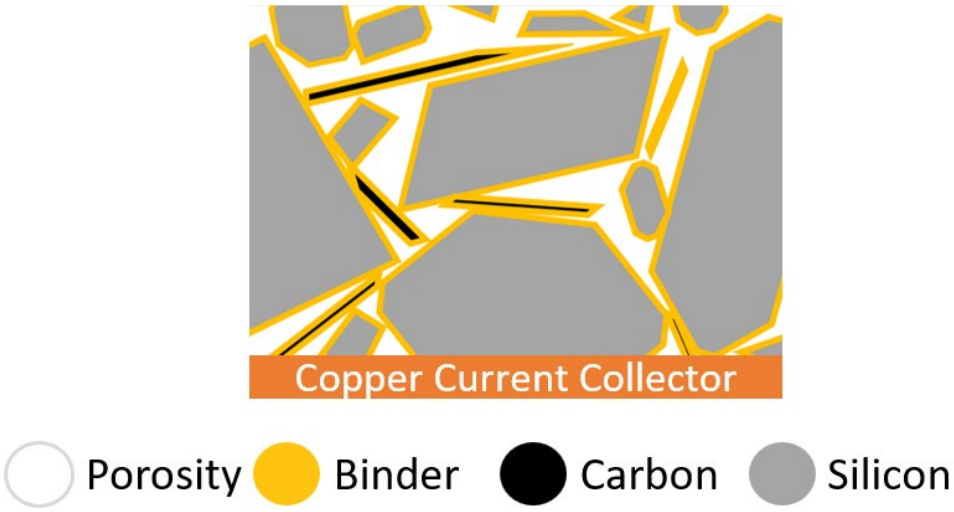

Figure 1. Schematic of composite silicon electrode cross-section

A scanning electron microscope image of a cross-section of an electrode used in this study is shown in **Figure 2**, for comparison.

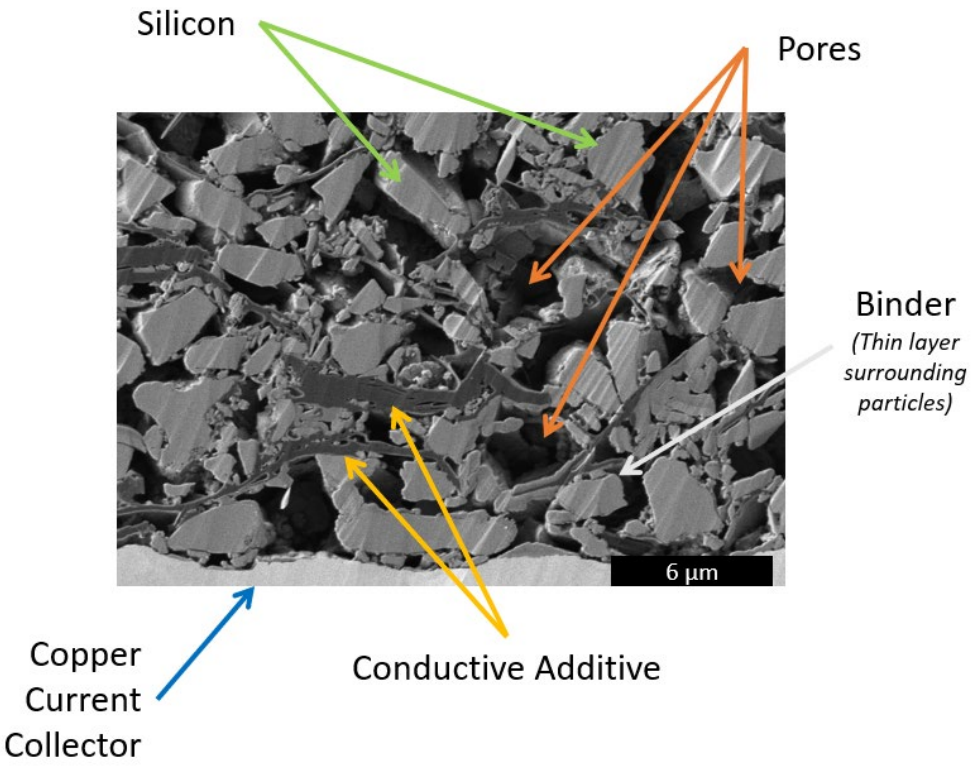

Figure 2. Secondary electron scanning electron micrograph of a composite silicon electrode.

The next sections will provide a brief overview of notable work concerning binders and conductive additives for silicon electrodes.

1.2.1 Development of Binder Chemistries for Silicon Anodes

A major milestone in silicon battery electrodes was the discovery that binder chemistry could substantially improve electrode performance. This kicked off an era of intense research to discover the best binders for silicon. There are numerous review articles on this subject[34–40]. A highlight of a few relevant developments is presented below.

While fluorinated polymers were conventionally used as battery binders due to their chemical stability, reliance on Van der Waals interactions was insufficient for maintaining

mechanical integrity in high volume expansion anodes. Moreover, polyvinylidene fluoride (PVDF) is reactive with lithium silicides, further contributing to electrode degradation[41].

One way to improve binder effectiveness is to facilitate the formation of covalent bonding between the binder and electrode particles. Li et al. showed that using carboxymethyl cellulose (CMC) as binder dramatically enhanced the initial capacity and cyclability of silicon-dominant electrodes, achieving 800-1200 mAh g_{Si}^{-1} over approximately 80 cycles with an electrode formulation of 80 wt% Si, 12 wt% SuperS carbon black, and 8 wt% CMC[42]. Magasinski et al. demonstrated the use of polyacrylic acid (PAA) as an efficient and effective binder for silicon, achieving > 2000 mAh g_{Si}^{-1} over 100 cycles with an electrode formulation of 43 wt% Si, 42 wt% carbon black, and 15 wt% binder[43]. Kovalenko et al. demonstrated the efficacy of sodium-alginate, another polymer with carboxylic acid functional groups, maintaining nearly 2000 mAh g_{Si}^{-1} over 100 cycles with a formulation of 64 wt% silicon, 22 wt% carbon black, and 15 wt% binder[44]. Alginate, PAA, and CMC all contain an abundance of carboxyl groups along the polymer backbone, which can covalently bond to the -OH groups on the silicon surface, providing long-lasting mechanical integrity[45–47]. The performance of these binders can be further improved by silicon particle surface modification or fine tuning slurry pH to modulate particle-binder bonding[48–52].

Another polymer that has been successfully used as a silicon electrode binder is polyimide (PI), a chemically resistant, thermally stable, and stiff polymer[53]. PI is a thermoset polymer, formed in-situ from poly (amic acid), as the high aromaticity and low solubility of PI makes it difficult to process otherwise. Through a condensation reaction at elevated temperatures, poly (amic acid) grafts onto the Si particle surface and forms polyimide. A summary of the performance of Si electrodes with PI binder is listed in **Table 2**.

Table 2: Summary of Silicon Electrodes with Polyimide Binder in Literature

Reference	Active material	Formulation	Si Loading	Performance
Kim et al.[54]	5 μm Si, as received and etched for porosity	50/40/10	0.22-0.24 mg cm^{-2}	76% capacity retention at 20 cycles, half cell
Uchida et al.[55]	Micrometric Si	75/10/15	2 mg cm^{-2}	167 cycles at 800 mAh/g capacity limit and 1600 mA/g current density
Wilkes et al.[53]	Si alloy, 3 μm	70/15/15	0.85 mg cm^{-2}	> 80% capacity retention @ 50 cycles

*Publication lists volumetric loading of 4.4-4.8 mg cm^{-3} and approximate electrode thickness of 50 μm. Areal loading was calculated from these values.

There has also been a plethora of "designer" binders which incorporate various functionalities and properties that have achieved notable improvements in electrode performance, such as self-healing, soft/hard segments[56], molecular scale mechanical strain relief[57,58], cross-linking[40,59,60], and electronic conductivity[61–67] into the polymer backbone. However, few silicon electrodes in literature exceed 3 mAh cm^{-2} (**Figure 3**). Meanwhile, demonstration of good performance at > 4 mAh cm^{-2} loadings are targeted for commercialization in automotive applications[68]. As such, the state-of-the-art has yet to converge on one or a few of the available binders for silicon electrodes.

1.2.2 Conductive Additive Morphologies

Another key component of silicon electrodes is conductive additive. In battery electrodes, conductive additives are typically carbonaceous.

The main function of the conductive additive is to provide an electrically conducting network throughout the electrode. We provide a summary of the electrical resistivities of the various components of silicon electrodes below.

The electrical resistivity of silicon depends on the purity and oxide layer thickness. Silicon is inherently non-conductive. The resistivity of intrinsic silicon is 2500 Ω cm[69], while that of metallurgical grade silicon is 0.66-2.05 Ω cm[70], closer to that of doped silicon used in microelectronics. However, all the materials which coat the silicon particles are substantially more resistive. Silicon forms a native oxide layer around 1-5 nm thick upon exposure to oxygen, even at room temperature[71]. The resistivity of this oxide layer is on the order of 10^{17} Ω cm[72]. Polymeric binders are generally insulating materials. While conductive polymer binders have lower resistivities, >1 Ω cm[73] for PEDOT:PSS, most other polymer binder materials have substantially higher resistivities: PAA resistivity is on the order of 10^{12} to 10^{13} Ω cm[74], PVDF on the order of 10^{14} to 10^{15} Ω cm[75], and PI on the order of 10^{16} to 10^{17} Ω cm[76]. Lastly, the electrically insulating nature of the SEI, which forms on all surfaces of the anode electrode, is key to its function and typically has a resistance of around 1-2 x 10^{7} Ω cm and a thickness of 30-50 Å[77]. With all the resistive components within the electrode, an electrically conductive network is necessary to facilitate the electron exchange that occurs during charging and discharging.

In contrast, the carbonaceous materials typically used as conductive additives for battery electrodes exhibit relatively high conductivity. The resistivity of typical carbon conductive additives depends on the chemical structure, surface groups, and defect density[78]. Due to differences in chemical bonding structure, graphene is the most conductive allotrope of carbon, while diamond is the most insulating one. Carbon black is the most commonly used conductive filler in battery electrodes. It is the product of either incomplete combustion or anoxic thermal decomposition of hydrocarbons[79] and is electrically conducting with a resistivity on the order of 10^{-2} to 10^{1} Ω cm[80,81]. Other common carbon filler morphologies include graphite (10^{3} Ω cm perpendicular to the basal plane and 10^{-4} Ω cm parallel to the basal plane in single crystals[82]), vapor grown carbon fibers (10^{-5} to 10^{-2} Ω cm[83,84]), multi-walled carbon nanotubes (~10^{-1} Ω cm[85]), and single-walled carbon nanotubes (10^{-6} to 10^{1} Ω cm, depending on helicity[86]). Conductive networks can also be formed in-situ via pyrolysis of polymeric materials, such as poly acrylonitrile (PAN). Resistivity of pyrolyzed PAN ranges between 10^{1} and 10^{5} Ω cm[87].

Usage of conductive additives in battery electrolytes must be judicious, balancing electrochemical performance benefits with processing characteristics and energy density. For slurry-made electrodes the slurry viscosity must be controlled to produce defect-free coatings. Slurry rheology is not just affected by solid volume fraction, but also factors such as particle size distribution, and particle shape[88]. Although low-density, high aspect ratio conductive filler particle morphologies are advantageous for gravimetric energy density, it must be balanced against the impact on other manufacturability and cost metrics. Increasing the amount of low-density and/or high aspect ratio conductive additive particles in the electrode formulation will necessitate an increase in slurry solvent content to maintain the same viscosity. However, increasing the solvent content increases the energy needed to dry the coating, thereby increasing manufacturing cost[89].

Overdosing electrodes with conductive additives can also hamper volumetric energy density. Commercial and state-of-the-art cathode electrodes typically use < 5 wt% conductive additive content[90,91]. Meanwhile, the conductive additive content of microparticle silicon electrode formulations in published literature spans a large range—from 5 to 40 wt%[54,92], more commonly 5 to 15 wt%[42,48,53–55,58]. The large range indicates that there is ample opportunity for improving the efficiency of conductive additive usage in silicon electrode formulations.

1.3 Development Targets and Current Status

The United States Advanced Battery Consortium (USABC) and the Department of Energy Vehicle Technologies Office have set performance targets to guide research and development work in academia, government labs, and industry[68,93]. The overarching goals are to:

- Reduce the cost of electric vehicle batteries to less than $100/kWh—ultimately $80/kWh
- Increase range of electric vehicles to 300 miles
- Decrease charge time to 15 minutes or less

More relevant to silicon are the targets for low-cost, fast-charge batteries, which include reaching 1000 cycles at > 4 mAh cm^{-2} for commercialization in 2025[68]. Despite the many

developments in silicon electrodes for lithium-ion batteries, the challenge of achieving these targets still stands. A brief overview of the functional capacity vs. cycle number for silicon-containing electrodes reported in literature is included below.

Table 3: Brief Literature Review of Functional Capacity vs. Cycle Number for Silicon-Containing Lithium-Ion Anodes, to Capture Functional Capacity of Electrodes after Extended Cycling

Reference	Material System	Functional Capacity *(mAh cm^{-2})*	Number of Cycles
Zhang et al.[92]	MXene Si nanoparticles	5	50
		1.28	250
Cho et al.[57]	Pyrene-Polyrotaxane-Poly acrylic acid, SiO	2.25	160
		3	60
		2	450
		2.5	100
Choi et al.[58]	Polyrotaxane-Poly acrylic acid, Si nanoparticles	1.5	400
		2.5	50
		2.25	150
Uchida et al.[55]	Polyimide, Si microparticles	1.6	300
		2.4	175
Neale et al.[94]	Pitch, Si nanoparticles	0.968	800
Jia et al.[95]	CNT-Si nanoparticle composite, half cell	2.75	500
	CNT-Si nanoparticle-Graphite composite, full cell	3	500
Dang et al.[48]	Lithiated-PAA, Si microparticles	2.025	100
Wang et al.[96]	Self-healing binder, Si microparticles	1.2	130
This Work	PI, Silicon microparticles, 1 x PI	2.5	175
	PI, Silicon microparticles, 3 x PI	2	212

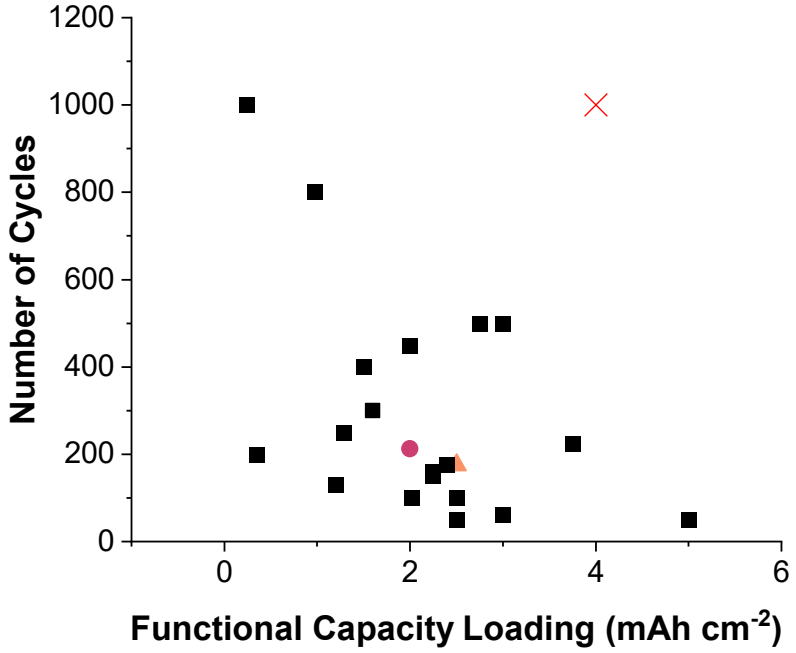

Figure 3. Plot of cycle number vs functional capacity loadings as reported in literature. Performance of the electrodes from in this work is denoted by the orange triangle (1 x PI formulation) and magenta circle (3 x PI formulation) symbols. The red X denotes the USABC target for 2025 production.

1.4 Dissertation Scope

From the literature, it is evident that the inactive components of the electrode play a significant role in realizing the full potential of silicon in lithium-ion batteries. Many of the milestone developments in silicon development depended upon effective design, formulation, and incorporation of binder and conductive additives. Yet, the study of how to formulate battery electrodes remains on the sidelines of published literature. Developing the fundamental understanding to guide optimization of binder and conductive filler use in silicon electrodes remains a largely unexplored area in literature and would provide significant benefit to the research community.

This dissertation aims to elucidate the influence of formulation on structure, properties, and electrochemical performance of silicon anode electrodes. The second chapter focuses on

understanding the effect of binder content in silicon microparticle electrode formulations, the third chapter on the effects of conductive additive content, and the fourth chapter on how cell design affects cell expansion and ultimately, volumetric energy density.

Chapter 2 Effect of Binder Content

2.1 Introduction

Silicon anodes are seen as the next advancement in lithium-ion battery anode technology, as they have the potential for three times the volumetric capacity, ten times the gravimetric capacity[97], are more amenable for fast-charge[98], and can be made using similar manufacturing processes as the incumbent, widely commercialized graphite anodes[99]. The introduction of silicon anodes could be a critical step towards increasing electric vehicle adoption among consumers. However, insufficient electrode durability remains a significant barrier to widespread commercialization. It is well-known that silicon undergoes a nearly 300% volume expansion during full lithiation, which can crack the active material and electrode, leading to active material isolation, additional electrolyte decomposition and concomitant solid-electrolyte interphase (SEI) formation, increases in ionic resistance, and ultimately, irreversible capacity loss[6,97,100]. Nanoparticle and nanostructured silicon electrodes were proposed as possible solutions to these issues, as size-confinement resists cracking[101,102]. However, low tap density, high interparticle resistance, and high manufacturing costs make nanosized silicon anodes unappealing for industrial production. Consequently, industrial focus has shifted towards micron sized silicon electrodes[103–105].

Binder optimization is a key factor in mitigating the degradation of composite silicon electrodes. In composite electrodes, binders are required to maintain the electrode's conductive network and mechanical integrity[34,36,106]. The large volume expansion and particle cracking in silicon microparticle electrodes necessitate improved electrode binders, as conventional PVDF binders were found ineffective in silicon electrodes[42,97,104]. Several binder chemistries reported in literature have enabled relatively long-term cycling of silicon microparticle electrodes, including

partially lithiated poly (acrylic acid)[48], poly(rotaxane)[58], and self-healing polymers[96,107,108]. These binder chemistries are able to form effective bonds between electrode components and maintain mechanical integrity of the electrode throughout cycling.

Despite being an "inactive" electrode component, the binder impacts nearly every aspect of electrode performance. Beyond its mechanical function, the binder also influences slurry processing characteristics[109–111], resulting electrode morphology[112], composite mechanical behavior[113,114], interfacial interactions with the electrode particles[45,115], and solid—electrolyte interphase formation[115–118], which can then impact the electrode's electrochemical performance[112,119]. Despite the progress in this area of research, there are still gaps in scientific understanding of the ideal binder content and morphology within a slurry and its resultant composite electrode, including:

- Should the binder coat the silicon particles conformally to promote electrode cohesion? How would a uniform coating affect the electronic and ionic conduction pathways?
- What are the effects of binder content on the electrode morphology, e.g., porosity and tortuosity?

Recent reports have shown that inhomogeneous binder coverage on silicon particles could still produce high-performing electrodes[110,119], despite earlier analysis that suggested conformal coatings of binder on silicon to be optimal for limiting SEI formation and maintaining mechanical integrity[97]. Landesfeind et al. studied the influence of binder on graphite electrode tortuosity, and showed that lower binder layer thicknesses resulted in lower electrode tortuosity and improved rate performance[112]. Many studies have reported cycling data for electrodes at different areal loadings; generally, higher loaded electrodes suffer from faster degradation[56,108,120].

Few publications have reported battery performance data from several electrode formulations using the same binder and at the same high areal capacity, as formulation optimization was not the main focus of their studies. Generally, more binder is shown to be beneficial to improving electrode capacity and durability[62,67] and insufficient carbon content can hinder electron transport[55]. There is a wide range of binder contents utilized in literature for

silicon electrodes, ranging from 8 to 44 wt%[48,49,96,107]. The wide range is partially due to differences in silicon and conductive filler particle sizes and densities, which influence the total particle surface area. To our knowledge, there has not been a published, systematic study on the impact of binder content on long-term cycling and rate performance in microparticle silicon anodes at industrially relevant areal loadings in full cells.

In this study, we focus on investigating the impact of polyimide (PI) binder weight fraction in silicon microparticle electrodes with high loadings. Electrode adhesion to the current collector, cohesion, porosity, electrical resistivity, and electrical tortuosity were characterized in pristine electrodes. These properties were then correlated to electrode cycle life and rate performance in Si-NMC622 full cells. We show that there is an optimal binder weight fraction for a given type of polymer binder. Increasing binder weight fraction improves electrode adhesion and cohesion, resulting in improved cycle life. However, increased binder weight fraction decreases electrical conductivity and porosity, leading to poorer silicon particle utilization, capacity, and rate performance.

2.2 Experimental Methods

2.2.1 Electrode Preparation and Cell Construction

Silicon microparticle electrodes were prepared by mixing silicon microparticles (Elkem Silgrain e-Si 409, D50 = 2.7 μm), graphene nanoplatelets (GNP) (xGSciences, xGnP, grade H5, average particle diameter = 5 μm), and polyimide binder (Ube U-Varnish A) with n-methyl-2-pyrrolidone (NMP) (VWR, SEMI grade) as solvent. The slurries were prepared by a planetary mixer (FlackTek SpeedMixer, DAC 600.1 FVZ) with 3 mm yttria stabilized zirconia beads in the mixing cup to help break up particle agglomerates. Mixing bead to slurry weight ratio was 1:2. The slurry preparation steps were optimized for particle de-agglomeration by maintaining a high solids content during initial mixing and adding the binder solution incrementally.

Slurry preparation steps were as follows:

1. Add silicon, GNP, NMP, and mixing beads to slurry mixing cup and mix at 2000 rpm for 15 minutes.
2. NMP weight ratio was 40%.
3. Mixing beads were 33% of total final slurry weight.
4. Add more NMP and mix at 2000 rpm for 15 minutes.
5. New NMP weight ratio is 50%.
6. Add half of binder solution and mix at 2000 rpm for 10 minutes.
7. Repeat step 3.
8. Coat onto copper using doctor blade. To achieve target loading, doctor blade was set between DR9 and DR18, depending on the solvent content of the formulation.

Slurries were cast on battery grade copper foil (thickness 8 μm) using an 80-180 μm gap on doctor blade (MTI Corporation) and automatic coater (MTI Corporation). Gap settings varied based on the formulation. Electrode coatings were dried under vacuum at 50°C overnight then heat treated to 350°C for 30 minutes under argon in a tube furnace (MTI Corporation, OTI-1200X) to imidize the binder. Electrode active mass loadings were 3 – 3.5 mg cm^{-2}. For our study, we varied the binder content in the formulation while keeping the silicon-to-carbon weight ratio to 8:1. **Table 4** lists the formulations tested in this study. The 80/10/10 formulation was chosen as our baseline because it produces a binder layer thickness of 6 nm, which has empirically been shown to produce a good balance between energy density, electrochemical performance, and electrode cohesion in NMC cathodes and graphite anodes[112,121].

Table 4: Electrode formulations utilized to study effect of binder content.

Formulation Name	Si/C/PI (wt %)	Calculated Binder Thickness (nm)
$^1/_3 \times$ **PI**	85.8/10.7/3.5	2
$^2/_3 \times$ **PI**	82.8/10.4/6.8	4
1 × PI	80/10/10	6
$^4/_3 \times$ **PI**	78/9.8/12.2	8
3 × PI	66.7/8.3/25	18

Cathode electrodes were provided by the General Motors Warren Cell Fabrication Laboratory. The electrodes contained 93.5 wt% NMC622, 2.5 wt% SuperP (Imerys), 1.5 wt% KS6 (Timcal), and 2.5 wt% PVDF binder (Kynar HSV 1800) and were pressed to 25% porosity. Cathode active material loading was 4.5 mAh cm^{-2}.

Full cells were assembled using the silicon anode electrodes (15.3 mm diameter), NMC622 cathode (12.7 mm diameter), Celgard 2325 separator, 40 µL of electrolyte (1.2 M $LiPF_6$ in dimethyl carbonate:fluoroethylene carbonate 1:4 with 2 wt% of vinylene carbonate and 3 wt% of OS3 from Silatronix), a 1.0 mm stainless steel spacer, and a 1.4 mm spring in a CR2032 coin cell. The capacity ratio of the negative to positive electrodes were N/P = 2.0 ± 0.05.

2.2.2 Electrochemical Testing

Electrochemical tests were conducted on a Maccor cycler. Charge rates were calculated based on the cathode electrode capacity. The galvanostatic cycling protocol consisted of two formation cycles (CC charge at C/20, CV charge until C/50, CC discharge at C/20) followed by cycling (CC charge at C/5, CV charge until C/20, CC discharge at C/5) between 3.0 and 4.2 V. A 15-minute rest period was employed after each charge and discharge. The rate testing protocol used the same formation protocol, followed by 5 cycles at C/10, C/5, C/2, 1C, 2C, 5C, and C/5. Discharges were carried out at C/5 when charge rate exceeded that rate, to ensure that electrodes were sufficiently discharged at each cycle.

2.2.3 Porosity Measurement

Total electrode porosities were calculated from thickness and weight measurements from a circular punch of electrode coated on copper current collector using the following equation:

$$P = \frac{t_{electrode}\pi r^2}{w_{electrode}\left(\frac{f_{Si}}{\rho_{Si}} + \frac{f_C}{\rho_C} + \frac{f_B}{\rho_B}\right)}$$

eq. 1

, where $t_{electrode}$ denotes the thickness of the electrode coating, r denotes the circular punch radius, $w_{electrode}$ is the weight of the electrode coating, and f_{Si}, f_C, f_B, ρ_{Si}, ρ_C, and ρ_B are the weight fractions and densities of silicon, conductive carbon, and binder, respectively. The electrode coating thickness was obtained by subtracting the bare copper thickness from the total electrode assembly thickness. Electrode thickness measurements were taken using a Heidenhain MT 1281 length gauge in order to determine electrode porosity or to convert electrode resistance to resistivity.

Connected porosity was measured by soaking electrode punches in electrolyte for 18 hours and weighing the electrodes before and after soaking. Five 15.3 mm punches were weighed at once to reduce the effects of experimental noise. Further details are provided in **Appendix D**.

2.2.4 Electrical resistivity measurements

Electrical resistivity measurements were conducted by measuring the resistance across a symmetric coin cell. These CR2032 coin cells contained two electrodes of interest with the electrodes facing one another, a 1.0 mm stainless steel spacer, and a 1.4 mm spring.

2.2.5 Mechanical Testing

Microscratch testing was conducted with an Anton Paar Micro Scratch Tester with a diamond spheroconical indenter (semiapex angle 60°, tip radius 2 μm) on electrode coatings on copper foil. Samples from electrode coatings were mounted onto the surface of mechanically polished, cylindrical acrylic pucks using superglue. The acrylic puck was then clamped on the MicroScratch Tester for scratch testing. The scratch distance, scratch velocity, and starting normal load were 2500 μm, 12 μm/sec, and 10 mN, respectively. Maximum normal loads were 50, 200, and 400 mN for the $^1/_3$ x, 1 x, and 3 x PI electrodes, respectively. Variations in electrode strength due to binder content necessitated the use of different maximum normal forces during the scratch testing. Excess normal load would scratch the current collector, while insufficient normal load could not scratch the electrode surface. We found that measured fracture toughness

became invariant once a critical normal load was reached. Scratch depths were measured using a Bruker NP Flex 3D metrology system.

The 180° peel test was conducted following the methodology presented in Hu et al.'s work[122]. Electrode coatings were cut to 10 mm width and at least 60 mm in length and adhered to an aluminum plate using double-sided tape (3M, 410M tape). Peel tests were conducted using an Imada ZTA-1 5 N load cell and tester, pulling the current collector at 50 mm min^{-1}.

2.2.6 Scanning Electron Microscopy

Scanning electron microscope (SEM) images were taken on a Hitachi S-4800 at 2 kV, using the secondary electron detector. Cross-sections were prepared using a Hitachi IM4000 ion milling system. For sections of cycled electrodes, cells were disassembled in an Argon-filled glove box and transferred to the ion miller in sealed containers. Sample alignment for ion milling and transfer to SEM were done in air as quickly as possible to minimize air exposure. Air exposure was typically less than two minutes.

2.2.7 X-ray Diffraction

X-ray diffraction (XRD) was conducted using a Bruker D8 Advance equipped with a Lynxeye detector in 1D mode and Cu Kα radiation at 39 kV and 40 mA. 2θ range, step time, and step size were 5-100°, 1.00 s, and 0.020°, respectively. Cycled electrodes were extracted from coin cells and rinsed in dimethyl carbonate (DMC). In coin cells, the anode is oversized, so prior to XRD analysis, the cycled anodes were cut with a $^3/_8$-inch circular punch to remove the excess, unreacted silicon along the outer edge of the oversized electrode. After punching, the electrode was placed in an airtight XRD specimen holder (Bruker, Airtight PMMA Rings) and sealed with Kapton film.

2.2.8 Atomic Force Microscopy

To study the electrical connectivity of prepared electrode cross-sections, PeakForce Tunneling AFM (PFTUNA) was implemented. Cross-sections of electrodes were mounted onto

a cross-section holder in an argon filled glovebox. The current collector was electrically connected to ground using carbon sticky tape while the conducting AFM tip (SCM-PIT V2, Bruker AFM probes) was used as an electrical probe. The PeakForce set point was set to 1.2 volts (V) to ensure good electrical contact between the probe and the sample during the measurement while an applied voltage of 2 V between the current collector on the electrode cross-section and AFM tip was used. The current sensitivity was set to the maximum setting (20 pA/V).

Data analysis was performed using OriginLab software (Origin 2022, Northampton, MA). One-way analysis of variance with Tukey's method was used to analyze statistical significance. Sample sizes are indicated in each figure caption. Error bars represent standard deviation.

2.3 Results

2.3.1 Pristine Electrode Properties

To gain an understanding of electrode properties prior to cycling, the porosity, electrical conductivity, mechanical cohesion and adhesion in pristine electrodes with varying binder content were measured.

Figure 4 shows SEM images of electrode cross-sections at different stages of cycling. The top row shows the electrodes in their as-made, pristine state. Silicon particles, GNP particles, electrode pores, and the copper current collector are indicated by the arrows on the top left image. The vertical striations are artifacts from ion milling. The binder phase is difficult to see in the low-binder content electrodes due to lack of spatial resolution, while it can be identified as the space-filling grey with rounded edges that surrounds the particles in electrodes with higher binder content. The total thickness of the pristine electrodes decreased with increasing binder content. SEM images of the cycled electrode cross-sections will be discussed later in this section.

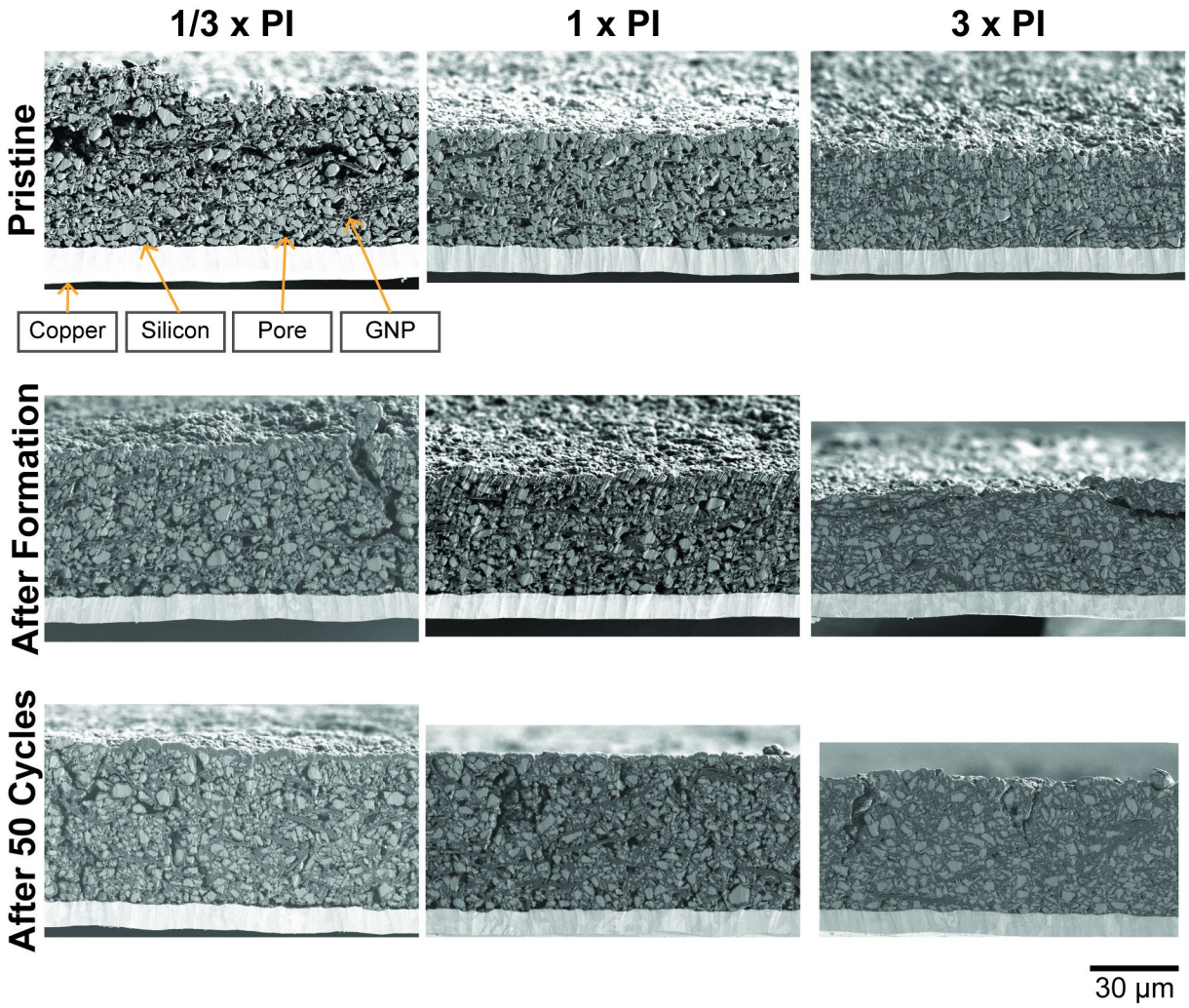

Figure 4. SEM images of 1/3 x PI (left column), 1 x PI (middle column), and 3 x PI (right column) electrodes in their pristine state (top row), after formation in the delithiated state (middle row), and after 50 cycles in the delithiated state (bottom row). The scale bar applies to all images.

Figure 5 shows the measured porosity for pristine electrodes with different binder loadings, averaged over three sets of five electrode punches. The total height of the bars represents the total porosity, while the connected pores are represented by the lower portion of the bars. The balance is assumed to be isolated pores and is represented in top portion of the bars. While the total porosity decreases with increasing binder content, the connected porosity is most severely impacted by increasing binder content.

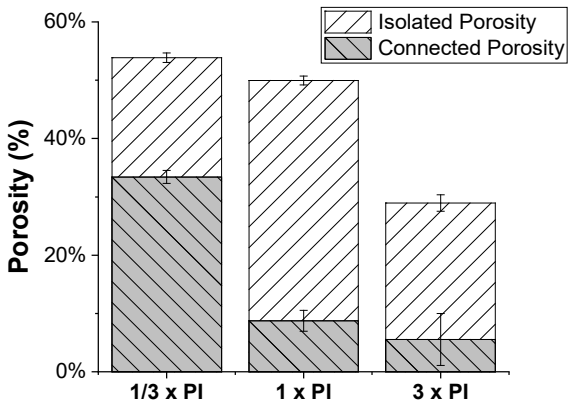

Figure 5. Isolated and connected porosity of pristine electrodes for each formulation (n = 3).

We used micro-scratch tests to characterize the cohesion between electrode components, following the methodology and analysis presented by Dang et al.[48] SEM images of the scratch surfaces (**Figure 6**) show that the scratch causes cracking and flaking of the electrode rather than of the electrode particles.

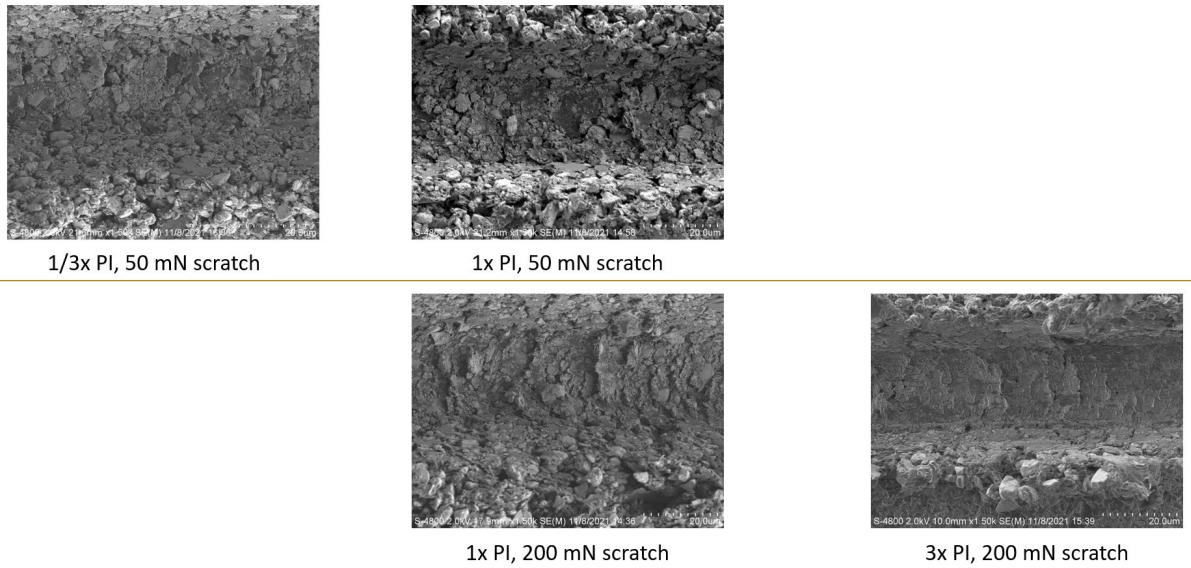

Figure 6. SEM of scratched surfaces on the electrodes.

Fracture toughness, K_c, which represents the electrode's resistance to cracking, was calculated using eq. 2, where F_T is the lateral force measured during the scratch test, d, the diameter of the scratch tip, and θ, the semiapex angle of the scratch tip.

$$K_c = \frac{F_T}{2d^{\frac{3}{2}}}\sqrt{\frac{cos\theta}{tan\theta}}$$

eq. 2

Fracture toughness was observed to increase with binder content (**Figure 7**a).

Peel tests were used to evaluate the electrode-to-current collector adhesion. For each specimen, peel force was determined as the average peel force measured over 30 mm of peel length. Typical peel force vs. peel length curves are provided in **Figure 8**. Peel force was also observed to increase with binder content (**Figure 7**b).

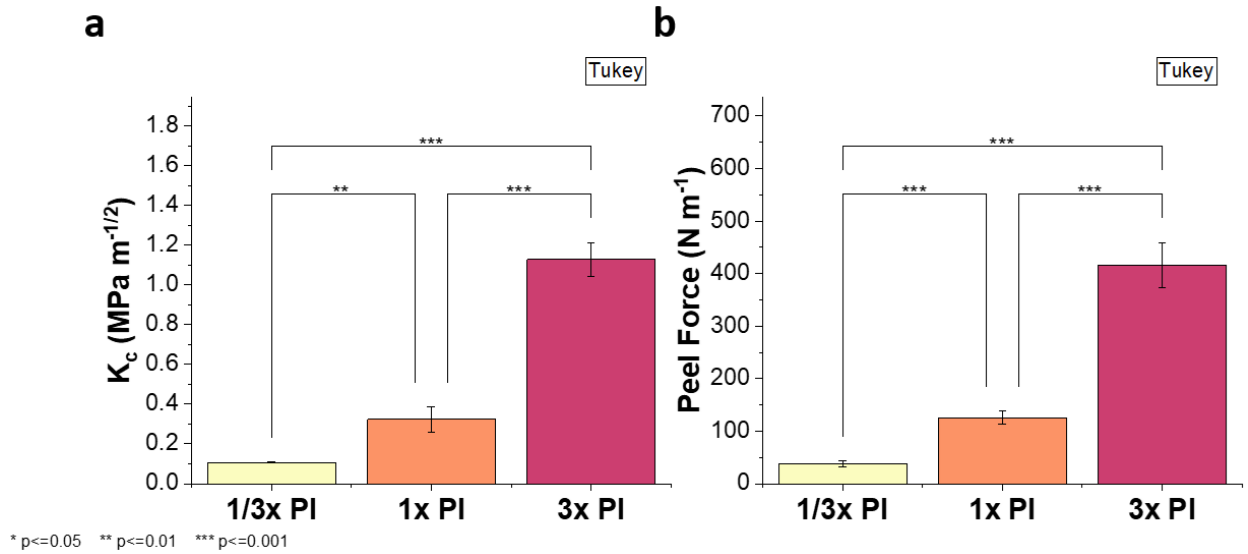

Figure 7. (a) Fracture toughness from scratch tests and (n ≥ 3) and (b) peel force from 180° peel tests on pristine electrodes of each formulation (n ≥ 5).

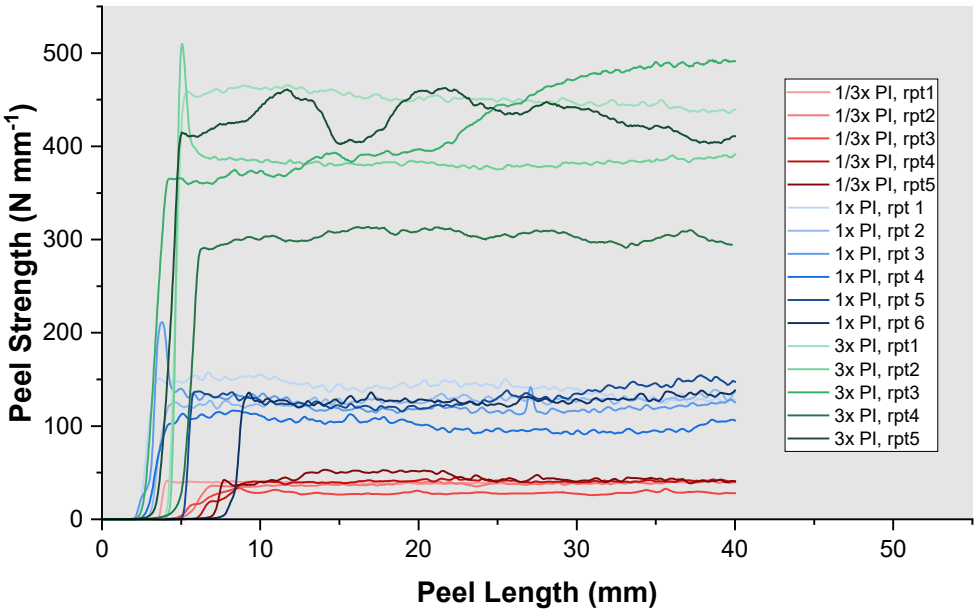

Figure 8. Typical peel strength vs peel length curves.

To understand the impact of binder content on the electronic pathways through the electrodes, we measured the electrical conductivity of pristine electrodes with varying binder content. Electrical conductivity reduced with increasing binder content when the binder content exceeded the 1 x PI loading (**Figure 9**).

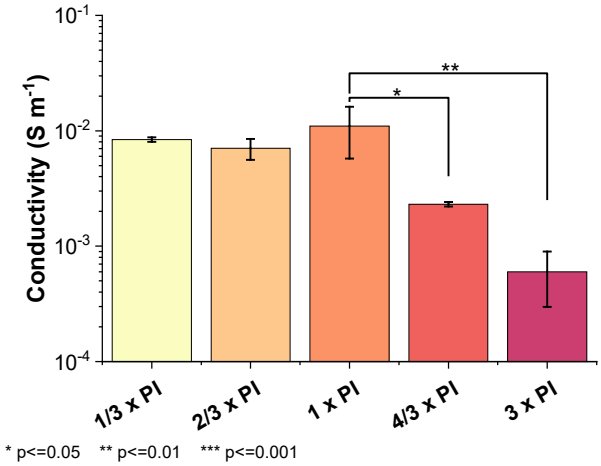

Figure 9. Electrical conductivity of pristine electrodes with varying binder content (n = 3).

2.3.2 Electrochemical Performance

The electrodes were then cycled in Si-NMC622 full cells to assess their electrochemical performance. **Figure 10** shows the mean and standard deviation discharge capacity from full cell cycle life testing. Three cells were tested for each anode formulation. The baseline formulation showed the highest discharge capacity throughout cycling. Sudden drops or step-like increases in discharge capacity were caused by unexpected power outages during cycling. In the case of the step-increases in cell capacity, the power outage occurred during discharge for an extended period and allowed the cell voltage to relax below the lower cutoff voltage. When power was restored, charging resumed from the relaxed voltage, resulting in an artificially high cell capacity. In some cases, the voltage relaxed below the lower cutoff cell voltage, e.g., 1.7 V, permanently altering the electrode materials, structure, or both. We hypothesize that the low voltage excursion activated lithium ions that are typically too sluggish at the intended cutoff cell voltage, however, further study would be required to confirm this. Due to this, a higher capacity was attained in the subsequent charge cycles, resulting in the step-increase in capacity. When momentary power outages occurred during discharge or during the rest prior to discharge with little to no voltage relaxation in the cell, the discharge cycle was simply cut short, resulting in a sudden drop in capacity that is recovered in the subsequent cycle.

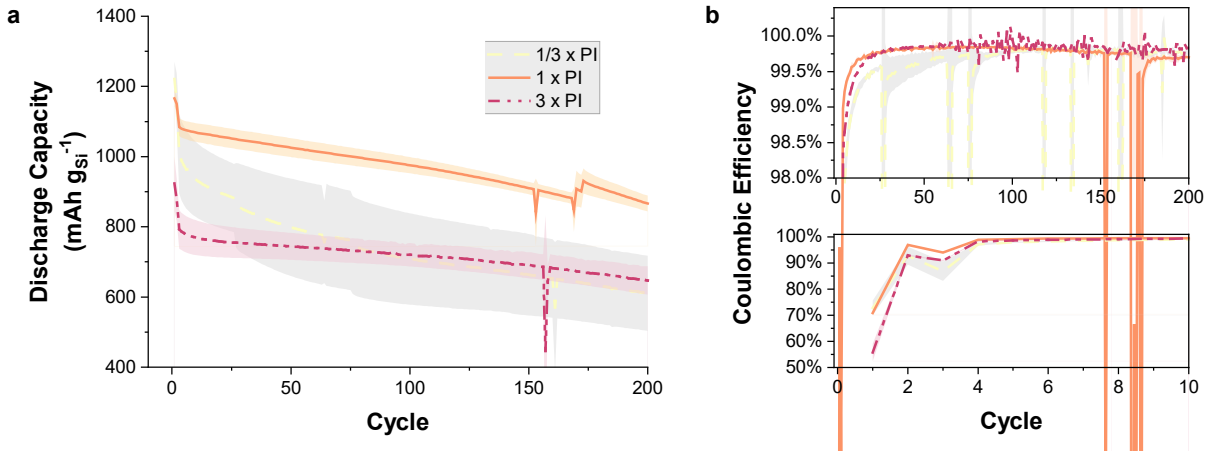

Figure 10. (a) Discharge capacity per gram of silicon and (b) coulombic efficiencies for electrodes with varying binder content, cycled at C/5 (n = 3). A close-up of the coulombic efficiencies for the first ten cycles is provided in the bottom right plot.

Figure 11 shows three key performance metrics from the cycling test: initial coulombic efficiency (ICE), initial discharge capacity (after formation), and number of cycles to 80% capacity retention (calculated from the 1st cycle after formation). ICE and initial discharge capacity significantly decreased with high binder content, while capacity retention improved with increasing binder content.

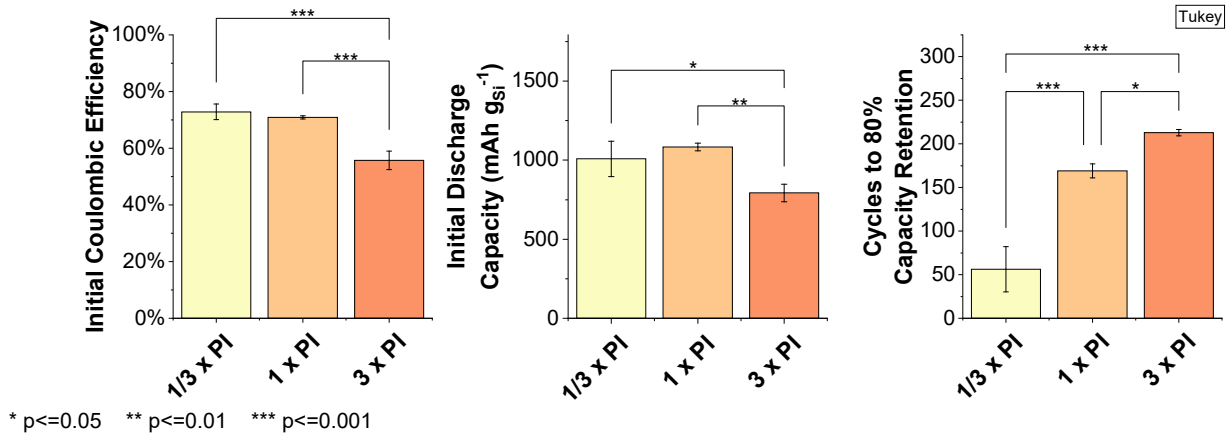

Figure 11. Initial coulombic efficiency (left), initial discharge capacity after formation (middle), and number of cycles to 80% capacity retention (right) for cells with varying binder content.

Charge voltage profiles were collected for each electrode formulation at the 1st formation cycle, 1st cycle after formation, cycle 100, and cycle 200 (**Figure 12**). Charging overpotentials increase with cycle number for each formulation. After formation, the 1 x PI formulation has the lowest overall charging overpotential, followed by $^1/_3$ x PI and then 3 x PI. Later in cycling, the charging overpotentials for the $^1/_3$ x PI formulation become greater than the 3 x PI formulation, while the 1 x PI formulation maintains the lowest overpotentials.

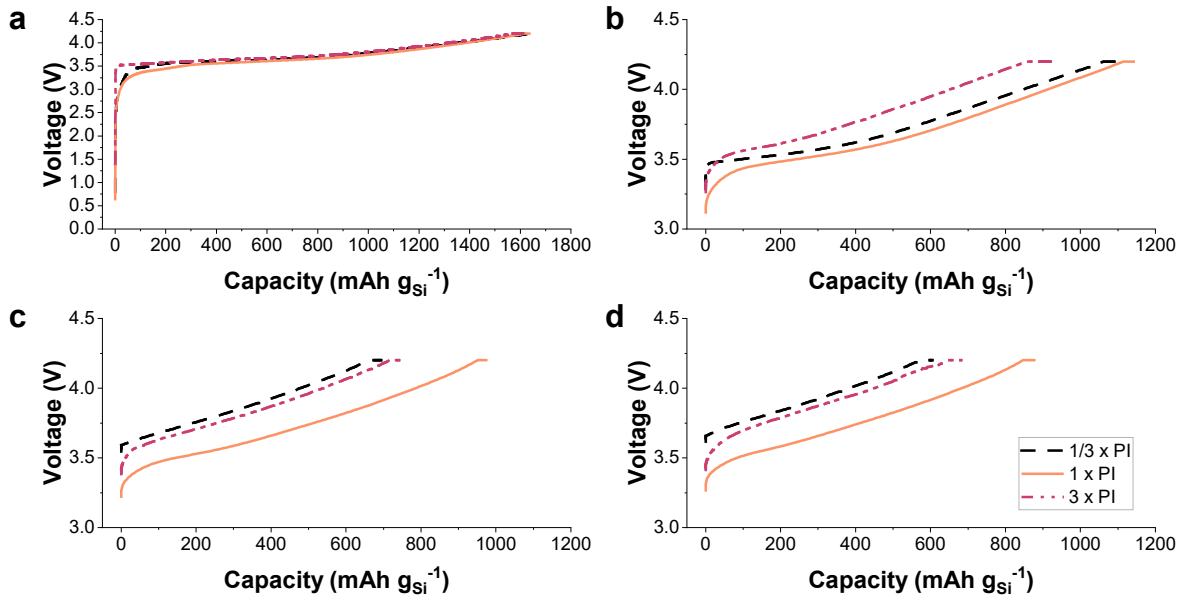

Figure 12. Charge voltage profiles for electrodes with varying binder content: (a) 1st formation cycle, (b) 1st cycle after formation, (c) 100th cycle, and (d) 200th cycle.

After formation and cycling, several changes in electrode morphology are observed in SEM images of the electrode cross-sections (**Figure 4**). Some degree of electrode cracking is observed in all three cycled electrodes. After formation, we also observe a thin layer surrounding the silicon particles and filling in the electrode pores, which we deduce to be SEI. The thickness of the SEI after formation decreases with increasing binder content. With cycling, both the thickness of the SEI and the electrode increase; less thickness increase is observed with increasing binder content.

Full cell rate tests were also conducted. At all rates after formation, the 1 x PI formulation showed the highest charge capacity, followed by $^{1}/_{3}$ x PI, then 3 x PI (**Figure 13**).

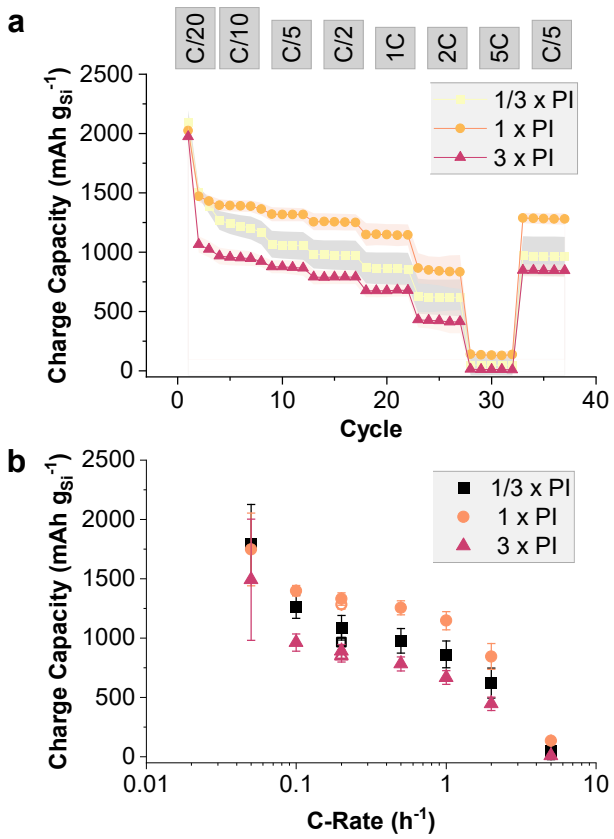

Figure 13. (a) Constant current charge capacity vs. cycle during rate testing, with charge rates listed across the top of the chart and (b) semi-log plot of charge capacity vs. C-rate (n = 3).

2.3.3 Post-Mortem Analysis

XRD was conducted on pristine and cycled electrodes to measure silicon utilization during cycling. Typical XRD spectra are provided in **Figure 14**.

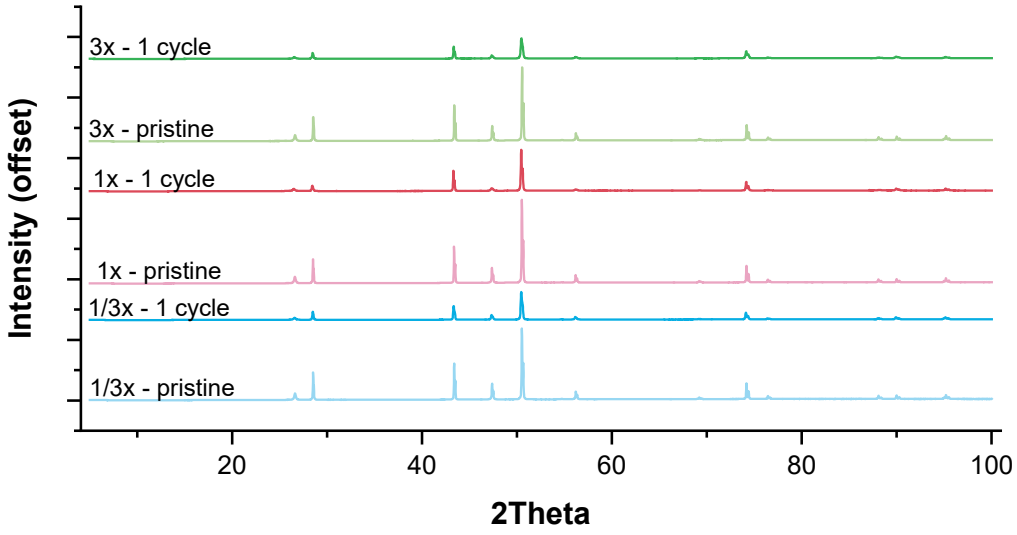

Figure 14. Typical XRD spectra on pristine and cycled electrodes with varying binder contents.

As the silicon is lithiated and amorphized, the silicon XRD peak decreases in intensity.[123] We used the Cu(200) peak intensity as an internal reference, as the current collector remains unchanged during cycling. As a measure of silicon amorphization after cycling, we used the following equation:

$$\%\ Si\ Amorphization = \frac{\left(\frac{I_{Si(311),pristine}}{I_{Cu(200),pristine}} - \frac{I_{Si(311),cycled}}{I_{Cu(200),cycled}}\right)}{\frac{I_{Si(311),pristine}}{I_{Cu(200),pristine}}}$$

eq. 3

The Si(311) peak was chosen because it exhibited a strong signal and did not overlap with peaks from other electrode components. Similar results were obtained when the Si(111) peak was used. Additionally, in pristine electrodes, the Si/Cu peak intensity ratios were not affected by varying the binder content.

In the first formation cycle, formulations from $^{2}/_{3}$ to $^{4}/_{3}$ x PI exhibited relatively high silicon utilization, while the higher and lower binder content electrodes exhibited lower silicon utilization. At binder contents above $^{2}/_{3}$ x PI, higher silicon utilization correlated with higher initial discharge capacity. However, the $^{1}/_{3}$ x PI formulation showed relatively low silicon

utilization, despite having a high discharge capacity (**Figure 15**). After 50 cycles, the % silicon amorphization increased for all formulations, despite decaying discharge capacity (**Figure 15**). Greater increases in silicon amorphization were observed in the $^1/_3$ and 3 x PI formulations than in the 1 x PI formulation between formation and 50 cycles.

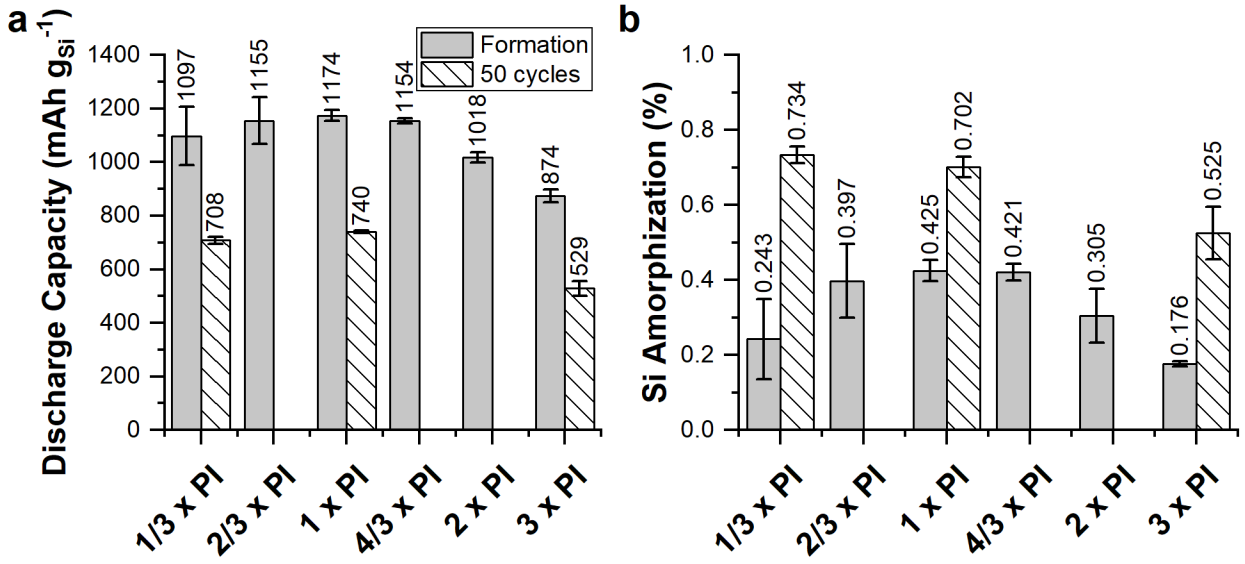

Figure 15. (a) Discharge capacity and (b) silicon amorphization after the 1st formation cycle and after 50 cycles for electrodes with varying binder content. (n ≥ 2)

To estimate the degree of lithiation in the amorphized silicon, we divide the measured discharge capacity, which is normalized by the weight of all available silicon in the electrode, by the percent silicon amorphization, measured from XRD:

$$Q_{Si,amorphized} = \frac{Q_{Si,total}}{\%\ Si\ amorphization}$$

eq. 4

We note that this calculation does not account for any potential capacity contributions from the polyimide binder[53,124] or GNP particles[125], which may explain the estimated gravimetric capacities in excess of the theoretical capacity of silicon[7,15,126]. Despite these unaccounted capacity contributions, we believe this calculation still reveals how the binder content affects the degree of lithiation in the amorphized silicon, given that the binder and GNP comprise a smaller fraction

of the electrode. **Figure 16** shows the calculated degree of lithiation in the amorphized silicon in electrodes with varying binder content.

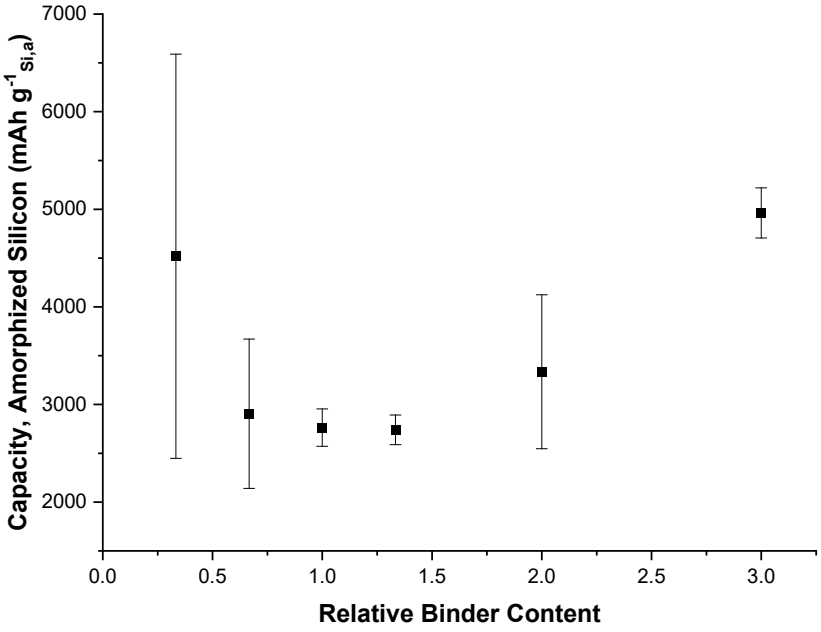

Figure 16. Calculated capacity of the amorphized silicon after formation in electrodes with varying binder contents. Error bars represent the propagated error from XRD and discharge capacity measurements.

We also used Peakforce Tunneling AFM (PFTUNA) to map the local electronic conductivity on electrode cross-sections after extended cycling. **Figure 17** shows the pull-off adhesion maps (left column) and the PFTUNA maps (right column) with the current collector oriented vertically along the left side of the image. The adhesion maps correspond well to SEM images and allow us to identify what is being imaged, as topography maps of the ion-milled cross-sections only show a monolithic surface. A comparison between SEM and AFM imaging is shown in **Figure 18**. By comparing the adhesion map and the SEM images, the long plate-like features are identified as the GNP conductive additive and the faceted blocks are silicon particles. Binder, pores, and SEI dominate the regions in between the electrode particles. In the conductivity map, larger currents indicate a greater electrical connectivity with the current collector, as the voltage is applied between the current collector and the AFM tip.

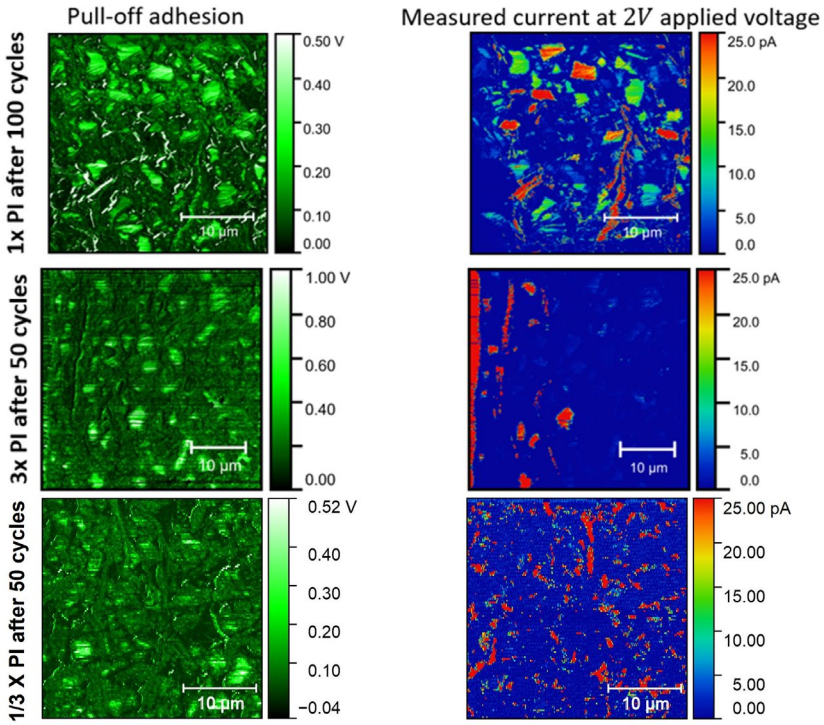

Figure 17. The left column contains AFM pull-off adhesion maps and right column contains PFTUNA maps of cycled electrodes: (top) 1 x PI electrode after 100 cycles, (middle) 3 x PI electrode after 50 cycles, and (bottom) 1/3 x PI electrode after 50 cycles.

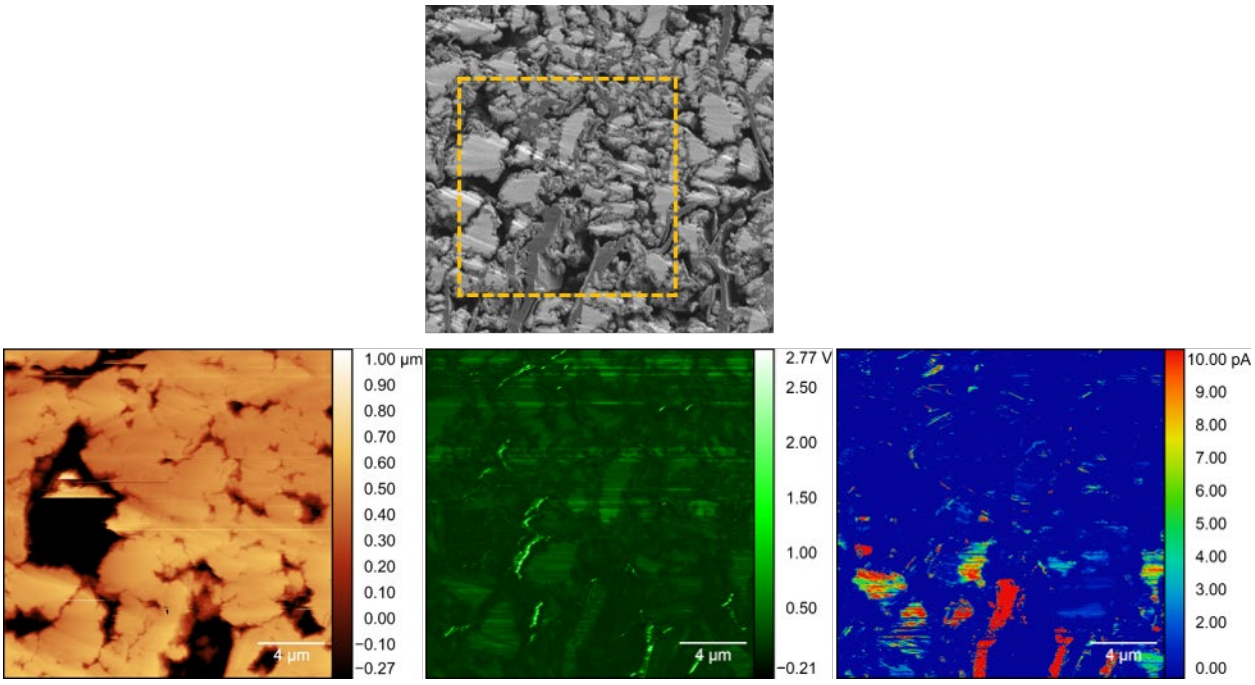

Figure 18. Comparison between SEM and AFM imaging on a cross-section of a 1x PI electrode after 100 cycles. Top row: SEM of imaged area on electrode cross-section. Bottom row: (left) AFM topography map (middle) pull-off adhesion map and (right) PFTUNA map.

2.4 Discussion

2.4.1 Initial Lithiation

In the first formation cycle, the 1 x PI formulation exhibits the highest discharge capacity (**Figure 15**a), lowest charging overpotentials (**Figure 12**a), and highest silicon amorphization (**Figure 15**b). Comparatively, the $^1/_3$ x PI formulation had a similar discharge capacity, a slightly elevated charge voltage profile, but only half the silicon amorphization. We attribute the similarities between the voltage profiles to similar levels of total porosity and electrical conductivity in both electrodes in the pristine state (**Figure 5** and **Figure 9**). The low rate of silicon amorphization indicates that the utilized silicon is charged to approximately twice the lithium concentration (Fig. S5). We believe this contributes to the elevated charging overpotentials observed in the low binder electrodes, compared to the 1 x PI electrodes. Although the high porosity in the low binder formulation should allow for good electrolyte and lithium-ion access to the silicon particles, we hypothesize that the particles are only loosely electrically connected, so that only a small fraction of particles remain accessible to the electrons throughout lithiation and concomitant particle expansion, resulting in a high degree of lithiation in these particles.

On the other hand, the 3 x PI formulation comparatively exhibited the lowest discharge capacity, highest charging overpotentials, and lowest rate of silicon amorphization during initial charging. The high charging overpotentials indicate higher internal resistances, which can be traced back to the low electrode porosity and electrical conductivity measured in the pristine electrodes (**Figure 5** and **Figure 9**). The high internal resistances also suggest a lack of particle accessibility to electrons and lithium-ions, due to excess binder. Analysis of our XRD data suggests that the amorphized portion of the silicon in the high binder formulations was lithiated to a greater degree at formation (**Figure 16**). We believe the lack of particle accessibility made it kinetically favorable to lithiate the accessible particles to a greater degree, leading to the low rate of silicon amorphization. The high binder formulation also exhibited a significantly lower ICE

than the other two formulations (**Figure 11**). We propose that this is caused by the large overpotentials driving a greater degree of SEI formation, as Michan et al. have reported that SEI formation is exacerbated by lower potentials relative to Li/Li^{+}[127]. Characterization of the differences in SEI composition, structure, properties, and evolution with cycling as a result of electrode binder content could be the subject of a future study.

2.4.2 Cycling and Capacity Retention

The cycle life testing shows that capacity retention significantly improves with increasing binder content (**Figure 11**).

The low binder electrodes exhibited the fastest capacity fade, reaching 80% capacity retention at 53 cycles, on average. We believe the root cause of the capacity fade is insufficient binder content and lack of mechanical integrity. In other studies, altering binder chemistry to improve electrode mechanical integrity has been correlated to improved cycling stability in silicon composite electrodes.[128–130] We find a similar effect when binder content is altered. Our mechanical testing showed that lack of binder content significantly hampered electrode adhesion and cohesion (**Figure 7**). As the low binder content electrode is cycled, the lack of mechanical integrity causes silicon particles to disconnect from the functioning electrode matrix. These morphological changes also expose additional silicon surface to the electrolyte, causing SEI growth and irreversible electrode thickness increase, which are both observed to be most severe in the low binder formulation in our SEM imaging (**Figure 4**). By the 100^{th} cycle, the charging overpotential of the low binder electrode surpasses both the 1 x and 3 x PI electrodes throughout the entire charging cycle (**Figure 12**), consistent with increased overall resistances due to SEI growth and disconnected particles.

On the other hand, capacity retention significantly improved when increasing the binder content from 1 x to 3 x (169 to 213 cycles to 80% capacity retention). We believe this to be for two reasons: increasing binder content improves the electrode's ability to maintain mechanical

integrity, while limiting electrode capacity and cathode degradation due to increased internal resistances. The scratch and peel tests indicated that electrode cohesion and adhesion improved with increasing binder content (**Figure 7**), which has been correlated to improved capacity retention in literature[48,122]. In addition, the SEM imaging of cycled electrodes (**Figure 4**) shows that irreversible electrode thickness changes were restricted with increased binder content, demonstrating the effect of improved mechanical integrity. Increasing binder content also reduced electrode porosity and increased binder layer thickness on the electrode particles. Large internal resistances from the decreased porosity and electrical conductivity in the high binder electrode increase charging overpotentials and limit the degree of lithiation in the electrode, which in turn limits particle expansion and SEI growth. Anode overpotentials directly affect the voltages experienced on the cathode side. In full cell cycling, only the cell voltage ($E_{cell} = E_{cathode} - E_{anode}$) is controlled. If overpotentials on the anode side are high, the cell voltage would reach the cutoff potential earlier, and cathode voltages will be limited. Limiting cathode voltages will not only limit cell capacity, but could also limit cathode degradation in the high binder electrodes[131–135]. High binder content also contributes to increasing the composite electrode stiffness and works to suppress irreversible thickness changes. Silicon composite electrodes with lower irreversible thickness changes during cycling have been correlated to improved capacity retention, which is consistent with our observation[60,113,130].

Our XRD analysis reveals that silicon utilization in our electrodes evolves with cycling (**Figure 15**). After 50 cycles, the absolute percentage of silicon amorphization decreases with increasing binder content. We propose that having a larger amount of fresh silicon available improves capacity stability, as we observed in the high binder electrodes. Between the 1st and 50th cycles, silicon amorphization increased by 200% in the high and low binder electrodes, but only by 75% in the 1 x PI electrodes. The increase in silicon amorphization with cycling suggests that morphological changes in these electrodes during cycling enabled fresh silicon to become accessible, lithiated, and amorphized. As XRD is a bulk analysis technique, we cannot probe the distribution of silicon amorphization in the particles and throughout the electrode. In other

words, we cannot discern whether lithium is penetrating more deeply into the crystalline cores of partially amorphized silicon particles or if previously unlithiated particles are being accessed. We hypothesize that the level of thickness expansion that the electrodes can sustain before new particles become accessible and lithiated varies with binder content and is related to capacity retention ability. Future experiments utilizing techniques capable of mapping silicon utilization throughout the electrode could help to elucidate the mechanisms which drive changes in silicon utilization with cycling.

AFM-PFTUNA mapping of the local electrical conductivity in cycled electrodes reveals the network of electronic connections within the electrodes (**Figure 17**). The electrical network in both the cycled 1 x and 3 x PI electrodes contain both GNP and Si particles, while electrical network in the cycled $^{1}/_{3}$ x PI electrode only corresponds to the GNP particles. The lack of silicon in electrical network indicates that the silicon in the low binder electrodes may not be easily accessible to electrons after cycling. When comparing the cycled 1 x and 3 x PI electrodes, the voltage signal in the 1 x PI electrode is significantly more pronounced and distributed, indicating that the high binder content exacerbates issues with electrical connectedness throughout the electrode, consistent with the high charging overpotentials measured in these electrodes (**Figure 12**).

2.4.3 Rate Testing

In rate testing, the 1 x PI formulation exhibited the optimal rate capability, showing that this formulation achieved an optimal balance between having sufficient binder content to maintain mechanical integrity and providing porosity and electrical conductivity for effective lithium ion and electron transport. With high binder content, large overpotentials result in lower charge capacities, especially at high rates. This finding is similar to Landesfiend et al.'s observation in graphite anodes that higher binder content results in higher binder layer thickness, higher tortuosity, and ultimately, poorer rate capability[112]. On the other hand, the low binder formulation achieves similar discharge capacity to the 1 x PI formulation during early

cycling, but quickly fades throughout the test. We believe this is attributed to insufficient binder content to maintain electrode integrity throughout cycling, resulting in capacity loss.

2.5 Conclusions

The electrochemical performance of silicon anodes is strongly dependent upon the binder content in the formulation. We have observed that increasing binder content will decrease porosity and increase electrode resistances but improve electrode cohesion and adhesion. As such, a trade-off between electrode impedances and mechanical robustness must be balanced to achieve optimal electrode performance. With cycle life and rate testing, we observe that changes in binder content can influence capacity retention rates and degradation mechanisms. With insufficient binder content, several factors contribute to electrode degradation. During early cycles, electrodes with low binder content can attain the expected gravimetric capacity due to acceptable porosity and electronic impedances. However, electrodes with insufficient binder quickly decay due to an inability to maintain mechanical integrity in the electrode. This results in loss of connection with some silicon particles which causes deeper lithiation of the accessible silicon particles, leading to greater silicon volume expansion, SEI growth, and increases in internal impedances. On the other hand, electrodes with high binder content exhibit significantly improved capacity retention, but the large internal resistances from a lack of porosity and electrical conductivity result in large overpotentials during charging, limiting electrode capacity and SEI growth. In applications where capacity retention is the main design objective, our work suggests that high binder formulations are advantageous.

When considering rate performance, we observe that a balance between particle accessibility (both electronically and ionically) and mechanical robustness is needed to achieve optimal performance. Insufficient binder caused electrode degradation even during rate testing, while excess binder impeded access to silicon particles and resulted in lower charge capacities and rate sensitivity. **Error! Reference source not found.**a illustrates the trade-off between several key electrochemical performance metrics and binder content for the silicon electrodes

that we have tested. **Error! Reference source not found.**b shows the gravimetric energy density of the electrodes, on a total electrode weight-basis. At beginning-of-life, the 10 wt% PI electrode exhibits the greatest gravimetric energy density, but with additional cycling, a higher polyimide content of 12.2 wt% is beneficial and shows greater stability from the 3rd to 200th cycle.

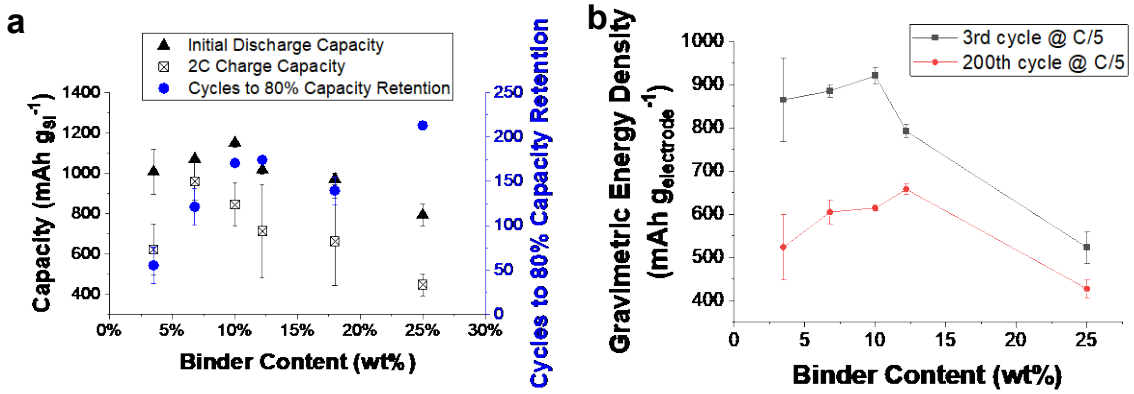

Figure 19. Electrode capacity (a) (left axis) and capacity retention (right axis) and gravimetric energy density of the electrode (b) vs. binder content.

Our results indicate that binder content in silicon anode formulations can significantly impact electrode performance, lithiation/delithiation kinetics, and degradation mechanisms. Our study, which used commercially relevant loadings and full-cell integration, provides insight towards both optimizing and finding acceptable limits for binder content in electrode formulations.

Chapter 3 Influence of Conductive Additive Content

3.1 Introduction

For successful operation of lithium-ion batteries, both electrical and ionic conductive pathways are required[136–138]. In electrodes with electrically insulating active materials, such as layered metal oxide cathode materials and silicon anodes, conductive additives, typically carbon black or other large surface area carbon particles, are added to facilitate electron transport. In the electrode, the conductive particles are situated in between the active material particles, and all particles in the electrode are held together by the binder.

Significant research has been conducted on optimization of electrode morphology through formulation on cathode electrodes. Lithium-ion cathode materials have low gravimetric capacities (< 300 mAh g^{-1}), necessitating thick electrodes to maximize volumetric energy density[139]. But as electrode loadings increase, transport resistances through the thickness of the electrode structure also increase, impeding lithiation/delithiation reactions and limiting rate capability and cycle life[140–142].

The composition and morphology of the conductive matrix play a significant role in shaping not only the electrical pathways, but also the ionic pathways—both of which can significantly impact electrode performance, particularly rate performance[137,138,143]. The morphology of the conductive matrix is affected by processing conditions and mixing order, binder chemistry, conductive additive morphology, and formulation[138,144–147]. Selecting the optimal formulation is critical to achieving optimized electrode performance. Increasing the conductive carbon content in the electrode formulation can increase the rate of ionic resistance increase with electrode loading[143]. Further, a balance between the binder and conductive additive content is necessary to optimize active material utilization and enhance rate capability[138].

For anode electrodes, silicon has great potential to increase energy density and rate capability in lithium-ion batteries. This is primarily due to the high gravimetric energy density of silicon, compared to conventional graphite, enabling thinner electrodes and reducing resistances[148]. As in any electrode, the efficiency of silicon utilization decreases as loading increases. However, Karkar et al. reported that astute selection of the conductive filler morphology, e.g., carbon black, graphite platelets, carbon nanofibers, can extend the maximum loading capability of silicon electrodes[146]. However, their study did not report how the binder ratio was controlled as conductive additive content increased, leaving open to question whether binder content was a factor in determining their results. In addition, many publications have reported on the beneficial effects of additional conductive additive morphologies, including MXene sheets enabling ultra-high electrode loadings[92], carbon wrapped silicon[149], silicon decorated graphite[98], and conformal coatings of carbon on silicon[150,151]. We acknowledge that realization of fast-charge capability[152] in silicon-based electrodes likely also requires improvement of the lithium-ion diffusion rate into silicon via surface engineering[98,153] and electrolyte improvements. However, understanding how formulation affects performance is critical, regardless of the electrode and cell architecture.

The fast-charge potential of silicon has yet to be realized at high mass loadings, as the state-of-the-literature currently falls short of the USABC fast-charge targets of 80% charge in 15 minutes[68]. To enable commercially relevant, high-loaded electrodes (> 4.5 mAh cm^{-2}), effective guidelines for formulation optimization must be established.

In our study, we aim to understand the impact of changing the conductive additive content in silicon microparticle electrode formulations. We created electrodes with varying silicon-to-carbon ratios, maintaining a constant calculated binder layer thickness across the available particle surface area, thereby eliminating the confounding effects of changing binder content. With these electrodes, we tested charge-rate and cycle life performance in Si/NMC622 coin cells. We corroborate our interpretation of the electrochemical performance tests with porosity measurements, initial thickness measurements, electrical conductivity measurements,

and scratch and peel tests to assess mechanical integrity. We utilized X-ray diffraction (XRD) to detect silicon amorphization, thus utilization, and understand how this is affected by the conductive additive content.

3.2 Methods

3.2.1 Electrode Preparation

Our NMC622 cathode and silicon anode electrodes with polyimide (PI) binder was prepared using the same materials and method as described in the previous chapter. We used thin-flake graphite nanoplatelets (GNP H5, xGSciences, particle diameter = 5 μm) as the conductive additive. The binder layer thickness for all electrodes was controlled at 6 nm, based on a calculation that assumes uniform coverage of all available surfaces in the electrode with binder (Appendix A). The formulations we tested are listed in **Table 5**. Silicon loadings were maintained at 3-3.3 mg cm^{-2}.

Table 5: Electrode formulations used in the Conductive Additive Content study

Name	Si vol%	GNP vol%	PI vol %	Si wt%	GNP wt%	PI wt%	Solids Content (%)
Ultra-Low	90.5	2.5	7	93	2.3	4.7	58
Low	85.2	5	9.8	88.5	5	6.5	52
Baseline	75.4	10	14.6	80	10	10	43
High	65.4	14.9	19.6	71	15.3	13.7	42
Ultra-High	44.8	25	30	61	21	18	38

During slurry preparation, slurry solid content was adjusted for each formulation to achieve a coat-able viscosity. Typically, the ideal viscosity range is 10^3 to 10^4 mPa s at a shear rate of 10/s[154,155]. The solid content for the 2.5, 5, 10, 15, and 25 vol% GNP slurries was 58, 52, 43, 42, and 38%, respectively. As the GNP content increases, the total particle surface area in the slurry increases, necessitating additional solvent in the slurry. The solids content the slurries used in this study are also listed in **Table 5**.

Volume percentages are reported based on solid volume only; it excludes consideration of the electrode pore volume. True volume percent, which includes the pore volume, can be obtained by multiplying solid volume percent by (1 minus total porosity percentage).

3.2.2 Porosity Measurement

We report the total porosity of our pristine electrodes, calculated from thickness and weight measurements of a circular punch of electrode coated on copper current collector. The methods and calculation match that provided in the previous chapter.

3.2.3 Scanning Electron Microscopy (SEM)

To prepare cross-sections for scanning electron microscope (SEM) imaging, we milled sections with a broad beam ion miller (Hitachi IM4000 Plus). Cross-sections for imaging were milled at 6 kV for 2 hours. Secondary electron scanning electron microscope images were then taken at 2 kV, 20 uA using a Hitachi S-4800 with ± 40° sample rotation during milling.

3.2.4 Electrical Conductivity

Electrical conductivity measurements were taken using the potentiostatic electrochemical impedance spectroscopy technique (PEIS) on a Biologic VMP-3e. Pristine electrode samples were punched to 12.7 mm diameter and clamped within a CESH-e (Enhanced controlled environment sample holder, Biologic) equipped with gold-coated plates of ½" diameter for measurement of through-thickness impedances. The impedance method sweeps from 1 MHz to 1 Hz with 10 points per decade at 0V vs. open circuit, averaging 3 measures per frequency. A voltage amplitude of 10 mV was used for the 25 and 15 vol% GNP electrodes, while 100 mV was used for the 2.5, 5, and 10 vol% electrodes (**Figure 20**).

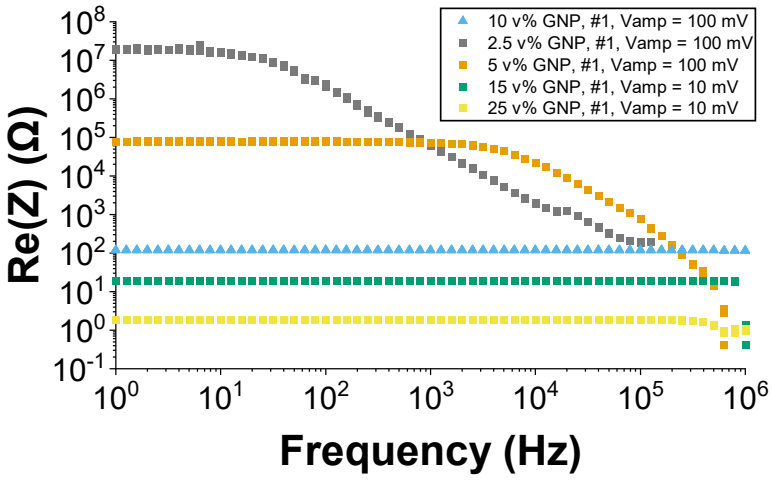

Figure 20. Bode plot of real impedance during PEIS on electrodes with varying GNP content.

The voltage amplitude had to be increased to increase the signal output for electrodes with lower conductivity. We confirmed that the measured response was invariant with voltage amplitude by testing voltage amplitudes of 10, 25, 50, 75, and 100 on the 10 vol % GNP electrodes (**Figure 21**). The measured electrode resistance was invariant with the perturbation voltage amplitude.

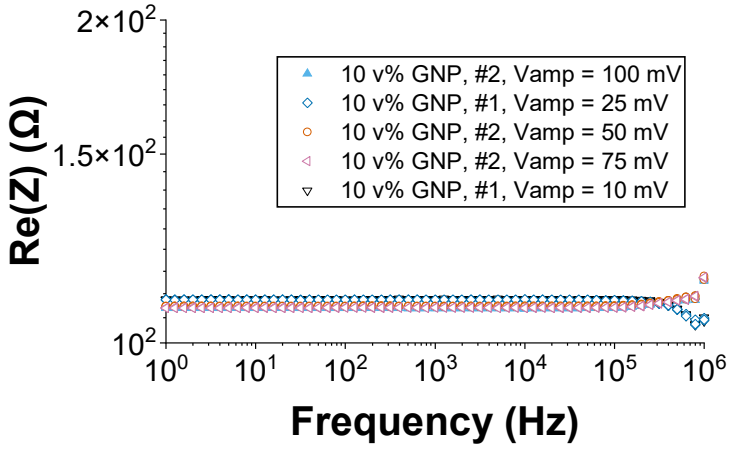

Figure 21. Bode plot of real impedance during potentiostatic electrochemical impedance spectroscopy (PEIS) of the 10 vol% GNP electrodes at various voltage amplitudes. Note the y-axis scale compared to Figure 20.

On a Bode plot of the phase angle, we observe that the phase angle returns to zero at low frequencies (**Figure 22**); thus, resistance values were taken as the y-intercept on the Bode plot of

the real component of the resistance. This resistance value was then converted into conductivity using the measured electrode area and thickness.

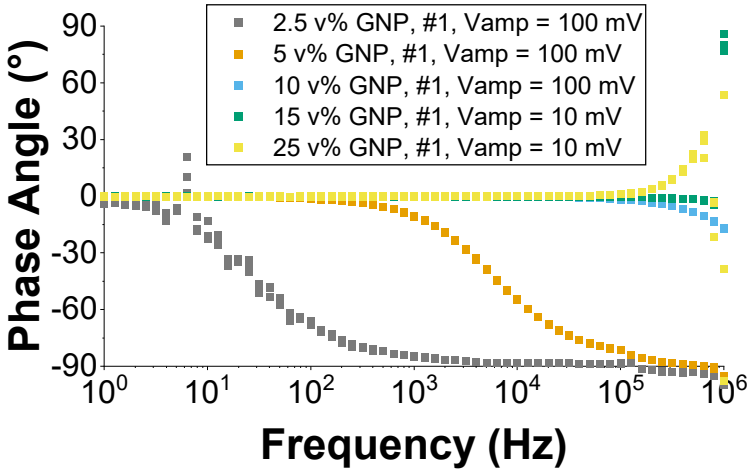

Figure 22. Bode plot of phase angle during PEIS on electrodes with varying GNP content.

3.2.5 Mechanical Testing

We utilized microscratch and 180° peel testing to assess the electrode cohesion and adhesion to the current collector, following the same methods as in the previous chapter. Maximum normal loads were 100, 100, 200, 100, 200 mN for the 2.5, 5, 10, 15, and 25 vol% GNP samples, respectively. Scratch loads were adjusted to ensure sufficient scratching of the electrode, without reaching the depth of the current collector.

3.2.6 Electrochemical Testing

For cycle life and rate testing, full cells were assembled using the silicon anode electrodes (15.3 mm diameter), NMC622 cathode (12.7 mm diameter), Celgard 2325 separator, 40 μL of electrolyte (1.2 M LiPF6 in dimethyl carbonate:fluoroethylene carbonate 4:1 with 2 wt% of vinylene carbonate and 3 wt% of OS3 from Silatronix), a 1.0 mm stainless steel spacer, and a 1.4 mm spring in a CR2032 coin cell. The capacity ratio of the negative to positive electrodes were N/P = 2.00 ± 0.05. Electrochemical tests were conducted on a Maccor cycler. Charge rates were calculated based on the cathode electrode capacity. The galvanostatic cycling protocol consisted

of two formation cycles (CC charge at C/20, CV charge until C/50, CC discharge at C/20) followed by cycling (CC charge at C/3, CV charge until C/20, CC discharge at C/3) between 3.0 and 4.2 V. A 15-minute rest period was employed after each charge and each discharge. The rate testing protocol used the same formation protocol, followed by 5 cycles at C/10, C/5, C/2, 1C, 2C, 5C, and C/5. Discharges were carried out at C/5 when the charge rate exceeded that rate, to ensure that electrodes were sufficiently discharged at each cycle.

To understand silicon utilization in these electrodes, we ran one fixed capacity formation cycle in lithium metal half cells. The half cells consisted of the silicon anode electrode (15.3 mm diameter), lithium metal counter electrode (16 mm diameter, 1 mm thick, MTI Corporation), Celgard 2325 separator, 80 µL of electrolyte (1.2 M LiPF6 in dimethyl carbonate:fluoroethylene carbonate 4:1 with 2 wt% of vinylene carbonate and 3 wt% of OS3 from Silatronix), a 0.5 mm stainless steel spacer, and a 1.4 mm spring in a CR2032 coin cell. The silicon electrodes were lithiated to 1500 mAh g_{Si}^{-1} at C/20, then delithiated to 1.5 V vs. Li/Li^+ at C/20. Voltage traces were checked for indications of lithium plating (negative voltages) before conducting additional post-mortem testing.

3.2.7 X-ray diffraction (XRD)

XRD was conducted using the same method as described in the previous chapter.

3.3 Results

3.3.1 Electrode Structure

The ionic resistance through electrodes is strongly influenced by two factors: electrode thickness and morphology[140–142]. **Figure 23** shows the relationship between electrode thickness and total porosity with GNP content. The electrode thickness increases with GNP content since the silicon loading is held constant in all the electrodes. All electrodes produced for this study showed similar porosity, except for the 25 vol% GNP electrodes, which had much lower porosity.

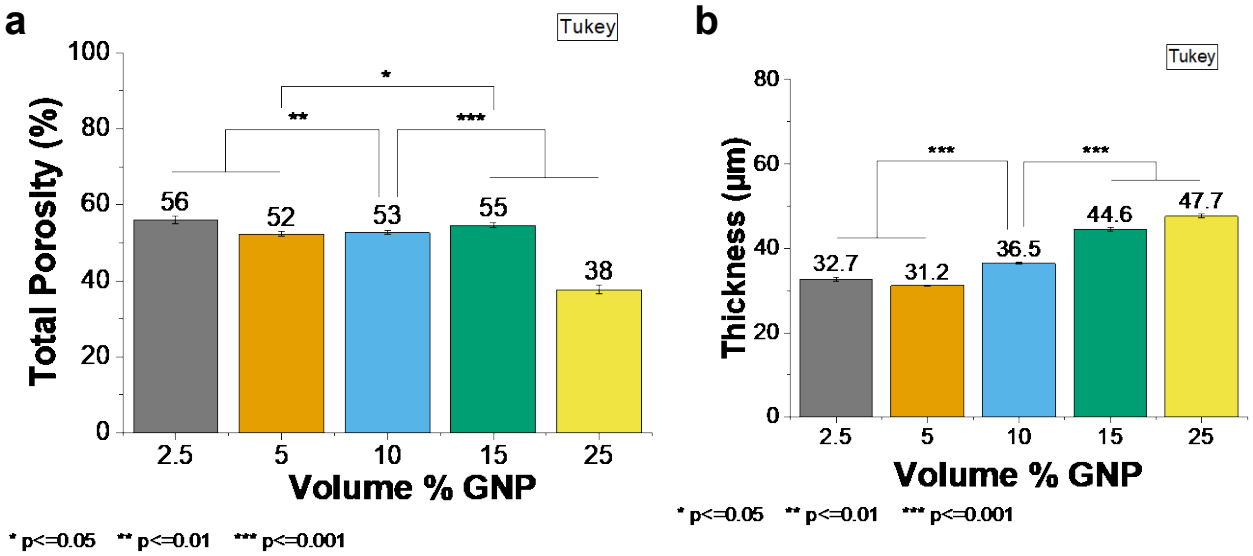

Figure 23. Total porosity (a) and thickness (b) of electrodes with varying conductive additive content.

SEM imaging of the pristine electrodes revealed that at high GNP content, the plate-like shape of the conductive additive particles causes them to preferentially stack together parallel to the current collector (**Figure 24**).

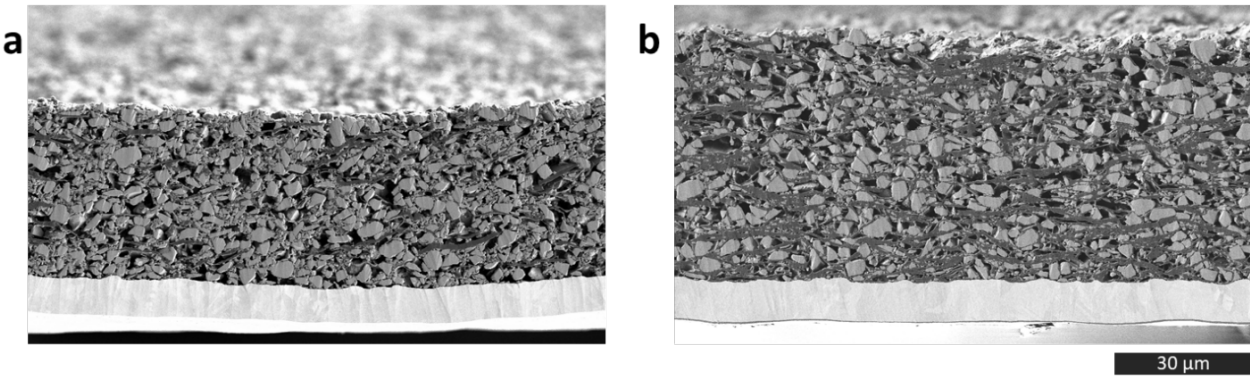

Figure 24. Secondary electron SEM images of cross-sections of pristine electrodes with 10 (a) and 25 (b) vol% GNP, showing more preferential stacking of GNP in the latter than the former electrode.

As the particles stack together, it effectively reduces the particle surface area, increasing the actual binder layer thickness on the particles, thus reducing porosity and restricting ionic conductivity.

3.3.2 Pristine Electrode Properties

Having sufficient electrical conductivity is another functional requirement in battery electrodes. **Figure 25** shows the relationship between electrical conductivity and GNP content. As expected, the conductivity increases with conductive additive content.

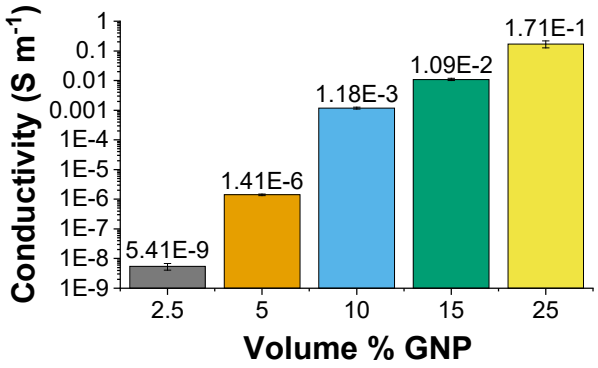

Figure 25. Electrode conductivity of electrodes with various conductive additive content.

The ability to maintain mechanical integrity is another key characteristic in electrodes, particularly with silicon – a high volume expansion material. To understand the impact of how changing the silicon to carbon ratio affects the mechanical behavior of the electrodes, we conducted microscratch and 180° peel testing (**Figure 27**). Although the fracture toughness (K_c) measured in scratch testing significantly varied from sample to sample, we did not observe a clear trend in K_c with conductive additive content. Photographs of the peel test specimens show more residual electrode on the peeled surface with increasing GNP content (**Figure 26**). This indicates that the failure mode gradually changes from adhesive to cohesive with increasing GNP content.

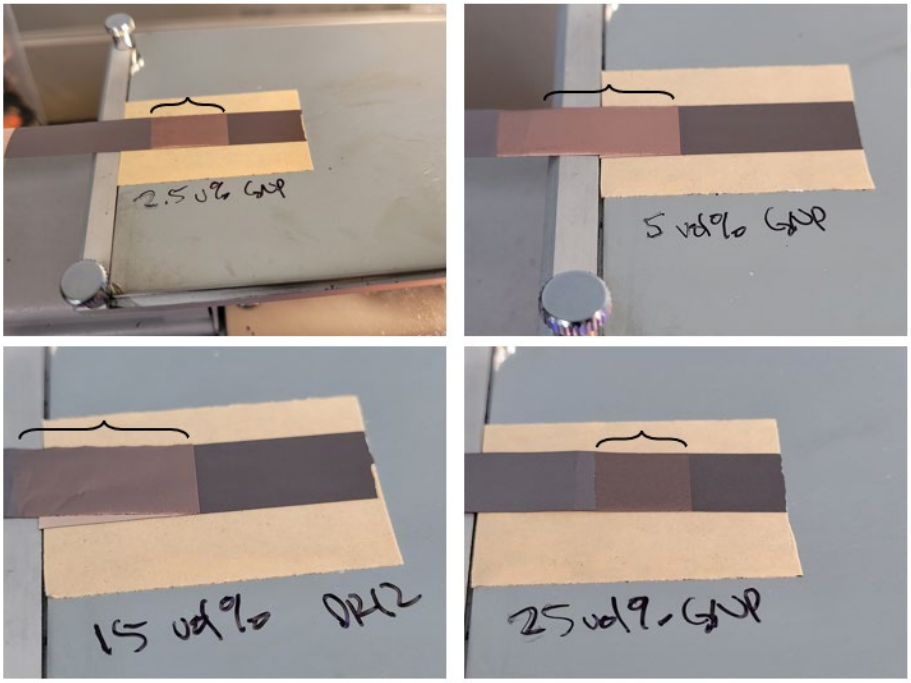

Figure 26. Photographs of peel test surfaces in electrodes with varying GNP content. Peeled area is denoted by the curly bracket.

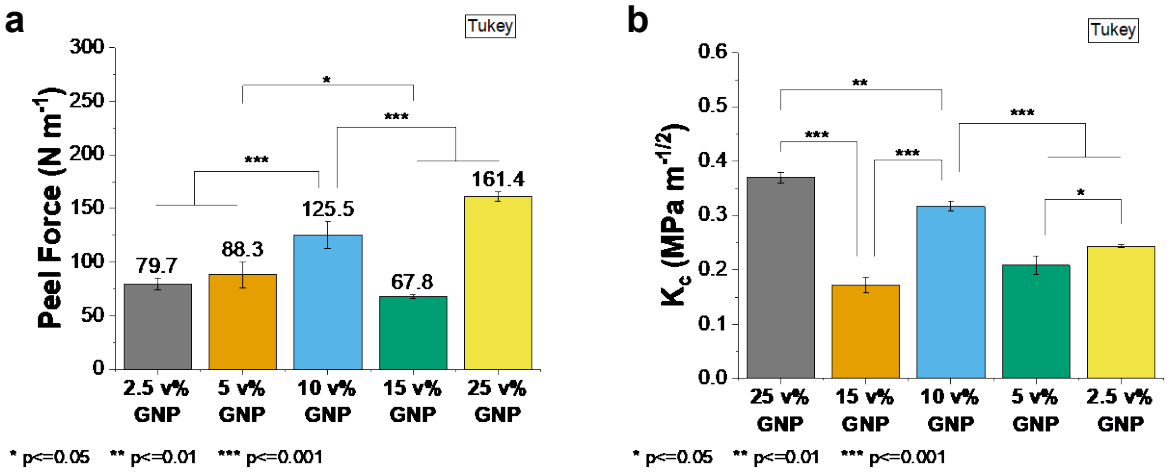

Figure 27. Peel force (a) and fracture toughness from microscratch (b) tests.

In the peel test, the peel force generally increased with conductive additive content. However, the 15 v% GNP electrode exhibited uncharacteristically lower peel force than the other samples. A replicate electrode was tested, which confirmed this result (**Figure 28**).

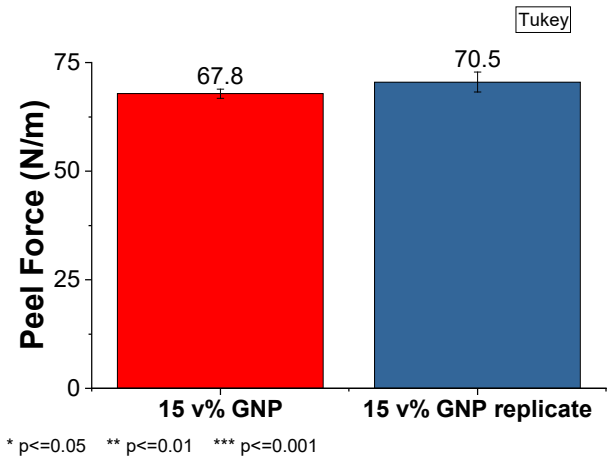

Figure 28. Peel force comparison between two electrodes of the same formulation.

3.3.3 Electrochemical Performance

We then conducted cycle life and charge rate testing to assess the impact of changing the conductive additive content. **Figure 29** shows discharge capacity in the C/3 cycle life test of electrodes with varying GNP content. A plot of the coulombic efficiencies is shown in **Figure 30**.

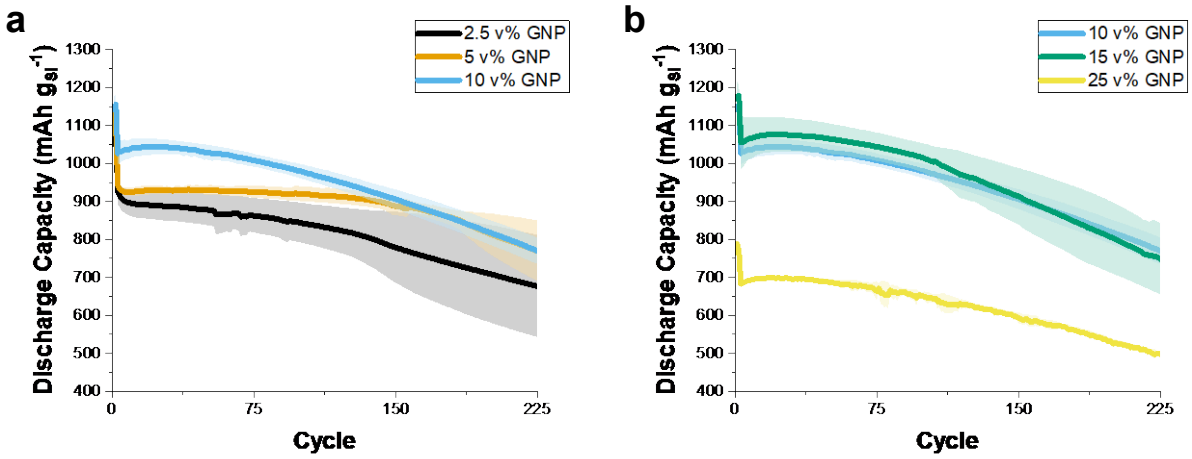

Figure 29. Discharge capacities in C/3 cycle life testing for electrodes with ≤ 10 vol% GNP (a) and ≥ 10 vol% GNP (b).

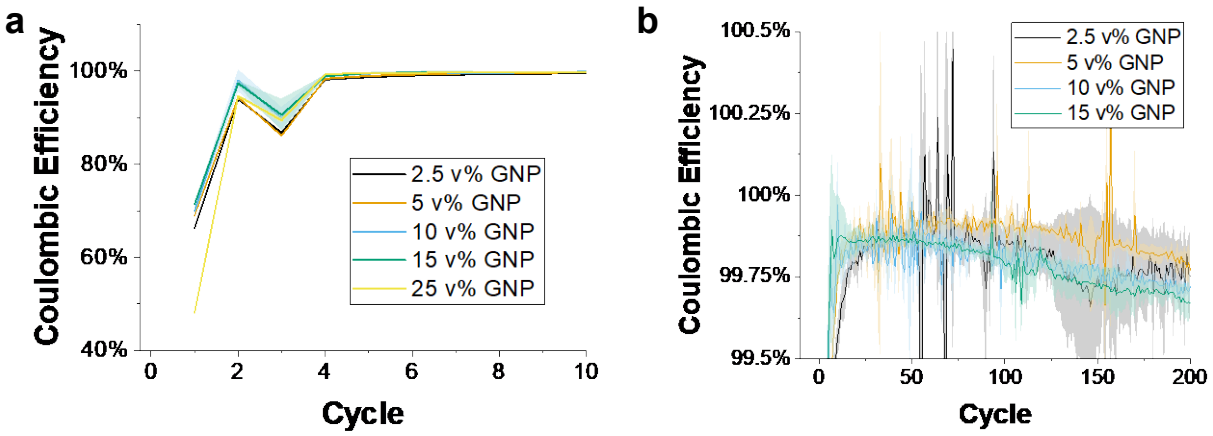

Figure 30. Coulombic efficiency during C/3 cycle life testing for the first 10 cycles (a) and cycles 1 to 200 (b) for electrodes of varying GNP content.

Figure 31 shows the initial coulombic efficiency (ICE), initial discharge capacity, and number of cycles to 80% capacity retention.

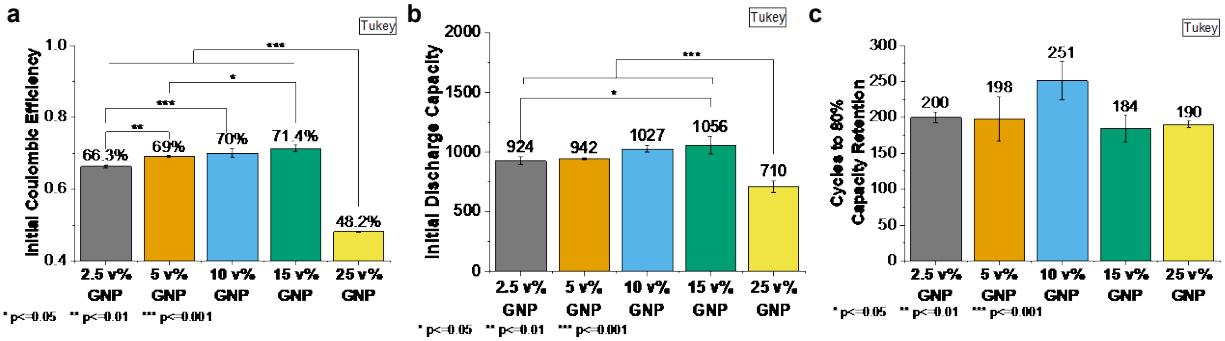

Figure 31. Initial coulombic efficiency (a), initial discharge capacity (b), and number of cycles to 80% capacity retention (c) in the C/3 cycle life test of electrodes with varying conductive additive content.

Figure 32 shows the rate performance of the cells on a semi-log plot. The 15 volume % GNP electrode shows the best charge capacity of all the electrodes at every rate tested, while the 25 volume % GNP electrode was the worst performer at all charge rates.

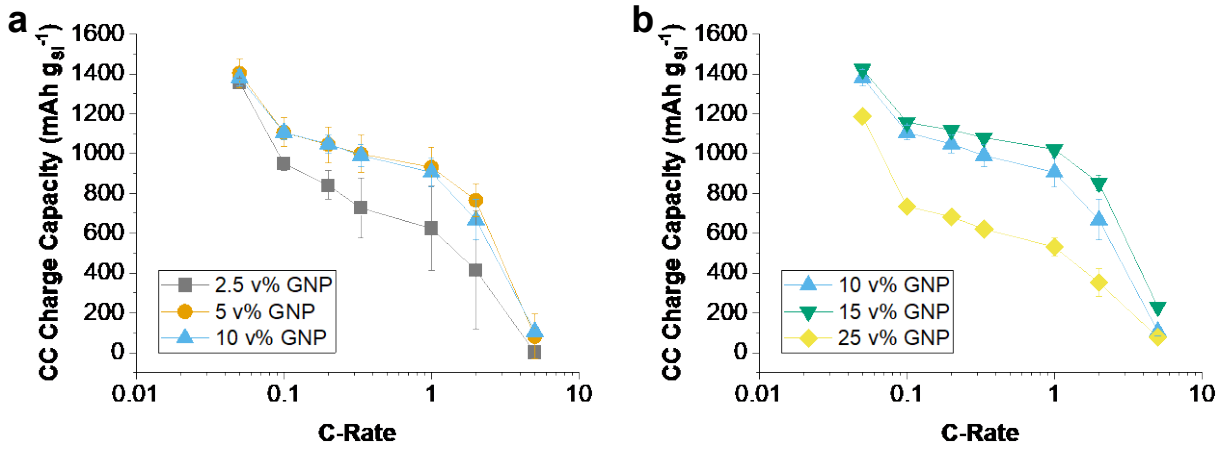

Figure 32. Constant current charge capacity in fast charge testing for electrodes with ≤ 10 vol% GNP (a) and ≥ 10 vol% GNP (b).

To better understand the charging dynamics in each electrode type, we have plotted the first 2C charge voltage profile for the electrodes in **Figure 33**. The 2.5 and 5 vol% GNP electrodes showed a reversal in overpotentials during charging, indicating insufficient electrical conductivity at fast charging speeds.

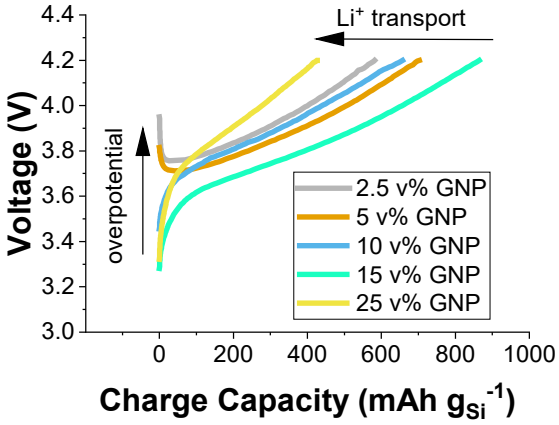

Figure 33. Voltage profiles of the first 2C charge for one cell of each level of GNP content.

3.3.4 Post-Mortem Analysis of Silicon Utilization

To understand how the conductive additive content affects silicon utilization, we lithiated the silicon electrodes in half cells to 1500 mAh g_{Si}^{-1} and delithiated to 1.5 V. We checked for lithium plating by looking for negative voltages during half cell discharge. We observed very

minimal lithium plating in the 2.5 vol% GNP electrodes (<0.01 mAh cm^{-2}). None of the other electrodes exhibited signs of lithium plating. Minimum voltages during lithiation and plated capacities are listed in **Table 6** below.

Table 6: Minimum voltages and plated capacities during half-cell lithiation to 1500 mAh gSi-1

Volume % GNP	Minimum Voltage during Lithiation *(mV)*	Lithium Plating Capacity *(mAh cm^{-2})*
2.5	-0.154	0.002
2.5	-13.827	0.005
2.5	-16.497	0.005
5	34.965	0
5	38.566	0
5	54.101	0
10	61.142	0
10	48.166	0
10	56.216	0
15	26.297	0
15	49.086	0
15	55.675	0
25	29.879	0
25	20.819	0
25	21.587	0

The ICE of the half cells mirrored the trend observed in full cells (**Figure 34**), i.e., the ICE increased with GNP content until 25 vol% GNP, where the ICE was significantly lower.

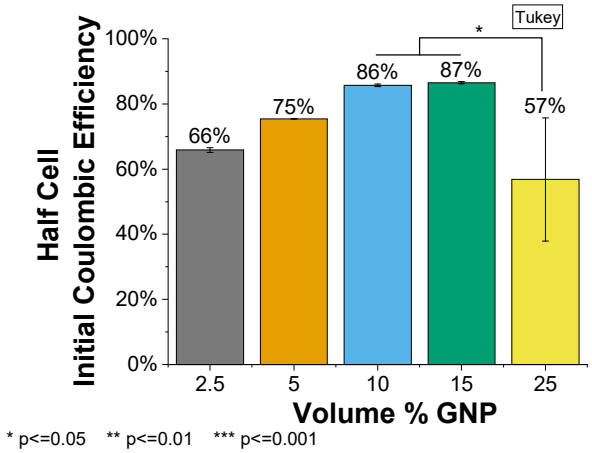

Figure 34. Initial coulombic efficiencies of half cells lithiated to 1500 mAh gSi-1 in electrodes with varying GNP content.

Afterwards, we disassembled the cells for XRD to determine the amount of silicon that became amorphized during lithiation, using the same method as in our previous publication[156]. We observed that the silicon amorphization decreased with GNP content (**Figure 35**a). As an indication of the degree of lithiation in the electrodes, we monitor the cell voltage after the 15-minute open circuit rest after lithiation (**Figure 35**b).

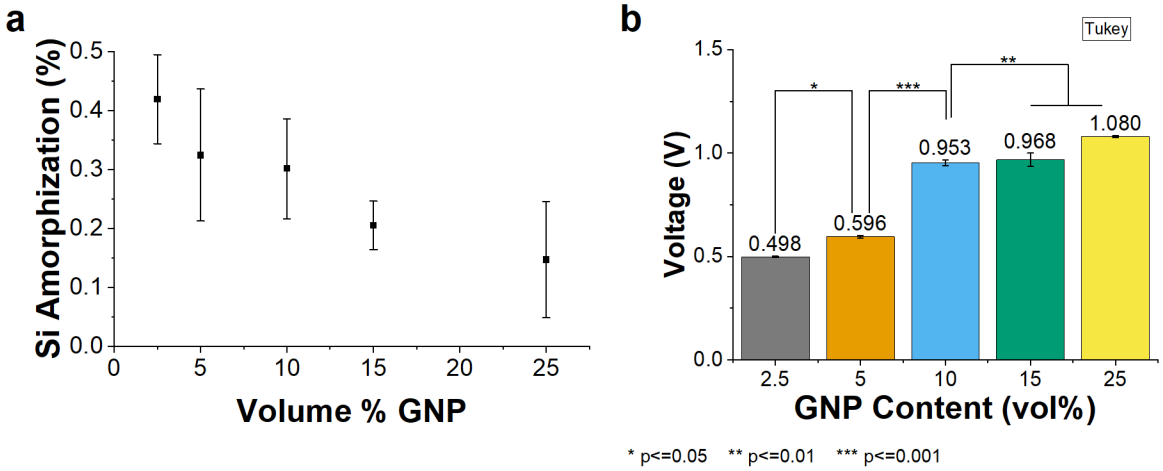

Figure 35. Percentage silicon amorphization after lithiating to 1500 mAh g_{Si}^{-1} (a) and cell voltage after open circuit rest after lithiation (b) in electrodes with varying GNP content. Error bars represent standard deviation.

3.4 Discussion

Comparison of the pristine electrode properties with the electrodes' performance in cycle life and fast charge tests help to build understanding of the relationship between electrode

structure, properties, and performance. This knowledge can ultimately inform product specifications and guide future development.

3.4.1 Mechanical Behavior

Performance in the peel and scratch tests are indicators of an electrode's ability to maintain connections to the current collector and between particles. Although we only ran mechanical tests on pristine electrodes, the results can still be indicative of the electrode's performance with cycling.

First, we note that the range of peel force and fracture toughness measured in this set of electrodes is much smaller than the range we measured in our previous work when binder content was varied[156] (**Table 7**). This indicates that binder content has a stronger influence on mechanical integrity than the Si/C ratio. In addition, we did not observe a monotonic relationship between GNP content and either peel force or fracture toughness (**Figure 27**).

Table 7: Comparison of fracture toughness and peel force ranges measured in this and previous work

	Range of Fracture Toughness *(MPa $m^{-1/2}$)*	Range of Peel Force *(N m^{-1})*
Chapter 2	0.1 – 1.1	50-400
Chapter 3	0.15 – 0.35	60-170

Our microscratch test shows significant differences in fracture toughness from electrode to electrode, but no monotonic trend with GNP content. Although the fracture toughness between the specific materials we tested is not reported, a literature search confirms that the fracture toughness between polyimide/silicon and polyimide/graphite are in a similar range: 103±12 J m^{-2} for silicon-polyimide[157] and 145-180 J m^{-2} for graphite fiber-polyimide[158].

Our peel results nearly show a monotonic increase with GNP content, except for the 15 vol% GNP electrodes. The plate-shaped GNP tends to preferentially orient parallel to the current collector. With increasing GNP content, a larger fraction of the particles become oriented in this way, increasing the contact area between the electrode and the current collector increases. Since

the binder coats the outer surface of the particles, greater contact between the particles and current collector leads to increased peel force. As for the 15 vol% GNP electrode, one possible explanation for its low peel force is the increase in electrode thickness. In the literature, thin film peel force has shown dependence on substrate thickness, since some of the peel force goes into stretching the coating before peeling[159]. With a thicker coating, more force will be required to stretch the electrode coating before peeling at the interface between the copper and electrode begin. It is unclear why this effect is less pronounced for the other electrodes, e.g., from 5 to 10 vol% GNP. Additional tests could help to understand this observation, i.e., measurement of coating modulus, quantitative comparison of GNP particle orientations.

3.4.2 Fast-Charge Capability

Comparing the rate performance (**Figure 32**) with the porosity, thickness, and conductivity (**Figure 23** and **Figure 25**) of the pristine electrodes, we glean several learnings regarding the performance trade-offs from electrode morphology.

Improvements in electrical conductivity correlate with improvements in rate performance only at low conductivity levels. With low GNP content, we observe significant improvements in the rate performance between the 2.5 and 5 vol% electrodes (**Figure 32**a). These electrodes had similar initial porosity and thickness, but the electrical conductivity improved by three orders of magnitude with more GNP content (**Figure 25**). Improvements in electrical conductivity in these electrodes translated to significant improvements in charge rate capability.

On the other hand, the 5 and 10 vol% GNP electrodes exhibit similar rate capability (**Figure 32**a), despite exhibiting three orders of magnitude difference in electrical conductivity (**Figure 25**). This indicates that there is a threshold level of workable electrode conductivity, above which electrodes can achieve acceptable rate capability. In line with the literature, improvements in electrical conductivity do not necessarily lead to improvements in fast-charge performance[136].

Above this threshold, other parameters, i.e., electrode porosity and thickness, become more important in determining fast-charge performance. Increases in electrode thickness increase the ionic path length and ionic resistances to lithium-ion transport, hampering the electrodes' rate capability[141]. Decreasing connected porosity will further increase the ionic path length by increasing the ionic path tortuosity through the electrode.

We compare the relative influence electrode thickness and porosity on the ionic resistances through the electrode. For ionic conduction, previous publications describe that ionic resistance is linearly related to thickness and tortuosity and inversely related to porosity (eq. 5)[148]

$$R_{ion} = \frac{\tau t}{\varepsilon A \kappa}$$

eq. 5

, where τ is the electrode tortuosity, t is the electrode thickness, ε is the electrode porosity, A is electrode area, and κ is the electrolyte conductivity.

However, X-ray tomographic studies indicate that tortuosity is related to porosity by approximately a power-law relationship[160–162], with increasing porosity resulting in decreasing tortuosity. In addition, the anisotropic particle shape of the GNP more negatively influences through-plane tortuosity[162]. Therefore, the influence of electrode porosity on ionic resistances is larger than the influence of thickness. We observe this clearly when we compare the change in performance between the 10 and 15 vol% electrodes vs. the 15 and 25 vol% electrodes. Between 10 and 15 vol%, there was a 22% thickness increase and similar porosity, yet rate performance improved by 28% at 2C. In comparison, the porosity reduction of 30% with just a 7% thickness increase resulted in a 50% reduction in constant current charge capacity at 2C between the 15 and 25 vol% GNP electrodes.

By examining the voltage profiles during fast charging, we further observe the effects of the pristine electrode properties on charging (**Figure 33**). The overpotentials at the start of charging decrease as electrical conductivity increases, while the maximum constant-current charge capacity is limited by lithium-ion transport resistances. Similar observations have been

made in the literature[141]. In the 2.5 and 5 vol% GNP electrodes, we observe an initial drop in cell potential during charging, which we believe is an indication of very high overpotentials on the anode. This indicates the minimum electrical conductivity threshold for good performance at 2C is somewhere between 10^{-6} and 10^{-3} S m^{-1}, the conductivities for the 5 and 10 vol% GNP electrodes. When we consider the electrode porosity, the true vol% of GNP in these electrodes would be 2.2 and 4.8 true vol%, respectively. These volume fractions are within the range of experimentally determined percolation limits of GNP polymer composites in published literature[163] and within the range of percolation limits predicted by the Li-Kim model[164]. The diameter to thickness ratio (D/t) for the conductive additive particles used in this work is 5 μm / 15 nm = 333.

The 15 vol% GNP electrodes exhibited the lowest overpotentials during initial charging. It also exhibited the highest CC charge capacity at all rates, indicating that it had the least ionic transport resistances. Despite exhibiting low overpotentials during initial charging, the 25 vol% GNP electrodes had the lowest constant current charge capacity at 2C, due to the ionic transport resistances from low porosity and high electrode thickness.

3.4.3 Cycle Life Performance

We compare pristine electrode structure and properties with performance during long-term cycling. During initial cycling, we observe trends similar to those observed in rate testing. However, long-term cycling stability showed no correlation to mechanical behavior or other electrode properties.

The ICE increased with conductive additive content from 2.5 to 15 vol% GNP (**Figure 31**a), similar to previous reports in literature[138,146]. Although increasing the conductive additive content increases the available surface area for SEI formation, this is not the main effect on ICE. Rather, increasing the conductive additive content reduces the probability of particle disconnections during delithiation, which improves the rate of lithium recovery and coulombic efficiency. At 25 vol% GNP, the ICE dropped significantly. We attribute this to the low porosity

and poor ion accessibility, which increases the likelihood of trapped lithium. The initial discharge capacities followed the same trends as were observed in rate testing (**Figure 31**b).

The initial discharge capacity—the discharge capacity in the first C/3 cycle – followed the same trend observed in rate testing (**Figure 31**b). Interestingly, during cycle life testing, the 5 vol% GNP electrodes showed lower capacity than in the rate testing. We do not have an explanation for the observed differences but point to the larger capacity variation at each C-rate in 5 vol% GNP electrodes than in the 10 vol% electrodes during rate testing as a possible explanation.

To evaluate cycling stability, we track the number of cycles it takes to reach 80% of the initial discharge capacity (**Figure 31**c). To our surprise, this statistic showed no sensitivity to the GNP content, with none of the electrodes exhibiting significantly different capacity retention. Previous studies have proposed that improving the electrode mechanical integrity improves cycling stability, whether through binder selection or conductive filler selection[58,113,114,146,156]. As we did not observe large changes in mechanical behavior with changing GNP content, it is unsurprising that the cycling stability of our electrodes also did not exhibit significant differences. This suggests other factors, such as binder content and electrolyte selection, have greater influence on cycling stability.

We calculate the gravimetric energy density of the electrodes, on a total electrode weight basis to evaluate the efficacy of GNP content in terms of gravimetric energy density enhancement in **Figure 36**. The 5 vol% GNP electrodes show the most stability in gravimetric energy density with cycling. This electrode also exhibited comparable rate performance as the 10 and 15 vol% electrodes (**Figure 33**), suggesting that 5 vol% may be near the optimal GNP content for this set of electrode materials.

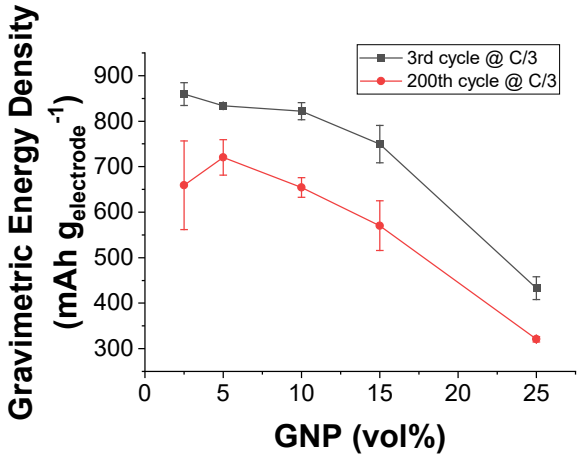

Figure 36. Total gravimetric energy density of electrodes with varying GNP content after 3 and 200 cycles.

3.4.4 Silicon Utilization

To further elucidate the impact of changing GNP content on electrode performance, we used XRD to probe silicon utilization. All electrodes were charged to the same capacity limit, i.e., 1500 mAh g_{Si}^{-1}, then delithiated to 1.5 V before post-mortem XRD. We hypothesized that increasing GNP content would improve particle-to-particle electrical connections, keeping more silicon particles connected and participating in lithiation/delithiation. Interestingly, silicon amorphization decreased with increasing GNP content (**Figure 35**).

To contextualize this result, we compare the kinetic barriers to silicon amorphization in a composite electrode. Lithium-ion diffusivity through electrolyte is on the order of 10^{-6} cm^2 s^{-1} [165,166], while diffusivity through silicon is on the order of 10^{-12} to 10^{-13} cm^2 s^{-1} at room temperature[167–170]. As expected, diffusion through the solid silicon is much slower than diffusion through the liquid electrolyte. However, the current of lithium ions at the silicon particle surface is constricted by the porosity and tortuosity of composite electrodes[171,172]. A lower porosity and higher tortuosity would reduce the contact area for lithium-ion flux to the silicon particle surface, increasing the lateral diffusion distances required to fully lithiate the silicon. Therefore, we expect reducing particle accessibility to strongly limit silicon amorphization.

Our measurement of silicon amorphization using XRD supports that silicon particle accessibility controls silicon amorphization. The electrodes with lower GNP content were

thinner and more porous, resulting in better silicon accessibility and more amorphization measured in XRD (**Figure 35**a). As the GNP content increases, silicon particle accessibility decreases along with silicon amorphization. The voltages after the open-circuit rest period after lithiation reflect the average silicon lithiation in the electrodes (**Figure 35**b). Lower voltages indicate higher degrees of lithiation[173,174]. We note that the minimum voltage during lithiation is not a good indicator of the degree of lithiation, as that voltage includes charging overpotentials, which are electrode formulation dependent. The electrodes with lower GNP content achieved a lower voltage after lithiation than the electrodes with higher GNP content. This again indicates that improving particle accessibility increases the average degree of lithiation.

The trend in ICE reveals the conductive additive's role during delithiation. The ICE of the half-cell electrodes (**Figure 34**) followed the same trend as was observed in our full cells (**Figure 31**a). During delithiation, the silicon particles decrease in volume, causing the electrode to crack and thickness to shrink[114,175]. These massive morphological changes in the electrode can increase the probability of silicon particle disconnection, resulting in trapped lithium[176,177]. Our results show that having higher GNP content decreases the chance of particle disconnection during delithiation, thereby increasing the coulombic efficiency. This trend holds until the conductive additive content becomes excessively high, as in the 25 vol% GNP electrodes. In this case, the increase in ionic path length due to lack of porosity results in trapped lithium during discharge and a very low coulombic efficiency. Our observations indicate that maintaining particle connectivity and ion conduction pathways are the main drivers of efficient delithiation.

3.5 Conclusions

We have studied how varying the conductive additive content affects electrochemical performance in silicon microparticle electrodes for lithium-ion batteries.

The proportion of the GNP conductive additive in the electrode formulation affects both the electrical and ionic conductive pathways throughout the electrode. As the GNP content increases, electrical conductivity also increases, which is beneficial to electrode function.

However, increasing the inactive material content necessitates an increase in electrode thickness to maintain the same active material loading. This increases the ionic path length and decreases capacity and rate performance. Additionally, at high GNP loadings, the plate-like shape of the conductive particles tends to stack together and preferentially orient parallel to the current collector. The stacking effectively reduces the particle surface area, thereby reducing porosity by closing pores and increasing the binder layer thickness. The loss of porosity inhibits particle accessibility and negatively affects the electrode capacity and rate performance.

180° peel and microscratch tests of the pristine electrodes reveal that the silicon-to-carbon ratio does not correlate to changes in the electrodes' ability to maintain mechanical integrity. Other factors, such as binder layer thickness, binder chemistry, and particle surface chemistry play a larger role in determining the mechanical properties of the electrode. Cycling stability is often related to the electrodes' ability to maintain their mechanical integrity. As the conductive additive content did not largely affect this property, we accordingly did not observe any correlation between long term cycling stability and conductive additive content.

Diffraction techniques helped us to further understand the role of the conductive additive in silicon utilization. Post-mortem XRD on silicon electrodes lithiated to a fixed capacity limit reveal that as GNP content increases and silicon particle accessibility decreases, silicon utilization also decreases. However, during delithiation, increased GNP content reduces the likelihood of disconnected silicon particles and trapped lithium, increasing the coulombic efficiency with conductive additive content.

- Our study indicates that there is a threshold of electrode electrical conductivity, above which acceptable electrode performance is attained. Our work suggests that this threshold is between 10^{-6} and 10^{-3} S m^{-1}.
- We found no clear correlation between GNP content and electrode mechanical properties. We also found no clear correlation between GNP content and capacity retention in long-term cycling tests.

- Silicon particle accessibility is strongly influenced by GNP content.
    - Increasing GNP content increases electrode thickness, which increases the ionic path length and tortuosity, resulting in increased overpotentials during lithiation.
    - Excessive increases in GNP content result in preferential stacking of the platelet-shaped conductive additive, which collapses porosity and severely limits silicon accessibility.
- Our XRD experiments revealed that silicon particle accessibility governs silicon amorphization and utilization in the electrodes.
    - Low GNP electrodes (high porosity, low thickness) exhibited the highest rates of silicon amorphization in our fixed capacity charging tests.
    - High GNP electrodes (low porosity, high thickness) exhibited the lowest rates of silicon amorphization.
- Increased GNP content also resulted in higher coulombic efficiencies, as the GNP network decreased the probability of disconnecting silicon particles during de-lithiation.
- Combined consideration of total gravimetric energy density, rate capability, cycling stability, and fast-charge overpotentials indicate that the ideal GNP content for this set of electrode materials is between 5 and 10 vol% GNP.

Our study has helped elucidate the effects of varying the conductive additive content in silicon microparticle electrodes. However, formulation development for commercial electrodes is often far more complex, involving many different particle morphologies, necessitating consideration of industrially relevant manufacturing processes, and requiring robustness against a wide range of operating conditions. The techniques and insights presented in this work can serve as a foundation to further develop our understanding of formulation effects on the performance of silicon electrodes.

Chapter 4 Magnetic Force Dilatometry of Silicon-NMC622 Lithium-Ion Coin Cells – the Effects of Binder, Capacity Ratio, and Electrolyte Selection

4.1 Introduction

Macroscopic expansion and contraction in lithium-ion battery electrodes is a function of the atomistic processes taking place during operation. Reversible volume changes correspond to reversible processes such as lattice expansion during lithium-ion intercalation or insertion[178,179], structural changes during reversible alloying/dealloying[174], and solid-electrolyte interphase (SEI) "breathing"[180,181]. Meanwhile, irreversible processes, such as amorphization of alloying anodes[173,174,182], SEI formation and growth[177,183–186], phase activation, degradation and defect evolution in layered metal oxide cathode materials[187–189], and trapped lithium in disconnected particles or "dead" lithium[174,177,190], contribute to irreversible electrode thickness changes. These microscopic volume changes become macroscopic in large format cells, as electrode layers are stacked together, and must be accounted for in cell, module, and pack designs[191]. Total cell expansion – the sum of both reversible and irreversible expansions from both anode and cathode – is a critical metric in applications with limited packaging space[7,192–195], and should be considered in the calculation of the true system volumetric energy density[196] (definitions in Appendix B). Accurate measurement of this expansion can provide key insights for electrode design, system design, and state-of-health sensing[197,198].

Adoption of silicon-based lithium-ion anodes could triple the volumetric energy density over incumbent graphite-anodes.[7] When paired with high voltage-capable cathode materials, recent cost analyses[9,10,199,200] project that battery costs could reach <\$125 kWh^{-1}. Nickel-rich layered cathode materials of $LiNi_xMn_yCo_zO_2$ (NMC, x + y + z = 10) can deliver relatively high gravimetric capacities at high voltages. In terms of expansion, these materials only exhibit very

minute material volume changes during delithiation/lithiation (~1-2%)[91]. However, the lithiation of silicon proceeds via alloying with a large, concomitant volume expansion[201]. Although lithiated silicon exhibits an appreciable degree of tensile plasticity[202], it undergoes brittle fracture at low strains (< 16%) regardless of the degree of lithiation[203]. Active material fracture disconnects it from the electrical network within the electrode and results in more surface area for SEI growth, both contributing to capacity fade and irreversible electrode expansion[127,204]. The expansion behavior of silicon lithiation is well-studied, and many active material-centric expansion-limiting strategies have been explored in literature: including hierarchical/nano-structuring[95,204,205], composite engineering[95], and liquid-metal encapsulation[206]. However, the influence of peripheral cell design parameters on cell expansion is less-thoroughly investigated. Examples of these parameters include electrode formulation, electrolyte selection, and capacity balancing.

Formulation can strongly influence the mechanical properties, morphology, and electrochemical performance of composite electrodes. As such, it is not surprising that electrode expansion is affected by electrode formulation. Particularly in silicon electrodes, binder chemistry has played a major role in enabling stable electrode performance. The binder has also been reported to influence cell expansion. Polyrotaxane-poly acrylic acid, a highly elastic, low modulus binder covalently bonded to the Si particle surface, resulted in less SEI growth and irreversible electrode expansion after 10 cycles when compared to an electrode using a more conventional polyacrylic acid as the binder.[207] On the other hand, Wang et al. and Yoon et al. reported that lower modulus binders resulted in larger irreversible thickness changes with cycling.[113,208] In addition, softer binders showed larger differences between fully lithiated and fully delithiated electrode thickness. Lack of covalent bonding between the soft binder and Si particles could explain the discrepancy between these studies and the relative irreversible expansions measured. Further, the conductive additive choice can also modulate electrode expansion. Karkar et al. reported dramatic differences in irreversible electrode expansion between electrodes with carbon black, vapor-grown carbon fiber, or graphite platelet fillers[146].

Park et al. demonstrated the use of hollow graphene to reversibly buffer electrode volume expansions.[209] Few electrode formulation studies report in-cycle volume changes[113], although we expect these also to be affected.

Electrolyte selection also plays a key role in silicon electrode performance and cell expansion. Poor electrolyte stability leads to greater SEI growth and irreversible expansion. Using in-situ AFM measurements of SEI thickness, Yoon et al. reported more SEI growth on silicon when propylene carbonate was used as the electrolyte solvent instead of ethylene carbonate (EC)[210], consistent with what has been observed in carbonaceous anodes[211,212]. Zhang et al. conducted a systematic study of numerous electrolyte solvent systems and reported that a fluoroethylene carbonate (FEC)/dimethyl carbonate (DMC) blend resulted in the most stable SEI layer and best cycling stability in silicon-graphite/NMC532 full cells.[213] Electrolyte additives are commonly used to increase SEI stability, as these components are preferentially reduced and generate stable SEI with desirable properties[211]. Fluoroethylene carbonate (FEC) and vinylene carbonate (VC) are among the most widely used electrolyte additives in silicon-containing cells[214–216]. Reduction of these components produce lithium carbonates, lithium alkyl carbonates, polycarbonates that are strongly adhered to the Si surface, and lithium fluoride[216–219]. Polycarbonate increases the SEI elasticity, making it more robust and resistant to fracture,[220] and likely also affects the electrode expansion/contraction behavior. However, both of these additives are continuously consumed during electrochemical cycling and are only capable of stabilizing cell performance for a limited time[221,222]. Lithium difluoro(oxalato)borate (LiDFOB) has also demonstrated good performance as an electrolyte salt or additive for NMC and silicon electrodes, forming a low-impedance, stable SEI layer[223–226]. Most studies on the effect of electrolyte selection on SEI growth and electrode expansion either utilize post-mortem analysis or measure nano-scale expansions on model electrodes[186,227]. We are unaware of any literature on operando cell expansion measurements focusing on the effects of electrolyte selection and SEI growth in conventional composite electrodes.

Changing lithiation cutoff potentials will influence the degree of lithiation, and thus expansion, in silicon electrodes. Wetjen et al. showed that wider potential windows resulted in larger irreversible thickness changes with cycling in silicon nanoparticle-graphite composite electrodes.[228] In full cells, changing the capacity ratio between anode and cathode directly influences the potentials experienced at each electrode.[229] This determines the degree of lithiation/delithiation at each electrode and should thus influence the cell expansion. Stressing the voltage conditions at each electrode by decreasing the negative-to-positive electrode capacity ratio (N/P ratio) will result in greater gravimetric lithiation/delithiation and exacerbate electrode degradation. In turn, we expect these conditions to increase both reversible and irreversible expansions in the cell.

In the literature, many methods have been used to measure electrode thickness changes with cycling. Post-mortem electrode thickness measurements using micrometers[113,230] or scanning electron microscopy (SEM)[228,231] are commonly used techniques. However, these measurements are inherently destructive, assume the electrode thickness is not altered by cell disassembly or any other post-mortem processes, and only provide thickness information at two points, i.e., the start- and end-of-test. Thickness changes in pouch cells have been monitored non-destructively using linear variable displacement transducers[232–234], pressure sensors[235], digital image correlation[236,237], and other light-based methods[238], yielding operando thickness monitoring. However, pouch cell construction can be resource intensive, limiting the accessibility of this technique. Another popular technique for operando single electrode thickness monitoring utilizes a rigid glass frit separator between the working and counter electrodes, allowing thickness changes of the electrode of interest to be monitored.[234,239–242] However, this technique is limited to low current testing, as the thick separator puts a large distance between the electrodes, resulting in large resistances when compared to coin cells and pouch cells.

Most battery work begins with small-scale testing, thus a low-cost, simple-to-use electrochemical dilatometer compatible with coin cells is highly attractive. In addition,

information on combined anode and cathode thickness changes is most relevant to practical cell design. To fill these needs, we have developed an operando magnetic dilatometry measurement system to monitor cell thickness changes within coin cells. We apply our technique to conduct operando cell thickness changes in Si/NMC622 2032 coin cells and investigate the influence of binder content, binder chemistry, capacity ratio, and electrolyte selection on cell expansion. To our knowledge, the effects of these parameters on cell expansion have not been explored with operando cell expansion monitoring. We aim to understand the significance of these parameters on cell expansion and ultimately, the true volumetric energy density of the cell.

We hypothesize that reversible expansions are correlated to reversible discharge capacity, while irreversible expansions are linked to irreversible lithium loss and capacity fade. We expect reversible expansions to be sensitive to the mechanical properties and morphology of the composite electrode. Possible root causes for irreversible expansions tied to capacity losses include SEI growth, trapped lithium in silicon, and lithium plating.

4.2 Methods

4.2.1 Electrode preparation and coin cell fabrication

Our NMC622 cathode and silicon anode electrodes with polyimide (PI) binder was prepared using the same method as described in our previous publication.[156] In this study, we used an 80/10/10 silicon/graphene nanoplatelet (GNP)/binder weight ratio as the baseline electrode formulation, called "1 x PI". A high binder content electrode with three times the theoretical binder layer thickness was tested for comparison. This electrode formulation was 66.7/8.5/25 and referred to as "3 x PI." Silicon electrodes with pyrolyzed polyacrylonitrile (PAN) binder were prepared in the same method as the air-dried electrodes described in another previous publication.[243] The formulation of these electrodes was 84.8/0.4/8.5/6.3 by weight of microparticle silicon/single-walled carbon nanotubes (SW-CNT)/carbon nano fiber

(CNF)/pyrolyzed polymer and are referred to as the "PAN" electrodes. For convenience, **Table 8** lists the electrode formulations used in this study.

Table 8: Electrode Formulations for Cell Expansion Study

Name	Silicon *(wt%)*	GNP *(wt%)*	SW-CNT *(wt%)*	CNF *(wt%)*	PI Binder *(wt%)*	Pyrolyzed PAN Binder *(wt%)*
1 x PI	80	10	0	0	10	0
3 x PI	66.7	8.5	0	0	25	0
PAN	84.8	0	0.4	8.5	0	6.3

Full cells were assembled using a 15.3 mm diameter anode, 12.7 mm cathode, Celgard 2325 separator, 40 µL of electrolyte, a 1.6 mm spring, and a 1.00 mm thick ferritic 430 steel spacer in a CR2032 coin cell. Use of a ferritic spacer enabled magnetic detection of cell thickness changes during cycling.

Three electrolytes were used in this study. The first was 1.2 M $LiPF_6$ in dimethyl carbonate:fluoroethylene carbonate (DMC:FEC) 4:1 with 2 wt% of vinylene carbonate (VC) and 3 wt% OS3 (Silatronix). The second electrolyte was 1 M $LiPF_6$ in ethylene carbonate:dimethyl carbonate (EC:DMC) 3:7 with 2 wt% FEC, 1 wt% VC, and 1 wt% LiDFOB. The third was 1 M $LiPF_6$ in EC:DMC 3:7 with 1 wt% LiDFOB. These electrolytes are referred to as "Y2", "B1," and "C1," respectively. The OS3 additive was obtained from Silatronix, LiDFOB salt was obtained from Sigma-Aldrich, and all other electrolyte components were obtained from Gotion. The electrolyte compositions are listed in **Table 9**.

Table 9: Electrolyte Compositions for Cell Expansion Study

Name	Electrolyte Composition
Y2	1.2 M LiPF6 in DMC:FEC 4:1 + 2 wt% VC + 3 wt% OS3
B1	1M $LiPF_6$ in EC:DMC 3:7 + 2 wt% FEC + 1wt% VC + 1wt% LiDFOB
C1	1M $LiPF_6$ in EC:DMC 3:7 + 1wt% LiDFOB

The cell configurations we built for this study are listed in **Table 10**. Two of each cell type were built and tested. Cathode active material loading was fixed at 4.5 mAh cm^{-2} and anode

loadings were adjusted to meet the N/P targets. Pristine electrode thicknesses were measured using a length gauge (Heidenhain MT 1281) affixed to a granite gauge stand (Heidenhain CS 200).

Table 10: Cell Configurations for Cell Expansion Study

Electrode	Electrolyte	N/P	Study Purpose
1 x PI	Y2	2.00 ± 0.05	Baseline
3 x PI	Y2	2.00 ± 0.05	Effect of binder content
1 x PI	Y2	1.50 ± 0.05	Effect of N/P ratio
PAN	Y2	1.5 ± 0.05	Effect of formulation
1 x PI	B1	2.00 ± 0.05	Effect of electrolyte
1 x PI	C1	2.00 ± 0.05	Effect of electrolyte

4.2.2 Electrochemical Test Procedures

Electrochemical tests were conducted using a battery cycler (Arbin, BT2043). The cells and dilatometers were kept in a thermal chamber (TestEquity TEC1 thermoelectric chamber) maintained at 25°C. Charge rates were calculated based on the cathode electrode capacity, measured at C/20 in a lithium half cell. The galvanostatic cycling protocol consisted of two formation cycles (CC charge at C/20, CV charge to C/50, CC discharge at C20), followed by cycling (CC charge at C/3, CV charge until C/20, CC discharge at C/3) between 3.0 and 4.2 V. A 15-minute rest period was employed after each charge and each discharge.

4.2.3 Magnetic Dilatometry

To monitor cell thickness changes during operation, coin cells were tested within our first-of-its-kind magnetic dilatometry test hardware, shown in **Figure 37**. A schematic of the hardware is shown in **Figure 38**. The hardware contains a slot for the coin cell, positive and negative electrode connections for the coin cell, and a spherical magnet affixed to a 2-pound load cell (Futek QSH02030), which are both on a micrometer-adjustable, lockable sliding stage. The load cell output is recorded using a digital load cell interface (Load Cell Central, model DSCUSB). A spherical magnet (K&J Magnetics, S7, $^{7}/_{16}$" dia.) was selected to reduce

experimental error from alignment issues, which we encountered when using flat, cylindrical magnets. The overall external size of the hardware is 8.5 x 10.5 x 5.5 cm.

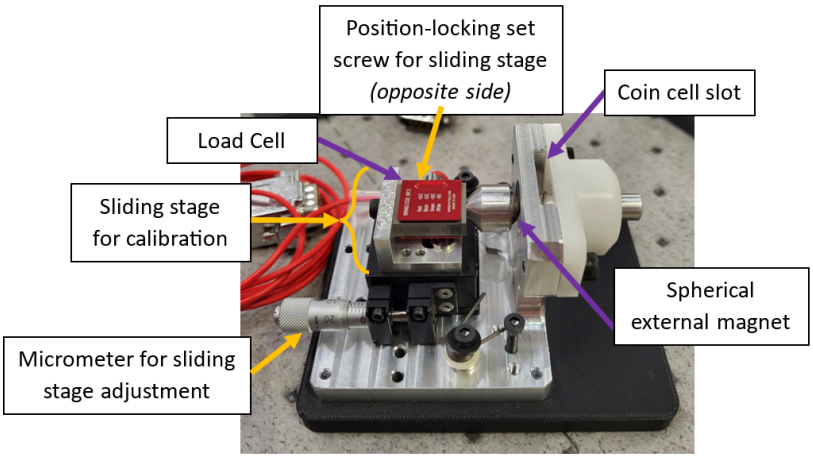

Figure 37. Photograph of magnetic dilatometer for coin cells. Photograph by W. Osad (GM R&D), May 3, 2023

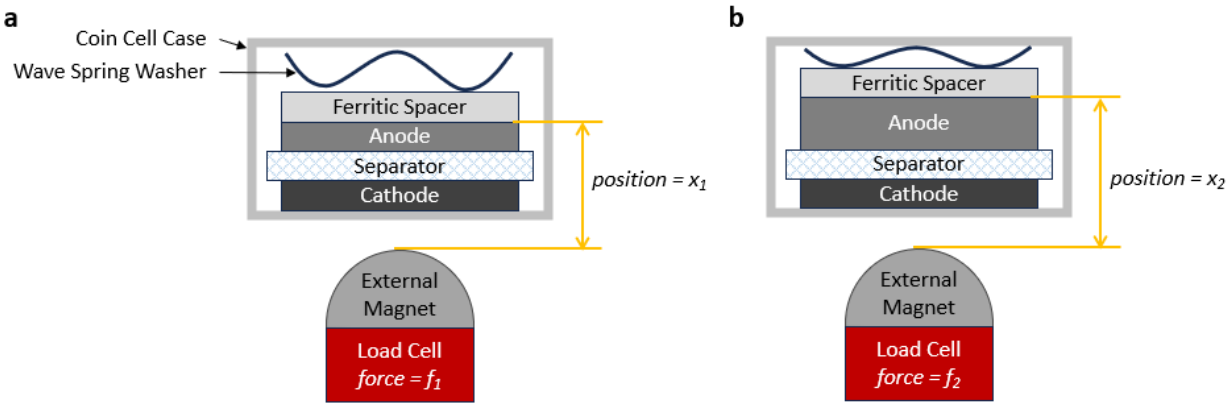

Figure 38. Schematic of magnetic dilatometry test hardware (a) before and (b) after cell expansion. Force is inversely related to the distance between the magnetic components; therefore, if $x_1 < x_2$, then $f_1 > f_2$.

The magnetic dilatometer consists of three key parts – the external spherical magnet, the load cell, and the coin cell slot. The spherical magnet is pressed and glued into a spherical cup, which is then carefully affixed onto the load cell. The load cell is mounted onto a small aluminum L-bracket, which is affixed to a micrometer-controlled slide rail, forming the slide-rail assembly. This assembly is bolted onto an aluminum base. A position-locking set-screw and two springs mounted to the aluminum base are used to control forward movement of the load cell

and spherical magnet. The position-locking set screw is used to hold the external magnet at a fixed position, not in contact with the coin cell during dilatometer and cell operation. The springs help to keep the load cell and magnet in position, preventing the magnetic attraction between the external magnet and the ferritic spacer from overcoming the locking set-screw and catapulting the external magnet towards the coin cell when the distance between the ferritic spacer and external magnet becomes small. The load cell electrical cable is affixed to the aluminum base with a small amount of slack to help isolate the load cell from any spurious load readings from movements of the cable.

The coin cell slot consists of a 3D printed nylon upper housing, a spring-loaded aluminum plunger for the positive electrical connection, and a machined aluminum lower housing, which serves as the negative electrical connection. The lower housing is machined into the aluminum base, which is then mounted onto a 3D printed plastic base.

The measurement principle is based on the force-distance relationship between the ferritic spacer and the external magnet. As the electrodes expand and contract during electrochemical cycling, the position of the ferritic spacer shifts within the coin cell, changing the distance between it and the external magnet, thus changing the force measured at the load cell affixed to the external magnet

Before beginning the electrochemical testing, we generated a force-distance calibration curve for each set of hardware. After the coin cell is affixed within its slot, we record the load as the external magnet is adjusted in 50 μm steps. This data is then fitted linearly to generate the calibration slope using a Python script. Immediately prior to testing, the external magnet is adjusted to be 100 μm away from the coin cell, then locked in position before electrochemical cycling.

Time synchronization of the electrochemical and load cell data streams was conducted using Python. Extraction of maximum cell height, minimum cell height, and cell height at the start of each cycle was also conducted using Python. Additional details are provided in Appendix

C. Further data analysis was performed using OriginLab software (Origin 2022, Northampton, MA).

We track two cell expansion metrics throughout the life of the cell: reversible and irreversible expansion. These metrics are illustrated in **Figure 39**.

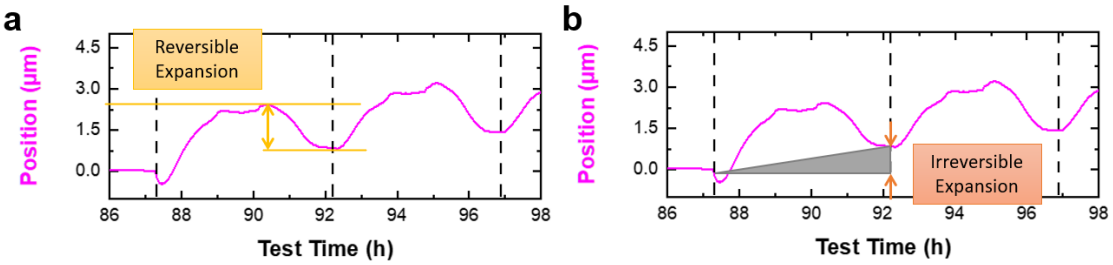

Figure 39. Illustration of reversible (a) and irreversible (b) expansion.

As we are primarily interested in cell thickness changes during cycling, both reversible and irreversible expansion are taken as a percentage of the cell thickness after formation, i.e., cell thickness at the start of the third cycle (first cycle after formation). The cell thickness after formation, $t_{3,o}$, was calculated by using the known initial cell thickness, t_0, and measuring the thickness change from start-of-test to the end of formation, Δx, using eq. 6. The cell thickness includes the anode and cathode electrode thicknesses. We exclude the separator and current collector thicknesses as we assume they do not change during cycling.

$$t_0 + \Delta x = t_{3,o}$$

eq. 6

We define percentage reversible expansion at the ith cycle as:

$$\%\ Reversible\ Expansion = \frac{x_{i,max} - x_{i+1,o}}{t_{3,o}} \times 100$$

eq. 7

, where $x_{i,max}$ is the maximum spacer position during the ith cycle, and $x_{i+1,o}$ is the spacer position at the start of the subsequent cycle.

We then define percentage irreversible expansion at the ith cycle as:

$$\%\ Irreversible\ Expansion = \frac{x_{i,o} - x_{3,o}}{t_{3,o}} \times 100$$

eq. 8

, where $x_{i,o}$ is the spacer position at the start of the ith cycle and $x_{3,o}$ is the spacer position at the start of the third cycle.

We hypothesize that irreversible expansion is correlated to capacity loss. Since cells of different configurations degrade at different rates, we compare % irreversible expansion against the cumulative irreversible capacity of each cell. We calculate the cumulative irreversible capacity over n cycles as

$$Q_{irr} = \sum_{3}^{n} (Q_{d,\,i-1} - Q_{d,i})$$

eq. 9

, where $Q_{d,i}$ is the cell discharge capacity at the ith cycle and $Q_{d,i-1}$ is the cell discharge capacity at the previous cycle.

4.3 Results

To check if the magnetic dilatometer had any influence on the cell cycling behavior, we ran preliminary tests where several of the cell configurations used in this study were built and cycled with commercially available 1.0 mm thick 316L stainless steel spacers. A comparison of the discharge capacities is shown in **Figure 40**. The discharge of the ferritic spacer cells was generally slightly lower than what was achieved with the austenitic spacers, but capacity fade trends are closely followed. All subsequent testing was conducted using ferritic spacers in the coin cells, run in the magnetic dilatometer.

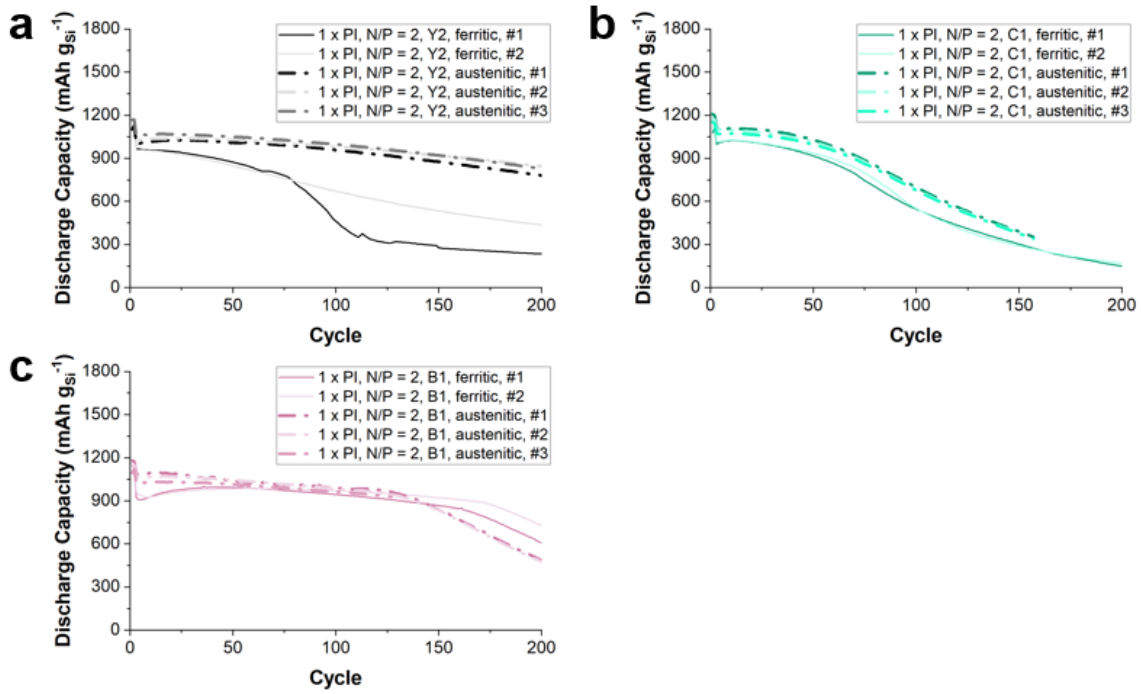

Figure 40. Comparison of coin cells with austenitic (conventional) and ferritic spacers. Coin cells were otherwise the same. Cells with Y2 electrolyte (a). Cells with C1 electrolyte (b). Cells with B1 electrolyte (c).

Plots of the measured cell expansion for the first 1200 hours of testing for each cell are provided in **Figure 41**.

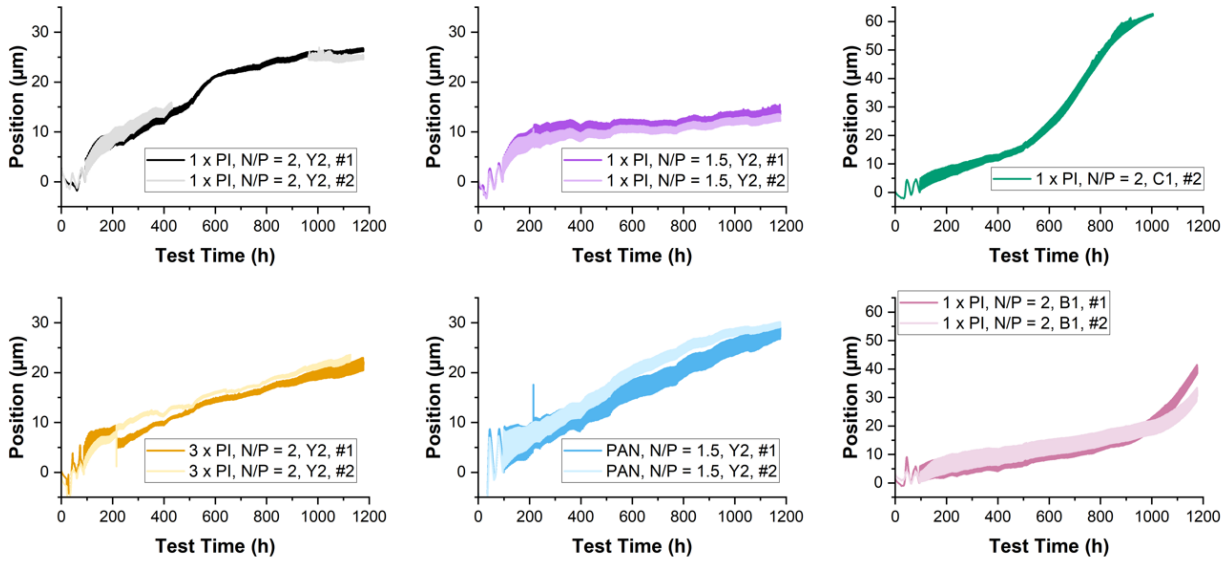

Figure 41. Position of the ferritic spacer vs. time. Positions are zeroed at the cell thickness at the start of C/3 cycling.

Examples of time-synchronized plots of the measured cell expansion (spacer position), capacity, voltage, and current for the first 150 hours of testing are provided in **Figure 42**.

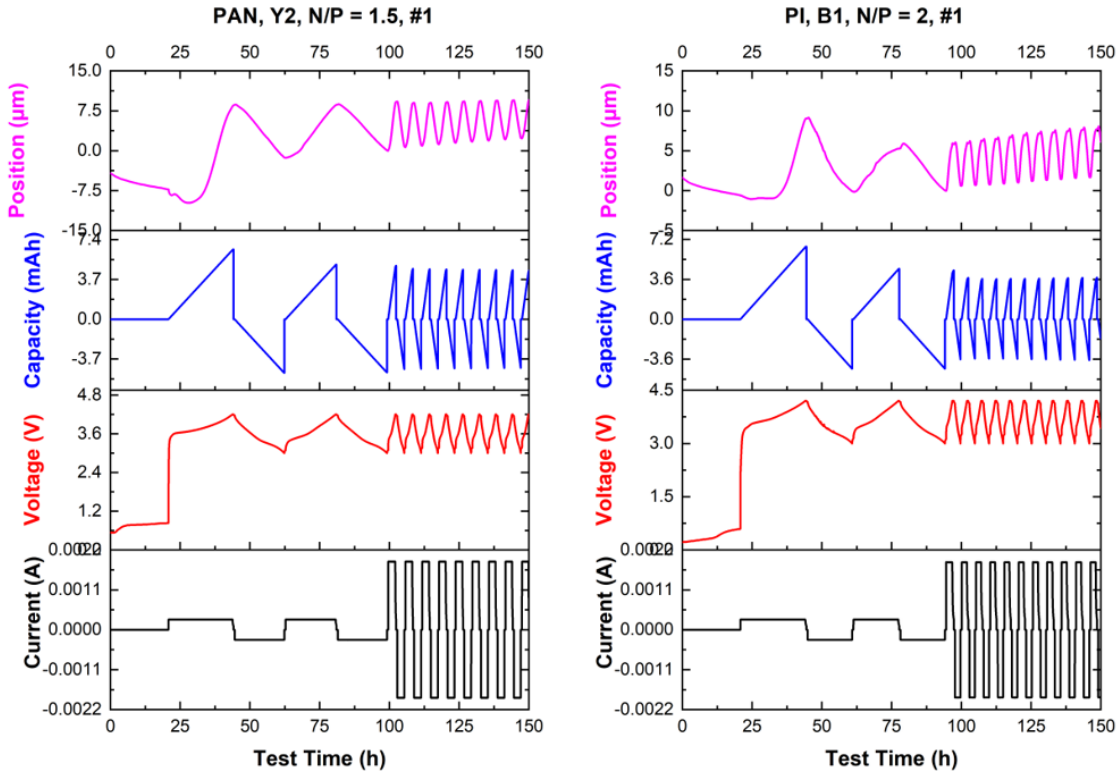

Figure 42. Stacked plots showing synchronization between cell cycling and cell expansion. Cell #1 of the PAN electrode cells (left) and cell #1 of the B1 electrolyte cells (right).

We observed several experimental artifacts and anomalies. The first 1 x PI cell with the ferritic spacer exhibited earlier capacity decay than in our preliminary tests using austenitic spacers (**Figure 40**a). Possible reasons for this behavior are electrolyte or electrode contamination, although we were not able to identify the root cause. We also observed experimental artifacts which affected the measurement of reversible expansion in the second 1 x PI, N/P = 2.0 cell from cycles 72 to 220 (**Figure 41**). We do not have a root cause, but we believe it to be an artifact because it had on/off characteristics. The measurement of irreversible expansion was not affected. But we have removed this section of reversible expansion data to make comparisons without the influence of the experimental artifacts. Additionally, we observed issues in the calibration of the 1st cell using C1 electrolyte, resulting in non-sensical cell expansion values, so that replicate is excluded from this analysis.

We additionally include a table of the pristine cell thicknesses and cell thicknesses after formation for comparison in **Table 11**. Most of the cells did not experience significant changes in cell thickness between those two points.

Table 11: Pristine cell thicknesses, to, cell thicknesses after formation, t3, and the difference in cell thickness between those points, Δt, for the cell configurations studied in this work.

Cell Configuration	Replicate	t_o (μm)	t_3 (μm)	Δt
1 x PI, N/P = 2, Y2	1	125.33	122.57	-2.76
	2	120	117.44	-2.56
3 x PI, N/P = 2, Y2	1	125.67	125.37	-0.30
	2	122.67	123.67	+1.00
1 x PI, N/P = 1.5, Y2	1	122.5	122.68	+0.18
	2	121	120.65	-0.35
PAN, N/P = 1.5, Y2	1	113.37	117.38	+4.01
	2	110.5	114.84	+4.34
1 x PI, N/P = 2, C1	1	124.67	---	---
	2	124.33	123.94	-0.39
1 x PI, N/P = 2, B1	1	124.67	125.03	+0.36
	2	125.5	122.10	-3.40

Cell thickness includes both the anode and cathode electrode thicknesses and excludes the current collector and separator thicknesses, as we assume they are invariant.

We confirmed that cell expansions are dominated by the anode electrode by comparing pristine electrode thicknesses with post-mortem electrode thicknesses of a subset of the cells, taken in the discharged state (**Table 12**). Cell expansions are dominated by the anode electrode, as the irreversible anode thickness changes far exceeded those of the cathode electrode. We expect this to be consistent across the different cell configurations that were tested in this study.

Table 12: Pristine electrode coating thicknesses, to, electrode coating thicknesses at end-of-test, tEOT, and the difference in electrode thickness between these points, Δt.

Cell	Electrode	t_o (μm)	t_{EOT}	Δt
1 x PI, N/P = 2, B1, #1	Anode	36.17	126	+89.83
	Cathode	90.5	98	+7.5
1 x PI, N/P = 2, B1, #2	Anode	35	109	+74
	Cathode	90.5	98	+7.5

End of test thicknesses were measured at low state-of-charge, using a micrometer after coin cell disassembly. Changes in cell thicknesses are slightly higher than what was measured in the magnetic dilatometer. These measurements were taken without significant force applied, unlike in the coin cell where the spring applies slight pressure to the electrodes.

Micrometers detect the largest thickness and are not suited to measuring average thickness across the electrode. In addition, the post-mortem measurements were conducted approximately one month after the end of test, leaving ample time for additional thickness increases from side reactions over time.

4.3.1 Binder Content vs. Cell Expansion

To study the impact of binder content in the electrode formulation on cell expansion, we compared measured expansions of the 1 x PI and 3 x PI electrodes. The discharge capacity of these electrodes during our cycle life test are shown in **Figure 43**a.

We hypothesize that reversible expansion is proportional to reversible capacity. The major source of cell expansion that is reversible is the reversible proportion of lithiation/delithiation, measured as discharge capacity. Although SEI breathing can also contribute to reversible expansion, the contribution is nearly negligible on a microscopic level[181]. Therefore, we plot the ratio between percentage reversible expansion and discharge capacity to discern the influence of binder content on this ratio in **Figure 43**b. The electrode with higher binder content exhibited less reversible expansion per discharge capacity, until the 100th cycle. Afterwards, the high binder electrodes exhibited more reversible expansion per discharge capacity.

Percent irreversible expansion is plotted as a function of cycles and the cumulative irreversible capacity in **Figure 43**c and **Figure 43**d, respectively. On average, the 3 x PI electrode showed less irreversible expansion than the 1 x PI electrode. The open symbols denote the 50th, 100th, 150th, 200th, and 250th cycles.

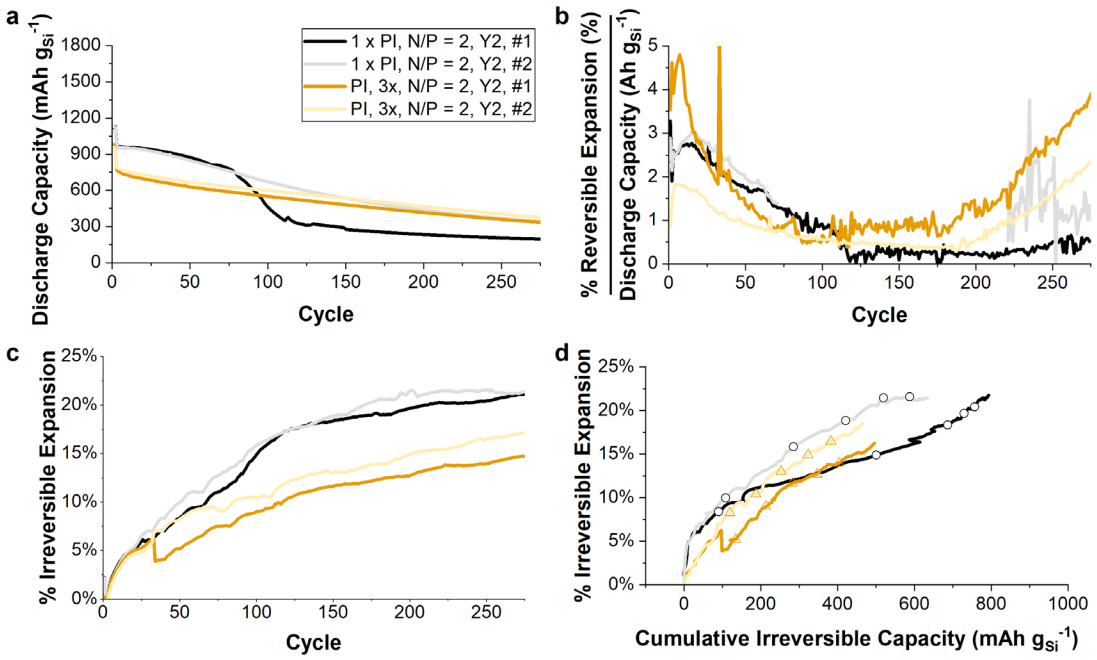

Figure 43. Discharge capacity (a), % reversible expansion scaled by discharge capacity (b), % irreversible expansion vs. cycle (c), and % irreversible expansion vs. cumulative irreversible capacity (d) for the 1 x PI and 3 x PI cells.

4.3.2 Capacity Ratio vs. Cell Expansion

To study the influence of N/P ratio on cell expansion, we compared cells made with the 1 x PI electrodes at N/P = 2.00 ± 0.05 and N/P = 1.50 ± 0.05, as shown in **Figure 44**. The 1 x PI, N/P = 2.00 cells are the same as those shown in **Figure 43**. We observed no influence from N/P ratio on the reversible expansion, as it is normalized by the discharge capacity. Unexpectedly, we observed that the cells with lower N/P showed less irreversible expansion than the cell with higher N/P.

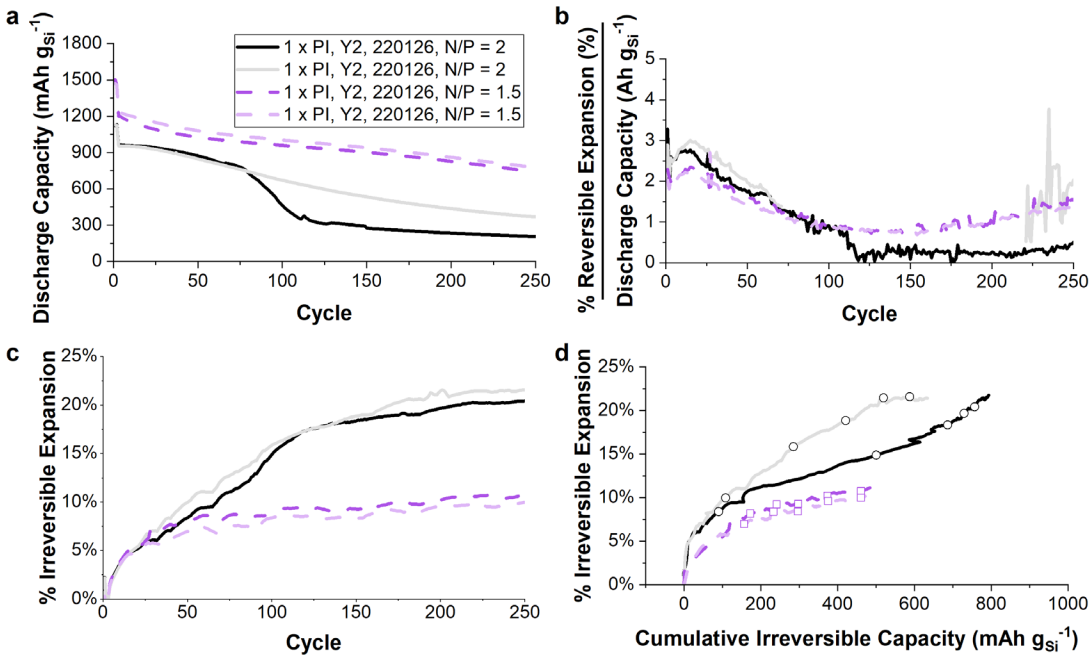

Figure 44. Discharge capacity (a), % reversible expansion scaled by discharge capacity (b), % irreversible expansion vs. cycle (c), and % irreversible expansion vs. cumulative irreversible capacity (d) for the 1 x PI cells at N/P = 2.00 and N/P = 1.50.

To help understand the differences in internal resistances in these cells, we monitored the voltage decay during the 15-minute open circuit rest after charging, as a proxy for cell resistance. The N/P = 2.00 cells showed greater voltage drop, thus cell resistance, than the N/P = 1.50 cells.

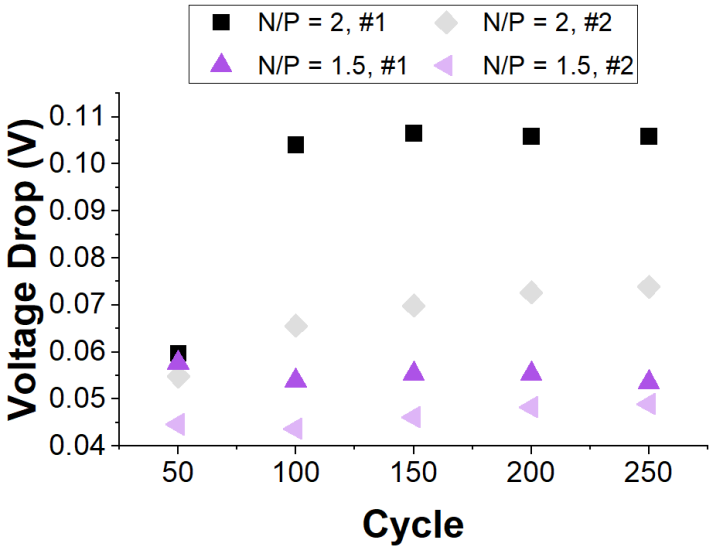

Figure 45. Voltage drop during the 15-minute OCV rest after charging and before discharging vs. cycle count for the 1 x PI electrodes with Y2 electrolyte at N/P = 2.00 and N/P = 1.50.

4.3.3 Binder Selection and Electrode Formulation vs. Cell Expansion

To study the influence of electrode formulation on cell expansion, we compared electrodes made with PI binder and electrodes made with pyrolyzed PAN binder. The discharge capacities, reversible expansions, and irreversible expansions are shown in **Figure 46**. The reversible expansion was higher in the PAN electrodes than in the 1 x PI electrodes. No significant differences in irreversible expansion were observed.

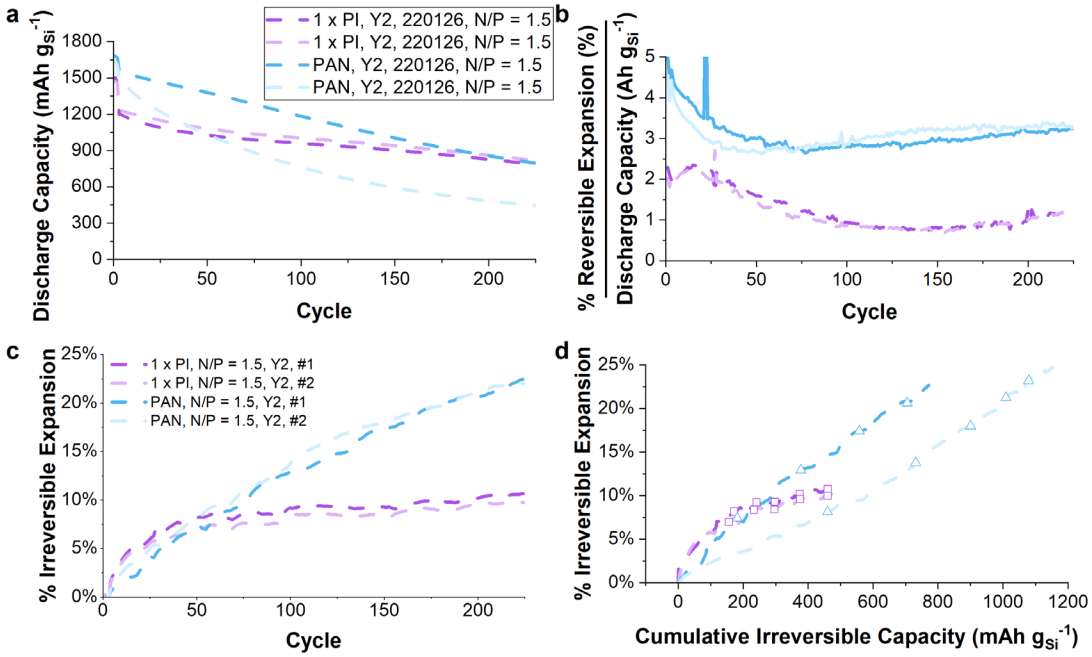

Figure 46. Discharge capacity (a), % reversible expansion scaled by discharge capacity (b), % irreversible expansion vs. cycle (c), and % irreversible expansion vs. cumulative irreversible capacity (d) for the 1 x PI and PAN cells at N/P = 1.5.

4.3.4 Electrolyte Selection vs. Cell Expansion

To study the influence of electrolyte selection on cell expansion, we compared the cell expansion observed in cells made with the 1 x PI electrode at N/P = 2.00 ± 0.05 using three different electrolytes, as shown in **Figure 47**. Again, the 1 x PI cells with Y2 electrolyte are the same as those shown in **Figure 43**. We observed differences in capacity fade behavior between the three electrolytes (**Figure 47**a). The reversible expansion to discharge capacity ratio also showed differences between electrolytes (**Figure 47**b). The Y2 cells exhibited continual decrease

in reversible expansion with cycling, while the reversible expansion in the B1 and C1 cells increased after the onset of capacity fade. A similar trend was observed in the percentage irreversible expansion; the irreversible expansion plateaued with cycling while it increased in the B1 and C1 cells after the onset of capacity fade (**Figure 47**c). When percentage irreversible expansion is plotted against cumulative irreversible capacity, we observe that the three electrolytes result in different rates of irreversible expansion (**Figure 47**d).

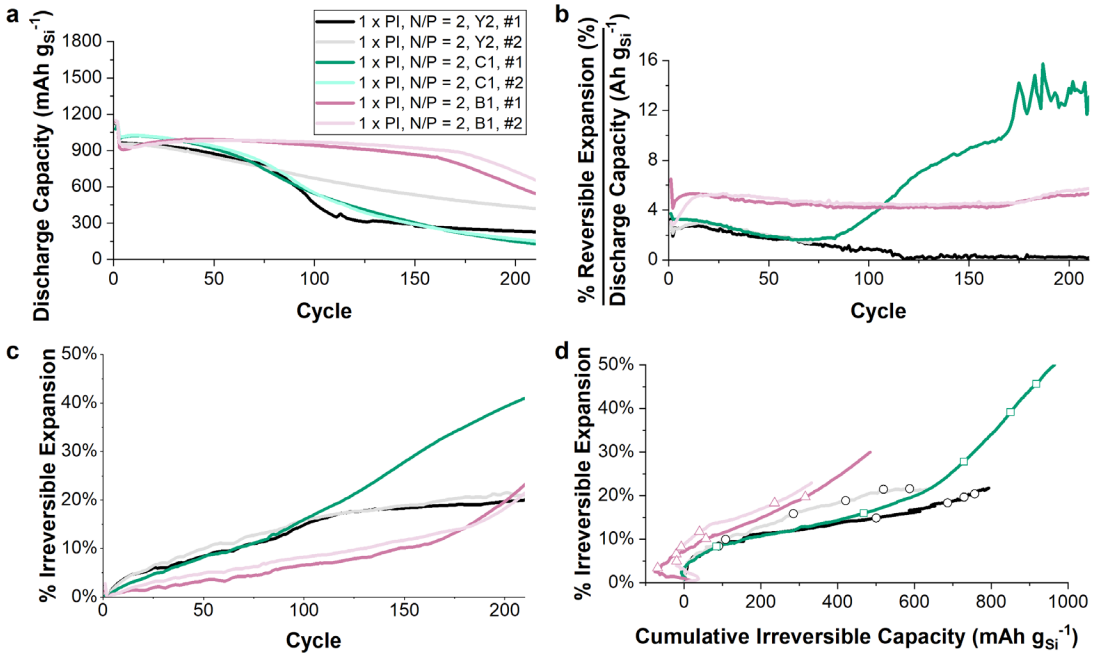

Figure 47. Discharge capacity (a), % reversible expansion scaled by discharge capacity (b), % irreversible expansion vs. cycle (c), and % irreversible expansion vs. cumulative irreversible capacity (d) for the 1 x PI cells with Y2, C1, and B1 electrolytes.

For the reader's convenience, we have additionally included plots of the reversible and irreversible expansions in microns vs. cycle number in **Figure 48** and **Figure 49**, respectively.

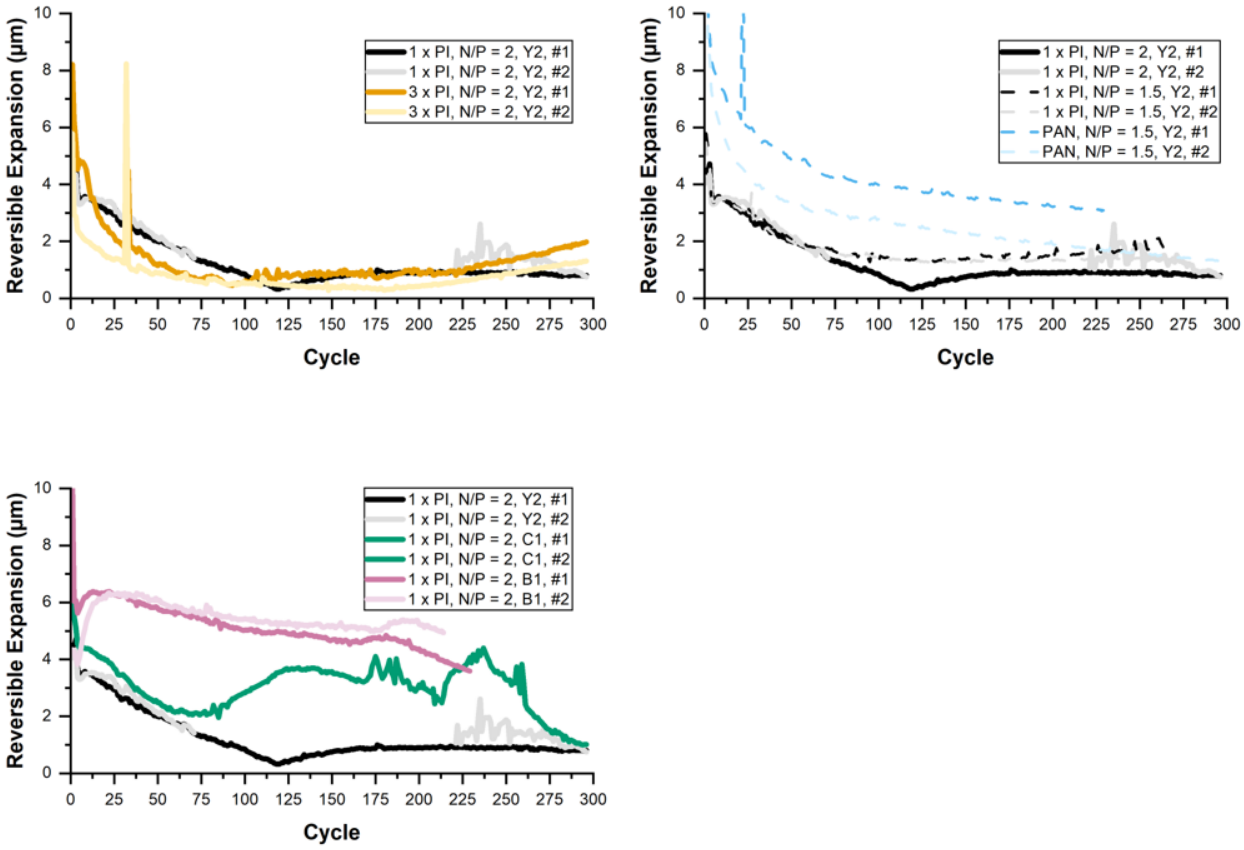

Figure 48. Reversible expansion, in microns, vs. cycle.

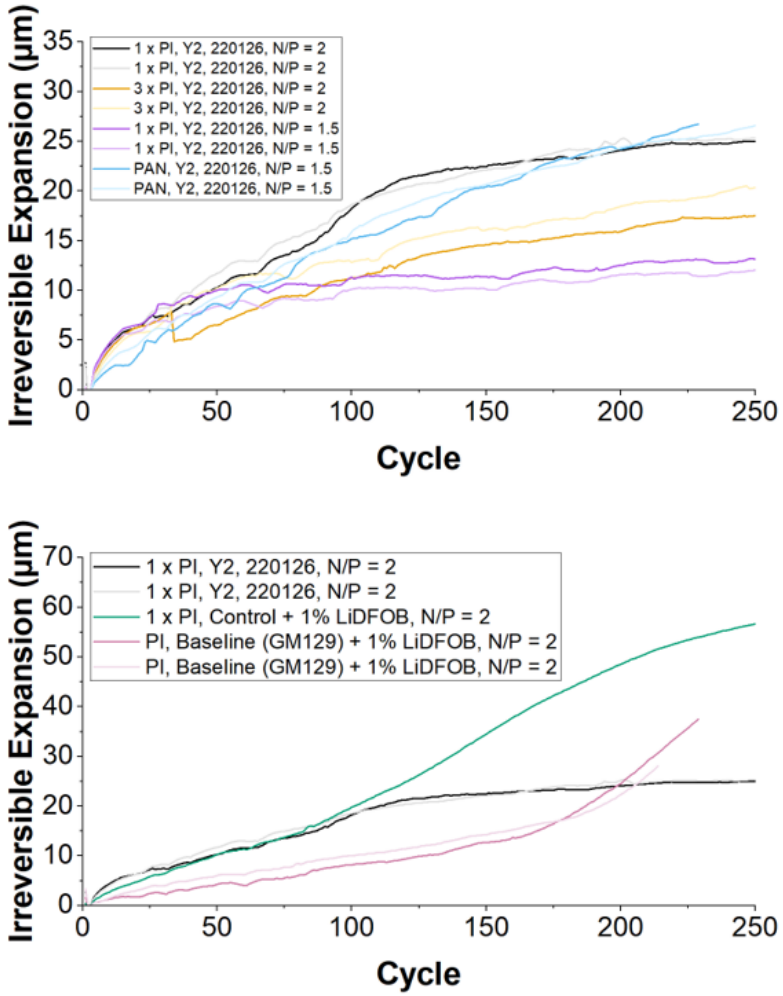

Figure 49. Irreversible expansion, in microns, vs. cycle.

4.4 Discussion

During the 12-hour rest that was employed between cell build and the start of formation, the electrodes tended to compress further (**Figure 41** and **Figure 42**). Electrolytes will typically swell binder materials, resulting in plasticization of the binder and a reduced modulus[244]. A reduction in binder modulus softens the composite electrode, resulting in the observed compression as the electrolyte soaks into the electrodes.

Subsequently during formation, the overall cell thickness increases with cycling due to irreversible processes, including Si amorphization, Si lithiation, and SEI growth. Interestingly, the initial cell thickness and cell thickness after formation are similar (**Table 11**). Overall we

observed the cell thickness increase during charging and decrease during discharging (**Figure 42**), as the Si volume changes dominate (~300% in Si[201] vs. ~1-2% in NMC622[91]). The volume change behavior during formation was less consistent than during cycling. This could be attributed to phenomena that are unique to the formation process, such as the crystalline-to-amorphous transition in the Si, initial SEI formation, and electrode cracking[114].

4.4.1 Influence of Binder Content on Cell Expansion

Electrode binder content has a measurable effect on cell expansion. In earlier cycles, the 3 x PI electrodes exhibit less reversible expansion, when scaled by discharge capacity (**Figure 43**b). One reason is that higher binder content increases the compliance of the electrode, especially as the electrolyte swells and plasticizes the binder. As such, the electrode is more able to buffer volume expansions of the electrode particles. A second explanation is that the high binder content reduces the electrode porosity and limits silicon particle accessibility in early cycles[156]. With less amorphization of the available silicon, we expect less volume change.

This trend reverses in later cycles. After around 100 cycles, the 3 x PI electrodes exhibit more reversible expansion per discharge capacity than the 1 x PI electrodes. Our previous work found that silicon utilization with cycling is influenced by binder content.[156] Namely, silicon utilization in the 3 x PI electrodes increases by 200% after 50 cycles at C/5, compared to only 75% the 1 x PI electrodes. We believe this explains the current observation – that reversible expansion in the high binder electrodes increases in later cycles as the silicon utilization also increases.

With regards to irreversible expansion, the 3 x PI electrodes exhibited less capacity loss, leading to less irreversible expansion with cycling than the 1 x PI electrodes (**Figure 43**a and **Figure 43**c), consistent with our hypothesis. When plotted as a function of cumulative irreversible capacity **Figure 43**d), the 3 x PI electrodes show less irreversible expansion for the same level of capacity fade, especially at lower levels of capacity fade. We believe this is again tied to the expansion-buffering effect of the binder.

4.4.2 Influence of Capacity Ratio on Cell Expansion

Decreasing the N/P ratio pushes the silicon to a higher gravimetric capacity (**Figure 44**a). We observe that N/P ratio has no influence on reversible expansion, when scaled by discharge capacity (**Figure 44**b). This is completely in agreement with our hypothesis – that when the electrode formulation and electrolyte composition are held constant, the reversible expansion is simply a function of the reversible discharge capacity. We regard the N/P = 2.00, cell #1 as an outlier, as it exhibited an unexpectedly early onset of capacity fade. With the capacity fade, the reversible expansion in this cell decayed significantly, implying the presence of a different degradation mechanism.

Surprisingly, we observed lower irreversible expansion in the cells with lower N/P ratio (**Figure 44**c). Originally, we expected that increased silicon lithiation in the low N/P cell would result in more Si particle cracking and SEI growth, leading to more irreversible expansion. However, this is not what we observed. An alternative explanation is tied to reduced anode electrode resistances in the low N/P cells. To achieve the lower N/P with a fixed cathode loading, the anode loading was reduced. Concomitantly, the electrode thickness is reduced, resulting in an electrode with lower resistance. Lower resistance would reduce instances of trapped lithium and lithium plating, and thereby reducing the irreversible expansion. Indeed, when we compare the voltage decay during the 15-minute open circuit rest after charging as a proxy for cell resistance, there is less voltage decay, thus less resistance in the lower N/P cells (**Figure 45**).

4.4.3 Influence of Binder Chemistry and Electrode Formulation on Cell Expansion

In our comparison between the PI and PAN electrodes, the PAN electrodes exhibited far greater reversible expansion than the PI binder electrodes (**Figure 46**b). Both electrodes started with initial total porosities of 50-55%[156,243], however the binder in the PAN electrodes have been carbonized via pyrolysis. This results in a significantly stiffer binder and electrode. Although silicon particles in conventional electrodes can readily expand into the pores throughout the

electrode, we believe that the lack of flexibility in the PAN electrodes cannot accommodate this movement and favors overall electrode expansion over pore-filling.

As for irreversible expansion, the PAN electrodes exhibited significantly more irreversible expansion with cycling (**Figure 46**c). But when scaled by capacity loss, the rate of irreversible expansion was very similar to that in the PI electrodes (**Figure 46**d). Although the binder chemistry did not affect the capacity loss-scaled irreversible expansion in this case, this may not be the case with other binder chemistries. In cases where binder chemistry directly affects SEI growth rates, we expect to see differences in irreversible expansion with binder chemistry, as reported in other literature[113,207].

4.4.4 Influence of Electrolyte Selection

The onset and nature of capacity decay reveal characteristics and efficacy of the additive packages and solvent systems utilized in the electrolytes tested. For electrolyte selection, there are two contributing factors to capacity decay: the solvent stability and additive consumption. FEC, VC, and LiDFOB are all consumable electrolyte additives. When the additives are fully consumed, there is a notable downward inflection point in the capacity curves[221]. On the other hand, switching electrolyte solvent systems tend to produce different capacity decay slopes due to the varying solvent stabilities[213]. The C1 cells had the lowest additive content, therefore it exhibited the characteristic downward inflection point in the fewest cycles (around 75 cycles; **Figure 47**a). Meanwhile, the B1 electrolyte, which contained a combination of FEC, VC and LiDFOB, was more effective at maintaining the cell discharge capacity up to 175 cycles, after which the capacity decays notably. The Y2 contains DMC and FEC as co-solvents, which has been reported to be a more stable solvent system than EC/DMC[213]. In addition, the additive content in Y2 is the highest among the electrolytes tested. As such, cells with the Y2 electrolyte did not typically contain the downward inflection point, apart from our first cell, which failed uncharacteristically early. Overall, the B1 cells exhibited the best capacity retention, indicating that the FEC/VC/LiDFOB additive package, though sparingly used, was an effective electrolyte

additive package for our Si/NMC622 cells. Further improvements would include finding ways to prolong the effectiveness of this additive package.

Reversible cell expansions show different behavior for each electrolyte. In the B1 and C1 cells, we observe coincident increases in reversible expansion with the downward inflection point in the capacity curves (**Figure 47**b). We do not believe this is tied to evolving composite electrode stiffness with cycling. Wang et al reported that composite electrode moduli decrease with cycling, as the SEI builds up, Li is increasingly trapped in the Si, and mechanical integrity declines[245]. This should result in a decrease in reversible expansions, yet we observed the opposite. Instead, we attribute the shift in reversible expansion behavior to shifts in silicon utilization with electrode degradation. Michan et al. proposed that as SEI growth clogs electrode pores, silicon particle accessibility declines, especially near the current collector.[127] As a result, accessible Si particles near the electrode surface become more deeply lithiated. When this occurs, the electrode porosity is no longer able to accommodate Si volume changes, forcing the electrode thickness to increase. Interestingly, the Y2 cells show a continual decrease in reversible expansion with cycling (**Figure 47**b). We attribute this to the differences in electrolyte composition, but further work would be required to fully understand this observation.

Irreversible expansions also showed a distinct trend with discharge capacity (**Figure 47**c). For the B1 and C1 electrolytes, upticks in irreversible expansion occurred with downturns in discharge capacity. This is in line with SEI-related cell degradation mechanisms that have been elucidated in literature[113,127,246]. The increase in SEI growth clogs electrode pores and increases cell resistance, leading to trapped lithium and capacity loss. As SEI growth and trapped lithium increase, their effects are measurable in irreversible cell expansions. The pattern of irreversible expansion plotted against cumulative discharge capacity also reflects the cell degradation behavior with each electrolyte system (**Figure 47**d). Again, the B1 and C1 electrolytes exhibit a step-change in the rate of irreversible expansion vs. cumulative irreversible capacity loss,

corresponding to the downward inflection point in the capacity curves, indicating a change in SEI growth mechanism.

4.4.5 Influence of Cell Expansion on Volumetric Energy Density

To understand the impact of cell expansion on volumetric energy density, we used the measured cell expansions for the 3rd cycle, then every 50 cycles thereafter. Included in the cell volume were a 22 µm thick aluminum current collector, 10 µm thick copper current collector, 25 µm thick separator, and the expanded electrode thicknesses at that cycle. We excluded the coin cell hardware volume, as it is less of a factor in large format, commercial battery cells. We also did not include excess electrolyte volume, as further studies would be needed to determine the optimal quantity of electrolyte.

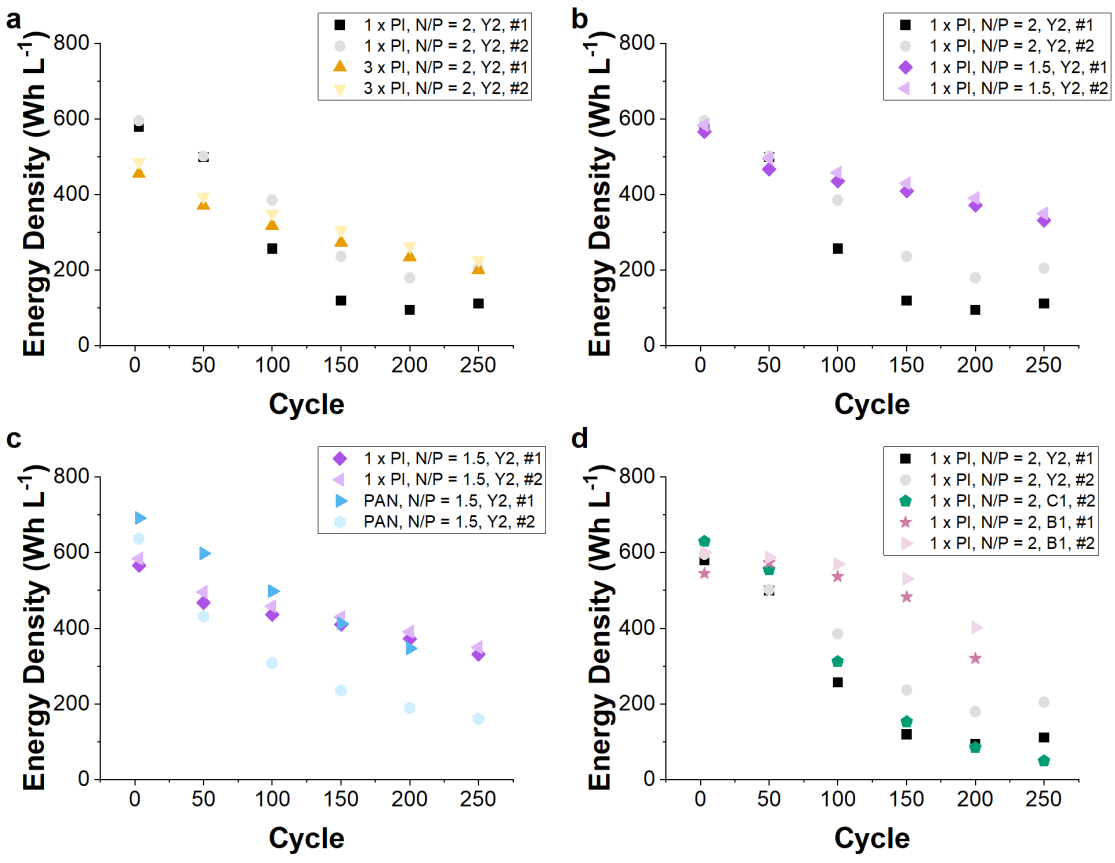

Figure 50. Volumetric energy density vs. cycle for cell configurations tested in this study.

Our calculations show that the volumetric energy density significantly decays with cycling, mainly due to irreversible expansions. Interestingly, the volumetric energy density of the 3 x PI cells becomes higher than that of the 1 x PI cells around cycle 150. The cell configurations with the best energy density retention at 200 cycles are 1 x PI, N/P = 2.00, B1 cells and the 1 x PI, N/P = 1.50, Y2 cells, both decaying by only ~30%. Additionally, using a lower capacity balance improved capacity retention and reduced irreversible cell expansions, yielding a lower ideal N/P ratio. Meanwhile, the C1 and Y2 electrolytes exhibited the poorest energy density decay, dropping by ~80% from 3 to 200 cycles. This highlights that judicious selection of peripheral cell parameters can have a major impact on volumetric energy density over the life of the battery.

4.5 Conclusions

Magnetic dilatometry is a low-cost, facile method for conducting operando cell thickness measurements in coin cells. Prior to our work, these measurements were limited to post-mortem, usage of thick glass-frit separators, or large format cells, all less accessible than the present technique. Magnetic dilatometry is enabled by the usage of a ferritic stainless-steel spacer and the measurement of the load detected at a spherical magnet held at a fixed position external to the coin cell. Electrode expansions and contractions shift the position of the ferritic spacer relative to the stationary, external magnet, changing the detected load. A force-position calibration curve is utilized to convert the detected measured load into a cell expansion.

We utilized this technique to conduct operando cell thickness measurements in Si/NMC622 coin cells, where cell expansions were dominated by the silicon anode volume changes. We studied the influence of electrode binder content, electrode formulation, N/P ratio, and electrolyte selection on cell expansion, tracking both reversible and irreversible expansion in the cell. Ultimately, these measurements shed light on how volumetric energy density evolves with cycling—an important metric for automotive battery design.

- Cell expansions in Si/NMC622 cells are dominated by the silicon anode behavior.
- Irreversible cell expansions correlate with irreversible capacity losses.

- Increasing the electrode binder content results in reduced initial capacity but cycling stability and energy density are maintained with cycling.
    - 3 x PI exhibited a 55% reductio in volumetric energy density after 250 cycles, while 1 x PI exhibited 75%.
- Decreasing N/P ratio resulted in lower electrode resistances, higher cycling stability, and better maintenance of volumetric energy density.
    - Cells with N/P = 1.50 exhibited only a 30 % reduction in volumetric energy density after 250 cycles, while cells with N/P = 2.00 exhibited a 75% reduction.
- Pyrolyzing the binder increases cell expansion.
    - Silicon electrodes with polyimide binder cells exhibited a 30 % reduction in energy density at 200 cycles, while electrodes PAN binder exhibited a 50% reduction.
- Electrolyte choice has a significant impact on cell expansion with cycling
    - Cells with the B1, Y2, C1 electrolytes exhibited 10%, 60%, and 70% reduction in energy density at 150 cycles, respectively.

When reversible expansions were scaled by cell discharge capacity, we observe that they are most sensitive to the mechanical properties of the composite electrode. When the electrode formulation remains the same, reversible expansions scale with discharge capacity, as in our cells with varying N/P ratios. Increasing electrode stiffness, by decreasing binder content or by pyrolyzing the binder, increased reversible cell expansions, as the electrode is less able to buffer any expansions. However, when testing different electrolytes, increases in the reversible expansion-to-discharge capacity ratio were not a result of shifting electrode modulus. Instead, we believe they were the result of a shift in silicon utilization stemming from extensive SEI growth.

Irreversible expansions were a symptom of cell degradation mechanisms. Most notably, the influence of electrolyte selection had the strongest impact on irreversible expansions.

Increases in irreversible expansion growth rates coincided with cell capacity decay rates. Usage of a ternary blend of electrolyte additives (LiDFOB, VC, and FEC) suppressed irreversible expansion by up to two thirds compared to usage of a LiDFOB alone or by up to one half when using binary additive package containing just FEC and VC.

Further work to elucidate root causes of the observed expansion behavior is warranted. This could include tracking electrode morphology and mechanical properties with cycling, tracking electrolyte composition with cycling, and tracking SEI composition with cycling to corroborate the present measurements.

Additionally, as most battery development begins at the coin cell level, magnetic dilatometry allows researchers to understand cell expansion behavior at an earlier stage of research. We believe this technique presents a great opportunity for further exploration, as a vast parameter space and its influence on cell expansion can now be explored using the coin cell platform.

Chapter 5 Conclusions and Future Work

5.1 Summary

We examine the structure-properties-performance relationships in silicon microparticle electrodes for lithium-ion batteries, exploring the influence of formulation and cell parameters, i.e., electrolyte selection and capacity ratio. We track how electrode formulation affects electrode porosity, mechanical properties, and electrical conductivity, and identify correlations between these characteristics and electrochemical performance. The various cell configurations are evaluated using three critical performance metrics: fast-charge capability, gravimetric energy density, and volumetric energy density. Full cells with high capacity loadings (4.5 mAh cm^{-2} at beginning of life) were used throughout our study to maintain relevance to near-term commercialization targets.

Binder content can significantly impact electrode performance, lithiation/delithiation kinetics, and degradation mechanisms. Increasing binder content decreases electrode porosity and electrical conductivity but improves cohesion between electrode particles and adhesion to the current collector. Decreasing electrode porosity and electrical conductivity reduce silicon particle accessibility to lithium ions and electrons. This affects lithiation/de-lithiation kinetics and increases electrode overpotentials during charging and discharging and reduces electrode capacity at high charge rates. On the other hand, increasing binder content will improve electrode mechanical integrity and improve capacity retention during long-term cycling. Therefore, optimizing the binder content in electrode formulations involves a trade-off.

When capacity retention is the main objective, increased binder content is advantageous. But to also achieve improvements in fast-charge performance, a balance between particle accessibility and mechanical robustness is needed.

Additionally, using XRD to monitor silicon amorphization with cycling, our work revealed that binder content can influence electrode degradation. In electrodes with optimal binder content, the rate of silicon amorphization, thus utilization, is more stable than in electrodes with excess or insufficient binder content.

Conductive additive content also impacts electrode performance. Increasing the conductive additive content increases the electrical conductivity of the electrode. However, we found that there is a minimum threshold of conductivity required for adequate electrode performance – above this threshold, there were no appreciable performance benefits. Interestingly, no clear correlation was found between conductive additive content and electrode mechanical properties. No correlation was observed between GNP content and capacity retention during long-term cycling.

The conductive additive content most strongly affects electrode morphology and lithiation/delithiation dynamics. Increasing the conductive additive content, an inactive component, necessitates an increase in electrode thickness to maintain the same active material areal loading. This increases the lithium-ion diffusion path length, decreasing silicon particle accessibility and increasing lithiation overpotentials. With excessive conductive additive content, the electrode porosity will collapse, due to preferential stacking of the plate-like conductive additive used in our study, further limiting silicon particle accessibility.

Fixed capacity lithiation experiments, combined with post-mortem XRD revealed that silicon strongly depends on particle accessibility. Electrodes with low GNP content (high porosity and low thickness) exhibited the highest rates of silicon amorphization, while electrodes with high GNP content (low porosity and high thickness) exhibited the lowest rates of silicon amorphization.

Examination of coulombic efficiencies reveals that increasing the conductive additive content helps to maintain connectivity of silicon particles during delithiation. Generally, coulombic efficiencies increased with conductive additive content. However, excessive

conductive additive content resulted in very poor coulombic efficiencies, due to low electrode porosity and poor particle accessibility.

We compare the gravimetric energy densities and fast charge capability of the various electrode formulations tested in this work as a function of formulation and cycle number. For the electrodes tested in the first parts of this thesis, we find that an electrode formulation with between 5 and 10 vol% GNP and 6 nm binder layer thickness would give the best combination of fast-charge capacity and gravimetric energy density, on a total electrode mass basis, at both beginning and end-of-life.

In the last chapter of this dissertation, we used operando magnetic dilatometry on coin cells to explore the effects of electrode formulation, capacity ratio, and electrolyte selection on cell expansion. We monitored both reversible and irreversible cell expansions. Reversible expansions are a function of reversible electrode capacity and stiffness, while irreversible expansions were a symptom of cell degradation mechanisms.

Our measurements revealed how cell parameter selection influences the volumetric energy density retention with cycling, with capacity ratio and electrolyte selection exhibiting the strongest effect. Of the cell configurations studied in this dissertation, the 1 x PI electrodes at N/P = 1.50 and the Y2 electrolyte exhibited the most stable and highest volumetric energy density. We believe additional improvements can be achieved by further refining electrolyte compositions, as the B2 electrolyte was able to limit irreversible cell expansion and maintain high volumetric energy density through the 150^{th} cycle.

Overall, the insights gained in this thesis contribute to the development of silicon microparticle composite electrodes for lithium-ion batteries. Our systematic investigation of the effects binder and conductive additive content indicated a strong interdependence between electrode formulation, structure, properties, and performance. In addition, our operando magnetic dilatometry experiments revealed that cell parameters, including electrode formulation, capacity ratio, and electrolyte selection, played a significant role in controlling reversible and irreversible cell expansions with cycling. The insights gained through the course of this work can

inform continued electrode and cell optimizations, guide definition of product specifications for commercialization, and serve as a catalyst for future research and development of silicon anode electrodes for lithium-ion batteries.

5.2 Future Work

5.2.1 Measuring Lithium-Ion Diffusion through Polymeric Binders

One subject that was left untouched in this thesis is the diffusion of lithium-ions through polymeric binders. Many measurements of lithium-ion diffusion coefficient measurements have been made for various anode active materials, e.g., silicon[17,167,168,247], graphite[248], lithium titanium oxide[249], nickel manganese cobalt oxide[250,251], lithium cobalt oxide[252], and lithium ion phosphate[253,254], and for solid electrolyte interphases[255,256]. Comparatively few measurements of lithium-ion diffusion through the binder layer have been published, despite the vast diversity of polymeric binder materials[63]. Obtaining these measurements could be highly valuable for computational simulations and to measure the efficacy of binder design and processing towards improving lithium-ion diffusion. To this end, we made some experimental efforts, which are detailed in Appendix E. But due to unsolved experimental difficulties, this project was not completed.

5.2.2 Understanding Degradation Mechanisms

Continued effort to understand the interaction between electrode formulation, manufacturing variations, and electrode degradation mechanisms are critical to producing high quality batteries with exceptional durability and reliability. The elucidation of degradation mechanisms is extremely time and resource intensive, yet invaluable. Piecing together a more complete understanding of this topic can unlock innovations in degradation avoidance or mitigation strategies and drive the advancement of battery technology.

Specifically, additional post-mortem analysis on the formulations tested in this dissertation could be illuminating.

- Combined usage of electron backscatter diffraction (EBSD) and energy dispersive spectroscopy (EDS) maps can identify regions of silicon amorphization within silicon electrode cross-sections. These techniques have the potential to reveal the morphology of silicon amorphization within electrodes and how it evolves with cycling. The effects of many parameters, such as electrode formulations, manufacturing procedures, and cycling conditions, on silicon utilization can be explored. In addition, serial sectioning, combined with EBSD/EDS within the same electrode can reveal the effects of manufacturing variations in electrode utilization.
- Development of spatially-resolved characterization techniques that are sensitive to light-elements can also help to develop a more complete understanding of the effects of electrode formulation and other cell parameters on degradation mechanisms. In particular, correlative Raman-SEM imaging, which can provide up to 360 nm lateral resolution and 1.5 μm depth resolution shows incredible promise to this end[257]. Raman spectroscopy is sensitive to changes in molecular vibrations. It is capable of detecting changes in binder and SEI chemistry and strains in lithiated silicon[258]. In addition, Raman spectroscopy could potentially also detect changes in lithiation in silicon-derivative active materials, such as amorphous silicon, silicon oxide, lithiated silicon oxides, and carbon/silicon composite materials, which can also be immensely beneficial to the research community, as these materials have garnered strong interest in recent years.

5.2.3 Understanding Cell Expansion

The database of cell expansion data in published literature is sparse, as previous methods of measuring cell expansion were cumbersome and resource intensive. The technique of magnetic dilatometry in coin cells, as demonstrated in this work, significantly reduces that barrier, so that the influence of an infinite number of cell parameter combinations on cell expansion can be measured.

- Coupling cell expansion tests with post-mortem analysis to deepen understanding of cell degradation mechanisms at play would be another valuable direction of future work. Again, informing our understanding of electrode degradation mechanisms is invaluable to battery development work.

5.2.4 Emphasizing Development of High-Throughput Characterization Techniques

The focus of this dissertation was to elucidate the relationship between electrode formulation and performance, with the thought that these learnings could inform not only electrode design and specifications, but also quality inspection standards. To apply these learnings to a high-volume manufacturing setting, an emphasis on developing high-throughput characterization techniques can also be of great value to battery manufacturers. For light duty, all-electric vehicles, a battery size of 100 kWh is typical. Assuming the following parameters from the cells tested in this work (4.5 mAh cm^{-2}, 80% ICE, 3.6 V average voltage), approximately 750 m^2 of anode and 750 m^2 of cathode coating would be required per vehicle. This necessitates very high manufacturing speeds and a high volume of quality inspections. Development of high-speed quality control characterization techniques can help ensure high-quality manufacturing and can reduce quality inspection costs, making it extremely valuable to battery manufacturers.

Appendices

Appendix A: Calculation of Theoretical Binder Layer Thickness

To calculate the theoretical binder layer thickness, the total binder volume in the formulation was divided by the total available particle surface area.

$$t_{binder,theoretical} = \frac{\rho_b f_b}{A_{Si} f_{Si} + A_C f_C} m_{tot}$$

, where ρ_b is the binder density, f_b, f_{Si}, and f_c are the weight fractions of binder, silicon, and carbon, respectively, A_{Si} and A_c are the gravimetric surface area (typically reported in units of m^2 g^{-1}) for the silicon and carbon particles, and m_{tot} is the total solid mass of the electrode formulation. m_{tot} excludes the solvent mass in the slurry.

We used the Brunauer, Emmett, and Teller (BET) surface areas provided by the materials suppliers. The gravimetric surface area for the electrode particles was 80 m^2 g^{-1} for the xG Sciences GNP H5 conductive additive and 3.49 m^2 g^{-1} for the Elkem e409 silicon microparticles. The Ube U-Varnish A polyimide density was 1.5 g mL^{-1}.

Appendix B: Definition of Cell Expansions for Calculation of True Energy Density

Cell volume expansion:

$$\Delta v_{cell} = \Delta v_{anode} + \Delta v_{cathode}$$

, where Δv_{cell}, Δv_{anode}, and $\Delta v_{cathode}$ are the volume change in the cell, anode, and cathode electrodes, respectively.

Total anode electrode expansion:

$$\Delta v_{anode,tot} = \Delta v_{anode,rev} + \Delta v_{anode,irr}$$

, where $\Delta v_{anode,tot}$, $\Delta v_{anode,rev}$, and $\Delta v_{anode,irr}$ are the total, reversible, and irreversible anode electrode volume expansions, respectively.

Total cathode electrode expansion:

$$\Delta v_{cathode,tot} = \Delta v_{cathode,rev} + \Delta v_{cathode,irr}$$

, where $\Delta v_{cathode,tot}$, $\Delta v_{cathode,rev}$, and $\Delta v_{cathode,irr}$ are the total, reversible, and irreversible cathode electrode volume expansions, respectively.

Calculation of true volumetric energy density:

$$E_{volumetric} = \frac{V_{cell} Q_{cell}}{(v_{cell} + \Delta v_{cell})}$$

, where V_{cell} is the nominal cell voltage, Q_{cell} is the cell capacity, v_{cell} is the sum of the anode, cathode, separator, and current collector volumes, and Δv_{cell} is the volume expansion of the cell.

Appendix C: Additional Details on Data Calibration and Processing Procedures for Magnetic Dilatometry

The calibration curve establishes the linear relationship between the load measured at the external magnet and the distance between the external magnet and ferritic spacer in the coin cell.

The calibration data contains a known series of position increments measured from the load cell sensor. There is some extraneous data since these calibration data points are collected by hand. For example, there is some variability in the timing and spacing of the steps. To identify and isolate the relevant calibration data, an "ideal" series of steps is constructed at fixed positional increments matching those used in the calibration, i.e., 50 μm step movements of the external magnet and load cell. The data for both the constructed steps and the measured calibration data is normalized between 0 and 1 to ensure both sets of data fall within the same scale.

To identify where the calibration data begins and ends, a method called 'dynamic time warping' (DTW) is used. A DTW algorithm measures the distance between two time series data sets containing some similar feature. The normalized constructed data is swept across the normalized measured data, in both forward and reverse, through the DTW algorithm. The location of the minimum distance recorded in the forward sweep is used to denote the beginning of the calibration data, and the minimum distance recorded in the reverse sweep is used to denote the end of the calibration data. This allows the extraneous data at the beginning and end of the record to be discarded.

To clean up any data points that fall between calibration steps, the difference between each data point and the two data points surrounding it is calculated. Data points that appear in a calibration step will show only a very small difference in at least one direction, while extraneous

data points will show some substantial amount of difference in both directions. Any points with substantial difference in both directions are discarded.

After the calibration data has been isolated and cleaned, the calibration steps are binned and labeled. The isolated calibration data is again run through a differencing algorithm, with the result being run through a kernel density estimate (KDE) algorithm to determine the typical difference between calibration steps. A KDE algorithm works like a continuous histogram, with peaks appearing at values estimated to be the most common. In this case, two peaks are expected, with the tallest peak at zero, and a shorter peak around the typical step height. Using this approximate step height, the data points are iterated through, binned, and labeled with their corresponding expected measured height in microns.

With the calibration data binned and labeled, the median value at each step is selected or calculated and run through a linear regression algorithm to determine the slope between the measured value from the load cell and the actual entered distance in microns. The slope and the R^2 value are recorded in the measurement file.

To determine the linear offset, the measured sensor value at the beginning of the test is used. The position at the beginning of the test is subtracted from all measurements, ensuring that the measured load cell value at the beginning of the test is equal to 0.

Since the load cell data is collected separately from the cycler data, the data sampling rates do not match between the two data streams. To correct this, the load cell data is interpolated to match the time scale of the cycler data.

With the cell expansion measurement data calibrated and interpolated, the statistical data needs to be compiled. Using the cycle number that is included in each measurement record from the battery cycler, the measured height at the beginning of the cycle and the minimum and maximum heights during the cycle are identified and appended to the provided per-cycle data from the cycler.

The Python and library versions used for this code were Anaconda 2022.10, Python 3.9.13, pandas 1.4.4, NumPy 1.21.5, SciPy 1.9.1, FastDTW 0.3.4, sklearn 0.0.post1, openpyxl

3.0.10, and the editor used was Jupyter Notebook 6.4.12. The KDE algorithm is included in the pandas library and the DTW algorithm is from the FastDTW library.

Appendix D: Connected Electrode Porosity Calculation

We assume there is some electrolyte uptake into the binder and some into the connected, accessible pores. To estimate binder uptake of the electrolyte, thin coatings of binder, without any silicon or carbon, were soaked in electrolyte for 18 hours and weighed before and after soaking. From this experiment, we determined the percentage weight gain from electrolyte uptake.

$$\%\ uptake = \frac{\left(m_{binder,after\ soak} - m_{binder,before\ soak}\right)}{m_{binder,after\ soak}}$$

, where $m_{binder,\ after\ soak}$ and $m_{binder,\ before\ soak}$ are the masses of the binder coating before and after soaking in electrolyte. To find the weight of the electrolyte in the binder after soaking the electrode, w_{binder}, we multiply the weight of the binder in the electrode with the % uptake:

$$W_{binder} = \%uptake \times dry\ binder\ mass$$

Connected porosity was measured by soaking electrode punches in electrolyte overnight and weighing the electrodes before and after soaking. The total weight gain, w_{tot}, is the difference between the electrode weight before and after soaking. We subtract the mass of electrolyte that we expect to be taken up by the binder from w_{tot} to estimate the weight of electrolyte in the connected pores, $w_{connected\ pores}$:

$$W_{tot} - W_{binder} = W_{Connected\ pores}$$

We assume that all binder has access to the electrolyte, which we understand may overestimate the amount of electrolyte in the binder. In electrodes where the binder is inaccessible to electrolyte due to low porosity, the amount of electrolyte in the binder will be overestimated and the connected porosity will be underestimated. In electrodes where binder is more accessible to electrolyte, our assumption will provide a more accurate assessment of connected porosity.

We then convert the weight of electrolyte in the pores to pore volume using the electrolyte density, as follows:

$$W_{pores} \times \frac{1}{\rho_{electrolyte}} = V_{electrolyte,\ pores} = V_{pores,\ connected}$$

And to calculate a fraction of connected pore volume by comparing with total pore volume:

$$\frac{V_{pores,connected}}{V_{pores,total}} = \%\ of\ connected\ pore\ volume$$

Appendix E: Toward Measurement of Lithium-Ion Diffusion Coefficients in Thin Film Polymeric Binders

We aimed to use potentiostatic intermittent titration (PITT) on binder-coated silicon wafers to measure lithium-ion diffusion coefficients through polymeric binders. We created a model system for this measurement. PI is often coated and patterned on Si wafers for use as a sacrificial or insulating layer in semiconductor devices and is known to be an effective binder for silicon anodes.

Silicon wafers were purchased from SVMI (Santa Clara, CA) (3" diameter, 250 ± 25 μm thickness, <100>, <0.005 Ω cm resistivity, P/Boron doped, single-side polished, back side etched, single flat). We note that 4" wafers are the standard for processing at the Lurie Nanofabrication lab and is a more convenient wafer size choice. We selected a low resistivity wafer to help with conductivity concerns between the Si and current collector. We also chose a very thin wafer thickness to further limit any electronic barriers to lithiation.

Thin films of PI binder were spin-coated onto low resistivity silicon wafers at the ROBIN lab, Lurie Nanofabrication Laboratory (LNF) at University of Michigan. After spin-coating, the wafer was soft-baked on a hot plate for 2 minutes at 150°C, so that most the solvent could be dried before curing. The coating was then cured in a vacuum oven purged with nitrogen for 30 minutes at 350°C. Coating thicknesses were measured using the Woollam ellipsometer at LNF. Then the wafers were diced into 10 x 10 mm squares for assembly into coin cells.

For the PITT measurement, lithium-metal half cell coin cells were assembled using glass fiber separators to prevent silicon wafer cracking during coin cell build. We succeeded in lithiating some uncoated wafers and measured a lithiation depth of approximately 20 nm using transmission electron microscopy on a PFIB section of the wafer (imaging work by Tao Ma).

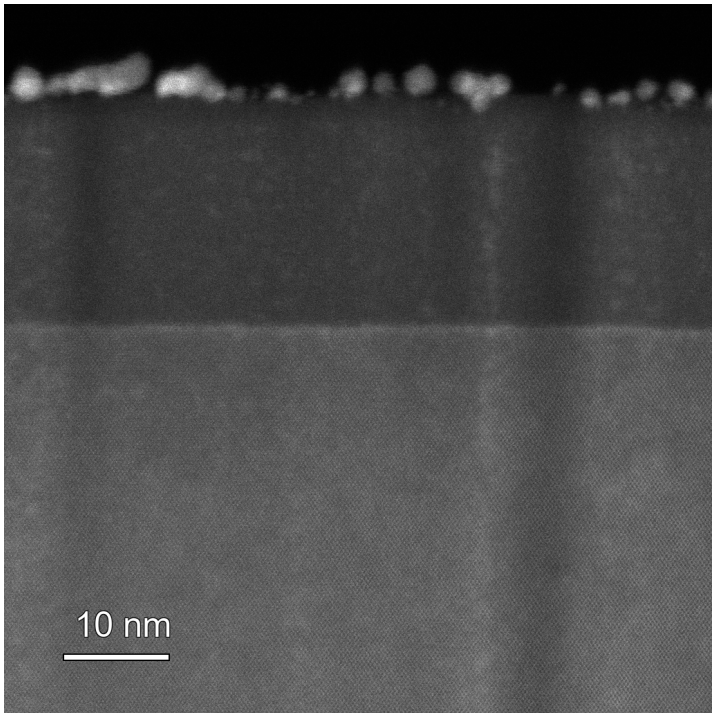

Appendix Figure 51. TEM image of silicon wafer that was lithiated in a coin cell and delithiated prior to imaging. Top layer = capping layer, middle layer = amorphized silicon (previously lithiated region), bottom layer = crystalline silicon wafer.

However, experimental repeatability was an issue. Diffusion coefficients obtained via PITT had high variation and did not correspond well to published values in literature. It was also difficult to confine the lithiation to the top surface of the silicon wafer. We hypothesize that application of a blocking layer to the sides and back of the silicon wafer could be helpful, as our strategy of limiting electrolyte volume resulted in conductivity issues. Unsurprisingly, lithiation of polyimide coated wafers was even more unreliable and difficult due to the low conductivity and uncertain uniformity of the polyimide coating.

Bibliography

1. Gohlke, D., Zhou, Y., Wu, X. & Courtney, C. *Assessment of Light-Duty Plug-in Electric Vehicles in the United States, 2010 – 2021*. https://www.osti.gov/biblio/1898424 (2022) doi:10.2172/1898424.
2. Cano, Z. P. *et al.* Batteries and fuel cells for emerging electric vehicle markets. *Nat. Energy* **3**, 279–289 (2018).
3. Nykvist, B. & Nilsson, M. Rapidly falling costs of battery packs for electric vehicles. *Nat. Clim. Change* **5**, 329–332 (2015).
4. Liu, Z. *et al.* Comparing total cost of ownership of battery electric vehicles and internal combustion engine vehicles. *Energy Policy* **158**, 112564 (2021).
5. Liu, Y., Zhu, Y. & Cui, Y. Challenges and opportunities towards fast-charging battery materials. *Nat. Energy* **4**, 540–550 (2019).
6. McDowell, M. T., Lee, S. W., Nix, W. D. & Cui, Y. 25th Anniversary Article: Understanding the Lithiation of Silicon and Other Alloying Anodes for Lithium-Ion Batteries. *Adv. Mater.* **25**, 4966–4985 (2013).
7. Obrovac, M. N., Christensen, L., Le, D. B. & Dahn, J. R. Alloy Design for Lithium-Ion Battery Anodes. *J. Electrochem. Soc.* **154**, A849 (2007).
8. Haxel, G., Hedrick, J. B. & Orris, G. *Rare Earth Elements—Critical Resources for High Technology | USGS Fact Sheet 087-02*. https://pubs.usgs.gov/fs/2002/fs087-02/ (2002).
9. G. Gallagher, K. *et al.* Quantifying the promise of lithium–air batteries for electric vehicles. *Energy Environ. Sci.* **7**, 1555–1563 (2014).

10. Howell, D., Cunningham, B., Duong, T. & Faguy, P. *Overview of the DOE VTO Advanced Battery R&D Program*. https://www.energy.gov/eere/vehicles/articles/vehicle-technologies-office-merit-review-2016-overview-doe-vto-advanced (2016).

11. McBrayer, J. D. *et al.* Calendar aging of silicon-containing batteries. *Nat. Energy* **6**, 866–872 (2021).

12. John, A. S. Automakers are betting on range and performance to win the electric vehicle wars. These 17 battery startups could reap the rewards by delivering an energy breakthrough. *Business Insider* (2022).

13. Blois, M. Silicon anode battery companies get a major boost. *Chemical & Engineering News* (2022).

14. Patel, P. The Age of Silicon Is Here…for Batteries. *IEEE Spectrum* (2023).

15. Sharma, R. A. & Seefurth, R. N. Thermodynamic Properties of the Lithium-Silicon System. *J. Electrochem. Soc.* **123**, 1763 (1976).

16. The Lithium Paradigm. *Chem. Eng. News Arch.* **58**, 5–7 (1980).

17. Wen, C. J. & Huggins, R. A. Chemical diffusion in intermediate phases in the lithium-silicon system. *J. Solid State Chem.* **37**, 271–278 (1981).

18. Yoshino, A. The Birth of the Lithium-Ion Battery. *Angew. Chem. Int. Ed.* **51**, 5798–5800 (2012).

19. Wilson, A. M., Way, B. M., Dahn, J. R. & van Buuren, T. Nanodispersed silicon in pregraphitic carbons. *J. Appl. Phys.* **77**, 2363–2369 (1995).

20. Wang, C. S., Wu, G. T., Zhang, X. B., Qi, Z. F. & Li, W. Z. Lithium Insertion in Carbon-Silicon Composite Materials Produced by Mechanical Milling. *J. Electrochem. Soc.* **145**, 2751 (1998).

21. Yang, J., Winter, M. & Besenhard, J. O. Small particle size multiphase Li-alloy anodes for lithium-ionbatteries. *Solid State Ion.* **90**, 281–287 (1996).

22. Liu, X. H. *et al.* Size-Dependent Fracture of Silicon Nanoparticles During Lithiation. *ACS Nano* **6**, 1522–1531 (2012).

23. Li, H., Huang, X., Chen, L., Wu, Z. & Liang, Y. A High Capacity Nano - Si Composite Anode Material for Lithium Rechargeable Batteries. *Electrochem. Solid-State Lett.* **2**, 547 (1999).

24. Chan, C. K. *et al.* High-performance lithium battery anodes using silicon nanowires. *Nat. Nanotechnol.* **3**, 31–35 (2008).

25. Cui, L.-F., Yang, Y., Hsu, C.-M. & Cui, Y. Carbon–Silicon Core–Shell Nanowires as High Capacity Electrode for Lithium Ion Batteries. *Nano Lett.* **9**, 3370–3374 (2009).

26. Magasinski, A. *et al.* High-performance lithium-ion anodes using a hierarchical bottom-up approach. *Nat. Mater.* **9**, 353–358 (2010).

27. Wada, T. *et al.* Bulk-Nanoporous-Silicon Negative Electrode with Extremely High Cyclability for Lithium-Ion Batteries Prepared Using a Top-Down Process. *Nano Lett.* **14**, 4505–4510 (2014).

28. Yao, Y. *et al.* Interconnected Silicon Hollow Nanospheres for Lithium-Ion Battery Anodes with Long Cycle Life. *Nano Lett.* **11**, 2949–2954 (2011).

29. Vila, M. N. *et al.* Interfacial Reactivity of Silicon Electrodes: Impact of Electrolyte Solvent and Presence of Conductive Carbon. *ACS Appl. Mater. Interfaces* **14**, 20404–20417 (2022).

30. Parkinson, C., Matsumoto, S. & Sherman, P. The influence of particle-size distribution on the apparent viscosity of non-newtonian dispersed systems. *J. Colloid Interface Sci.* **33**, 150–160 (1970).

31. He, M., Wang, Y. & Forssberg, E. Slurry rheology in wet ultrafine grinding of industrial minerals: a review. *Powder Technol.* **147**, 94–112 (2004).

32. Shaffer, R. E. & Rengasamy, S. Respiratory protection against airborne nanoparticles: a review. *J. Nanoparticle Res.* **11**, 1661–1672 (2009).

33. Zhao, Y., Liu, X., Li, H., Zhai, T. & Zhou, H. Hierarchical micro/nano porous silicon Li-ion battery anodes. *Chem. Commun.* **48**, 5079–5081 (2012).

34. Mazouzi, D. *et al.* Critical roles of binders and formulation at multiscales of silicon-based composite electrodes. *J. Power Sources* **280**, 533–549 (2015).

35. Choi, N.-S. *et al.* Recent Progress on Polymeric Binders for Silicon Anodes in Lithium-Ion Batteries. *J. Electrochem. Sci. Technol.* **6**, 35–49 (2015).

36. Lopez, J., Mackanic, D. G., Cui, Y. & Bao, Z. Designing polymers for advanced battery chemistries. *Nat. Rev. Mater.* **4**, 312–330 (2019).

37. Kwon, T., Choi, J. W. & Coskun, A. The emerging era of supramolecular polymeric binders in silicon anodes. *Chem. Soc. Rev.* **47**, 2145–2164 (2018).

38. Yang, Y. *et al.* Towards efficient binders for silicon based lithium-ion battery anodes. *Chem. Eng. J.* **406**, 126807 (2021).

39. Preman, A. N. *et al.* Progress of 3D network binders in silicon anodes for lithium ion batteries. *J. Mater. Chem. A* **8**, 25548–25570 (2020).

40. Li, S. *et al.* A review of rational design and investigation of binders applied in silicon-based anodes for lithium-ion batteries. *J. Power Sources* **485**, 229331 (2021).

41. Han, B. *et al.* Probing the Reaction between PVDF and LiPAA vs Li7Si3: Investigation of Binder Stability for Si Anodes. *J. Electrochem. Soc.* **166**, A2396 (2019).

42. Li, J., Lewis, R. B. & Dahn, J. R. Sodium Carboxymethyl Cellulose: A Potential Binder for Si Negative Electrodes for Li-Ion Batteries. *Electrochem. Solid-State Lett.* **10**, A17 (2006).

43. Magasinski, A. *et al.* Toward Efficient Binders for Li-Ion Battery Si-Based Anodes: Polyacrylic Acid. *ACS Appl. Mater. Interfaces* **2**, 3004–3010 (2010).

44. Kovalenko, I. *et al.* A Major Constituent of Brown Algae for Use in High-Capacity Li-Ion Batteries. *Science* **334**, 75–79 (2011).

45. Vogl, U. S. *et al.* Mechanism of Interactions between CMC Binder and Si Single Crystal Facets. *Langmuir* **30**, 10299–10307 (2014).

46. Hochgatterer, N. S. *et al.* Silicon/Graphite Composite Electrodes for High-Capacity Anodes: Influence of Binder Chemistry on Cycling Stability. *Electrochem. Solid-State Lett.* **11**, A76 (2008).

47. Delpuech, N. *et al.* Critical Role of Silicon Nanoparticles Surface on Lithium Cell Electrochemical Performance Analyzed by FTIR, Raman, EELS, XPS, NMR, and BDS Spectroscopies. *J. Phys. Chem. C* **118**, 17318–17331 (2014).

48. Dang, D. *et al.* Lithium Substituted Poly(acrylic acid) as a Mechanically Robust Binder for Low-Cost Silicon Microparticle Electrodes. *ACS Appl. Energy Mater.* **3**, 10940–10949 (2020).

49. Mazouzi, D., Lestriez, B., Roué, L. & Guyomard, D. Silicon Composite Electrode with High Capacity and Long Cycle Life. *Electrochem. Solid-State Lett.* **12**, A215 (2009).

50. Bridel, J.-S., Azaïs, T., Morcrette, M., Tarascon, J.-M. & Larcher, D. In Situ Observation and Long-Term Reactivity of Si/C/CMC Composites Electrodes for Li-Ion Batteries. *J. Electrochem. Soc.* **158**, A750 (2011).

51. Jung, C.-H., Kim, K.-H. & Hong, S.-H. Stable Silicon Anode for Lithium-Ion Batteries through Covalent Bond Formation with a Binder via Esterification. *ACS Appl. Mater. Interfaces* **11**, 26753–26763 (2019).

52. Nguyen, C. C., Seo, D. M., Chandrasiri, K. W. D. K. & Lucht, B. L. Improved Cycling Performance of a Si Nanoparticle Anode Utilizing Citric Acid as a Surface-Modifying Agent. *Langmuir* **33**, 9254–9261 (2017).

53. Wilkes, B. N., Brown, Z. L., Krause, L. J., Triemert, M. & Obrovac, M. N. The Electrochemical Behavior of Polyimide Binders in Li and Na Cells. *J. Electrochem. Soc.* **163**, A364 (2015).

54. Kim, J. S. *et al.* Effect of polyimide binder on electrochemical characteristics of surface-modified silicon anode for lithium ion batteries. *J. Power Sources* **244**, 521–526 (2013).

55. Uchida, S., Mihashi, M., Yamagata, M. & Ishikawa, M. Electrochemical properties of non-nano-silicon negative electrodes prepared with a polyimide binder. *J. Power Sources* **273**, 118–122 (2015).

56. Kwon, T. *et al.* Systematic Molecular-Level Design of Binders Incorporating Meldrum's Acid for Silicon Anodes in Lithium Rechargeable Batteries. *Adv. Mater.* **26**, 7979–7985 (2014).

57. Cho, Y. *et al.* A Pyrene–Poly(acrylic acid)–Polyrotaxane Supramolecular Binder Network for High-Performance Silicon Negative Electrodes. *Adv. Mater.* **31**, 1905048 (2019).

58. Choi, S., Kwon, T., Coskun, A. & Choi, J. W. Highly elastic binders integrating polyrotaxanes for silicon microparticle anodes in lithium ion batteries. *Science* **357**, 279–283 (2017).

59. Cao, P.-F. *et al.* Rational Design of a Multifunctional Binder for High-Capacity Silicon-Based Anodes. *ACS Energy Lett.* **4**, 1171–1180 (2019).

60. Koo, B. *et al.* A Highly Cross-Linked Polymeric Binder for High-Performance Silicon Negative Electrodes in Lithium Ion Batteries. *Angew. Chem. Int. Ed.* **51**, 8762–8767 (2012).

61. Liu, G. *et al.* Polymers with Tailored Electronic Structure for High Capacity Lithium Battery Electrodes. *Adv. Mater.* **23**, 4679–4683 (2011).

62. Higgins, T. M. *et al.* A Commercial Conducting Polymer as Both Binder and Conductive Additive for Silicon Nanoparticle-Based Lithium-Ion Battery Negative Electrodes. *ACS Nano* **10**, 3702–3713 (2016).

63. Zeng, W. *et al.* Enhanced Ion Conductivity in Conducting Polymer Binder for High-Performance Silicon Anodes in Advanced Lithium-Ion Batteries. *Adv. Energy Mater.* **8**, 1702314 (2018).

64. Wang, L. *et al.* Highly Stretchable Conductive Glue for High-Performance Silicon Anodes in Advanced Lithium-Ion Batteries. *Adv. Funct. Mater.* **28**, 1704858 (2018).

65. Zhao, H. *et al.* Toward Practical Application of Functional Conductive Polymer Binder for a High-Energy Lithium-Ion Battery Design. *Nano Lett.* **14**, 6704–6710 (2014).

66. Gao, S. *et al.* Ultra-efficient polymer binder for silicon anode in high-capacity lithium-ion batteries. *Nano Energy* **73**, 104804 (2020).

67. Park, S.-J. *et al.* Side-Chain Conducting and Phase-Separated Polymeric Binders for High-Performance Silicon Anodes in Lithium-Ion Batteries. *J. Am. Chem. Soc.* **137**, 2565–2571 (2015).

68. USABC Goals for Low-Cost / Fast-Charge Advanced Batteries for EVs - CY 2023. https://uscar.org/usabc/.

69. Callister, W. D. & Rethwisch, D. G. *Materials Science and Engineering*. (Wiley).

70. Zhilkashinova, A. M., Kabdrakhmanova, S. K., Troyeglazova, A. V. & Abilev, M. B. Structure and Properties of Metallurgical-grade Silicon. *Silicon* **10**, 2201–2210 (2018).

71. Raider, S. I., Flitsch, R. & Palmer, M. J. Oxide Growth on Etched Silicon in Air at Room Temperature. *J. Electrochem. Soc.* **122**, 413 (1975).

72. El-Kareh, B. Thermal Oxidation and Nitridation. in *Fundamentals of Semiconductor Processing Technology* (ed. El-Kareh, B.) 39–85 (Springer US, 1995). doi:10.1007/978-1-4615-2209-6_2.

73. Kirchmeyer, S. & Reuter, K. Scientific importance, properties and growing applications of poly(3,4-ethylenedioxythiophene). *J. Mater. Chem.* **15**, 2077–2088 (2005).

74. Moharram, M. A., Soliman, M. A. & El-Gendy, H. M. Electrical conductivity of poly(acrylic acid)–polyacrylamide complexes. *J. Appl. Polym. Sci.* **68**, 2049–2055 (1998).

75. McKeen, L. W. 11 - Fluoropolymers. in *Film Properties of Plastics and Elastomers (Fourth Edition)* (ed. McKeen, L. W.) 317–388 (William Andrew Publishing, 2017). doi:10.1016/B978-0-12-813292-0.00011-3.

76. McKeen, L. W. 7 - Polyimides. in *Film Properties of Plastics and Elastomers (Fourth Edition)* (ed. McKeen, L. W.) 147–185 (William Andrew Publishing, 2017). doi:10.1016/B978-0-12-813292-0.00007-1.

77. Peled, E. & Menkin, S. Review—SEI: Past, Present and Future. *J. Electrochem. Soc.* **164**, A1703 (2017).

78. Wissler, M. Graphite and carbon powders for electrochemical applications. *J. Power Sources* **156**, 142–150 (2006).

79. Kühner, G. & Voll, M. Manufacture of Carbon Black. in *Carbon Black* (Routledge).

80. Probst, N. Conducting Carbon Black. in *Carbon Black* (Routledge, 1993).

81. Spahr, M. E., Goers, D., Leone, A., Stallone, S. & Grivei, E. Development of carbon conductive additives for advanced lithium ion batteries. *J. Power Sources* **196**, 3404–3413 (2011).

82. Dutta, A. K. Electrical Conductivity of Single Crystals of Graphite. *Phys. Rev.* **90**, 187–192 (1953).

83. Heremans, J. Electrical conductivity of vapor-grown carbon fibers. *Carbon* **23**, 431–436 (1985).

84. Endo, M. *et al.* Vapor-grown carbon fibers (VGCFs): Basic properties and their battery applications. *Carbon* **39**, 1287–1297 (2001).

85. Marinho, B., Ghislandi, M., Tkalya, E., Koning, C. E. & de With, G. Electrical conductivity of compacts of graphene, multi-wall carbon nanotubes, carbon black, and graphite powder. *Powder Technol.* **221**, 351–358 (2012).

86. Ebbesen, T. W. *et al.* Electrical conductivity of individual carbon nanotubes. *Nature* **382**, 54–56 (1996).

87. Teoh, H., Metz, P. D. & Wilhelm, W. G. Electrical conductivity of pyrolyzed polyacrylonitrile. *Mol. Cryst. Liq. Cryst.* **83**, 297–306 (1982).

88. Barnes, H. A., Hutton, J. F. & Walters, K. Chapter 7 - Rheology of Suspensions. in *An Introduction to Rheology* vol. 3 115–139 (Elsevier, 1989).

89. Duffner, F., Mauler, L., Wentker, M., Leker, J. & Winter, M. Large-scale automotive battery cell manufacturing: Analyzing strategic and operational effects on manufacturing costs. *Int. J. Prod. Econ.* **232**, 107982 (2021).

90. Li, J., Li, H., Stone, W., Glazier, S. & Dahn, J. R. Development of Electrolytes for Single Crystal NMC532/Artificial Graphite Cells with Long Lifetime. *J. Electrochem. Soc.* **165**, A626 (2018).

91. Structural evolution and capacity degradation mechanism of LiNi0.6Mn0.2Co0.2O2 cathode materials. *J. Power Sources* **400**, 539–548 (2018).

92. Zhang, C. (John) *et al.* High capacity silicon anodes enabled by MXene viscous aqueous ink. *Nat. Commun.* **10**, 849 (2019).

93. Vehicle Technologies Office - Batteries. *Energy.gov* https://www.energy.gov/eere/vehicles/batteries.

94. Neale, N. R. *Silicon Consortium Project: Next-Gen Materials for Silicon Anodes*. https://www.energy.gov/eere/vehicles/articles/silicon-consortium-project-next-gen-materials-silicon-anodes (2021).

95. Jia, H. *et al.* Hierarchical porous silicon structures with extraordinary mechanical strength as high-performance lithium-ion battery anodes. *Nat. Commun.* **11**, 1474 (2020).

96. Wang, C. *et al.* Self-healing chemistry enables the stable operation of silicon microparticle anodes for high-energy lithium-ion batteries. *Nat. Chem.* **5**, 1042–1048 (2013).

97. Obrovac, M. N. & Chevrier, V. L. Alloy negative electrodes for Li-ion batteries. *Chem. Rev.* **114**, 11444–11502 (2014).

98. Kim, N., Chae, S., Ma, J., Ko, M. & Cho, J. Fast-charging high-energy lithium-ion batteries via implantation of amorphous silicon nanolayer in edge-plane activated graphite anodes. *Nat. Commun.* **8**, 812 (2017).

99. Nguyen, B. P. N., Chazelle, S., Cerbelaud, M., Porcher, W. & Lestriez, B. Manufacturing of industry-relevant silicon negative composite electrodes for lithium ion-cells. *J. Power Sources* **262**, 112–122 (2014).

100. Beaulieu, L. Y., Hatchard, T. D., Bonakdarpour, A., Fleischauer, M. D. & Dahn, J. R. Reaction of Li with Alloy Thin Films Studied by In Situ AFM. *J. Electrochem. Soc.* **150**, A1457 (2003).

101. Aricò, A. S., Bruce, P., Scrosati, B., Tarascon, J.-M. & van Schalkwijk, W. Nanostructured materials for advanced energy conversion and storage devices. *Nat. Mater.* **4**, 366–377 (2005).

102. Jin, M. Y. *et al.* Optimum Particle Size in Silicon Electrodes Dictated by Chemomechanical Deformation of the SEI. *Adv. Funct. Mater.* **31**, 2010640 (2021).

103. Andersen, H. F. *et al.* Silicon-Carbon composite anodes from industrial battery grade silicon. *Sci. Rep.* **9**, 14814 (2019).

104. Wilson, A. M. & Dahn, J. R. Lithium Insertion in Carbons Containing Nanodispersed Silicon. *J. Electrochem. Soc.* **142**, 326 (1995).

105. Zhu, G., Chao, D., Xu, W., Wu, M. & Zhang, H. Microscale Silicon-Based Anodes: Fundamental Understanding and Industrial Prospects for Practical High-Energy Lithium-Ion Batteries. *ACS Nano* **15**, 15567–15593 (2021).

106. Zou, F. & Manthiram, A. A Review of the Design of Advanced Binders for High-Performance Batteries. *Adv. Energy Mater.* **10**, 2002508 (2020).

107. Lopez, J. *et al.* The Effects of Cross-Linking in a Supramolecular Binder on Cycle Life in Silicon Microparticle Anodes. *ACS Appl. Mater. Interfaces* **8**, 2318–2324 (2016).

108. Xu, Z. *et al.* Silicon Microparticle Anodes with Self-Healing Multiple Network Binder. *Joule* **2**, 950–961 (2018).

109. Burdette-Trofimov, M. K. *et al.* Understanding Binder–Silicon Interactions during Slurry Processing. *J. Phys. Chem. C* **124**, 13479–13494 (2020).

110. Burdette-Trofimov, M. K. *et al.* Competitive adsorption within electrode slurries and impact on cell fabrication and performance. *J. Power Sources* **520**, 230914 (2022).

111. Liu, H. *et al.* Advanced electrode processing of lithium ion batteries: A review of powder technology in battery fabrication. *Particuology* **57**, 56–71 (2021).

112. Landesfeind, J., Eldiven, A. & Gasteiger, H. A. Influence of the Binder on Lithium Ion Battery Electrode Tortuosity and Performance. *J. Electrochem. Soc.* **165**, A1122 (2018).

113. Wang, Y., Dang, D., Li, D., Hu, J. & Cheng, Y.-T. Influence of polymeric binders on mechanical properties and microstructure evolution of silicon composite electrodes during electrochemical cycling. *J. Power Sources* **425**, 170–178 (2019).

114. Li, D. *et al.* Role of polymeric binders on mechanical behavior and cracking resistance of silicon composite electrodes during electrochemical cycling. *J. Power Sources* **387**, 9–15 (2018).

115. Nguyen, C. C., Yoon, T., Seo, D. M., Guduru, P. & Lucht, B. L. Systematic Investigation of Binders for Silicon Anodes: Interactions of Binder with Silicon Particles and Electrolytes and Effects of Binders on Solid Electrolyte Interphase Formation. *ACS Appl. Mater. Interfaces* **8**, 12211–12220 (2016).

116. Browning, K. L. *et al.* The Study of the Binder Poly(acrylic acid) and Its Role in Concomitant Solid–Electrolyte Interphase Formation on Si Anodes. *ACS Appl. Mater. Interfaces* **12**, 10018–10030 (2020).

117. Han, L. *et al.* Undervalued Roles of Binder in Modulating Solid Electrolyte Interphase Formation of Silicon-Based Anode Materials. *ACS Appl. Mater. Interfaces* **13**, 45139–45148 (2021).

118. Parikh, P. *et al.* Role of Polyacrylic Acid (PAA) Binder on the Solid Electrolyte Interphase in Silicon Anodes. *Chem. Mater.* **31**, 2535–2544 (2019).

119. Porcher, W. *et al.* Understanding Polyacrylic Acid and Lithium Polyacrylate Binder Behavior in Silicon Based Electrodes for Li-Ion Batteries. *J. Electrochem. Soc.* **164**, A3633 (2017).

120. Liu, T. *et al.* Interweaving 3D Network Binder for High-Areal-Capacity Si Anode through Combined Hard and Soft Polymers. *Adv. Energy Mater.* **9**, 1802645 (2019).

121. Marks, T., Trussler, S., Smith, A. J., Xiong, D. & Dahn, J. R. A Guide to Li-Ion Coin-Cell Electrode Making for Academic Researchers. *J. Electrochem. Soc.* **158**, A51 (2010).

122. Hu, J., Wang, Y., Li, D. & Cheng, Y.-T. Effects of adhesion and cohesion on the electrochemical performance and durability of silicon composite electrodes. *J. Power Sources* **397**, 223–230 (2018).

123. Limthongkul, P., Jang, Y. Il, Dudney, N. J. & Chiang, Y. M. Electrochemically-driven solid-state amorphization in lithium-silicon alloys and implications for lithium storage. *Acta Mater.* **51**, 1103–1113 (2003).

124. Yang, H., Liu, S., Cao, L., Jiang, S. & Hou, H. Superlithiation of non-conductive polyimide toward high-performance lithium-ion batteries. *J. Mater. Chem. A* **6**, 21216–21224 (2018).

125. Kim, Y. *et al.* Electrochemical investigation on high-rate properties of graphene nanoplatelet-carbon nanotube hybrids for Li-ion capacitors. *J. Electroanal. Chem.* **863**, 114060 (2020).

126. Obrovac, M. N. & Christensen, L. Structural Changes in Silicon Anodes during Lithium Insertion/Extraction. *Electrochem. Solid-State Lett.* **7**, A93 (2004).

127. Michan, A. L. *et al.* Solid Electrolyte Interphase Growth and Capacity Loss in Silicon Electrodes. *J. Am. Chem. Soc.* **138**, 7918–7931 (2016).

128. Hu, J., Wang, Y., Li, D. & Cheng, Y. T. Effects of adhesion and cohesion on the electrochemical performance and durability of silicon composite electrodes. *J. Power Sources* **397**, 223–230 (2018).

129. Dang, D. *et al.* Lithium Substituted Poly(acrylic acid) as a Mechanically Robust Binder for Low-Cost Silicon Microparticle Electrodes. *ACS Appl. Energy Mater.* **3**, 10940–10949 (2020).

130. Choi, S., Kwon, T. woo, Coskun, A. & Choi, J. W. Highly elastic binders integrating polyrotaxanes for silicon microparticle anodes in lithium ion batteries. *Science* **357**, 279–283 (2017).

131. Harlow, J. E. *et al.* A Wide Range of Testing Results on an Excellent Lithium-Ion Cell Chemistry to be used as Benchmarks for New Battery Technologies. *J. Electrochem. Soc.* **166**, A3031 (2019).

132. Baasner, A. *et al.* The Role of Balancing Nanostructured Silicon Anodes and NMC Cathodes in Lithium-Ion Full-Cells with High Volumetric Energy Density. *J. Electrochem. Soc.* **167**, 020516 (2020).

133. Rodrigues, M.-T. F. *et al.* Modulating electrode utilization in lithium-ion cells with silicon-bearing anodes. *J. Power Sources* **477**, 229029 (2020).

134. Jung, R., Metzger, M., Maglia, F., Stinner, C. & Gasteiger, H. A. Oxygen Release and Its Effect on the Cycling Stability of LiNixMnyCozO2 (NMC) Cathode Materials for Li-Ion Batteries. *J. Electrochem. Soc.* **164**, A1361 (2017).

135. Jung, R., Metzger, M., Maglia, F., Stinner, C. & Gasteiger, H. A. Chemical versus Electrochemical Electrolyte Oxidation on NMC111, NMC622, NMC811, LNMO, and Conductive Carbon. *J. Phys. Chem. Lett.* **8**, 4820–4825 (2017).

136. Entwistle, J., Ge, R., Pardikar, K., Smith, R. & Cumming, D. Carbon binder domain networks and electrical conductivity in lithium-ion battery electrodes: A critical review. *Renew. Sustain. Energy Rev.* **166**, 112624 (2022).

137. Ogihara, N. *et al.* Theoretical and Experimental Analysis of Porous Electrodes for Lithium-Ion Batteries by Electrochemical Impedance Spectroscopy Using a Symmetric Cell. *J. Electrochem. Soc.* **159**, A1034 (2012).

138. Zheng, H., Yang, R., Liu, G., Song, X. & Battaglia, V. S. Cooperation between Active Material, Polymeric Binder and Conductive Carbon Additive in Lithium Ion Battery Cathode. *J. Phys. Chem. C* **116**, 4875–4882 (2012).

139. Shi, J.-L. *et al.* High-Capacity Cathode Material with High Voltage for Li-Ion Batteries. *Adv. Mater.* **30**, 1705575 (2018).

140. Ogihara, N., Itou, Y., Sasaki, T. & Takeuchi, Y. Impedance Spectroscopy Characterization of Porous Electrodes under Different Electrode Thickness Using a Symmetric Cell for High-Performance Lithium-Ion Batteries. *J. Phys. Chem. C* **119**, 4612–4619 (2015).

141. Zheng, H., Li, J., Song, X., Liu, G. & Battaglia, V. S. A comprehensive understanding of electrode thickness effects on the electrochemical performances of Li-ion battery cathodes. *Electrochimica Acta* **71**, 258–265 (2012).

142. Ju, Z. *et al.* Tortuosity Engineering for Improved Charge Storage Kinetics in High-Areal-Capacity Battery Electrodes. *Nano Lett.* **22**, 6700–6708 (2022).

143. Itou, Y., Ogihara, N. & Kawauchi, S. Role of Conductive Carbon in Porous Li-Ion Battery Electrodes Revealed by Electrochemical Impedance Spectroscopy Using a Symmetric Cell. *J. Phys. Chem. C* **124**, 5559–5564 (2020).

144. Wang, M., Dang, D., Meyer, A., Arsenault, R. & Cheng, Y.-T. Effects of the Mixing Sequence on Making Lithium Ion Battery Electrodes. *J. Electrochem. Soc.* **167**, 100518 (2020).

145. Wang, M. *et al.* Influence of Mixing Process on the Performance of Electrodes Made by a Dry Coating Method. *J. Electrochem. Soc.* **170**, 010541 (2023).

146. doi:10.1016/j.electacta.2016.08.118.

147. Chen, Y.-H. *et al.* Selection of Conductive Additives in Li-Ion Battery Cathodes: A Numerical Study. *J. Electrochem. Soc.* **154**, A978 (2007).

148. Berg, C., Morasch, R., Graf, M. & Gasteiger, H. A. Comparison of Silicon and Graphite Anodes: Temperature-Dependence of Impedance Characteristics and Rate Performance. *J. Electrochem. Soc.* **170**, 030534 (2023).

149. Min Kim, J. *et al.* A novel textile-like carbon wrapping for high-performance silicon anodes in lithium-ion batteries. *J. Mater. Chem. A* **6**, 12475–12483 (2018).

150. Wang, B. *et al.* Ultrafast-Charging Silicon-Based Coral-Like Network Anodes for Lithium-Ion Batteries with High Energy and Power Densities. *ACS Nano* **13**, 2307–2315 (2019).

151. Li, Y. *et al.* Growth of conformal graphene cages on micrometre-sized silicon particles as stable battery anodes. *Nat. Energy* **1**, 1–9 (2016).

152. Weiss, M. *et al.* Fast Charging of Lithium-Ion Batteries: A Review of Materials Aspects. *Adv. Energy Mater.* **11**, 2101126 (2021).

153. Son, I. H. *et al.* Silicon carbide-free graphene growth on silicon for lithium-ion battery with high volumetric energy density. *Nat. Commun.* **6**, 7393 (2015).

154. Bitterlich, B., Lutz, C. & Roosen, A. Rheological characterization of water-based slurries for the tape casting process. *Ceram. Int.* **28**, 675–683 (2002).

155. Cherrington, R. & Liang, J. 2 - Materials and Deposition Processes for Multifunctionality. in *Design and Manufacture of Plastic Components for Multifunctionality* (eds. Goodship, V., Middleton, B. & Cherrington, R.) 19–51 (William Andrew Publishing, 2016). doi:10.1016/B978-0-323-34061-8.00002-8.

156. Li, A., Hempel, J. L., Balogh, M. P., Cheng, Y.-T. & Taub, A. I. Effect of Binder Content on Silicon Microparticle Anodes for Lithium-Ion Batteries. *J. Electrochem. Soc.* **170**, 010533 (2023).

157. Grady, M. E., Geubelle, P. H. & Sottos, N. R. Interfacial adhesion of photodefinable polyimide films on passivated silicon. *Thin Solid Films* **552**, 116–123 (2014).

158. Delvigs, P. Graphite/polyimide composites with improved toughness. *Polym. Compos.* **10**, 134–139 (1989).

159. Kim, Y.-H., Walker, G. F., Kim, J. & Park, J. Adhesion and interface studies between copper and polyimide. *J. Adhes. Sci. Technol.* **1**, 331–339 (1987).

160. Lu, X. *et al.* Microstructural Evolution of Battery Electrodes During Calendering. *Joule* **4**, 2746–2768 (2020).

161. Abdollahifar, M. *et al.* Insights into Influencing Electrode Calendering on the Battery Performance. *Adv. Energy Mater.* **n/a**, 2300973.

162. Ebner, M., Chung, D.-W., García, R. E. & Wood, V. Tortuosity Anisotropy in Lithium-Ion Battery Electrodes. *Adv. Energy Mater.* **4**, 1301278 (2014).

163. Mutlay, İ. & Tudoran, L. B. Percolation Behavior of Electrically Conductive Graphene Nanoplatelets/Polymer Nanocomposites: Theory and Experiment. *Fuller. Nanotub. Carbon Nanostructures* **22**, 413–433 (2014).

164. Li, J. & Kim, J.-K. Percolation threshold of conducting polymer composites containing 3D randomly distributed graphite nanoplatelets. *Compos. Sci. Technol.* **67**, 2114–2120 (2007).

165. Ehrl, A., Landesfeind, J., Wall, W. A. & Gasteiger, H. A. Determination of Transport Parameters in Liquid Binary Lithium Ion Battery Electrolytes. *J. Electrochem. Soc.* **164**, A826 (2017).

166. Martin, W., Tian, Y. & Xiao, J. Understanding Diffusion and Electrochemical Reduction of Li+ Ions in Liquid Lithium Metal Batteries. *J. Electrochem. Soc.* **168**, 060513 (2021).

167. Li, J., Xiao, X., Yang, F., Verbrugge, M. W. & Cheng, Y.-T. Potentiostatic Intermittent Titration Technique for Electrodes Governed by Diffusion and Interfacial Reaction. *J. Phys. Chem. C* **116**, 1472–1478 (2012).

168. Miao, J. & Thompson, C. V. Kinetic Study of the Initial Lithiation of Amorphous Silicon Thin Film Anodes. *J. Electrochem. Soc.* **165**, A650 (2018).

169. Ding, N. *et al.* Determination of the diffusion coefficient of lithium ions in nano-Si. *Solid State Ion.* **180**, 222–225 (2009).

170. Xie, J. *et al.* Li-ion diffusion in amorphous Si films prepared by RF magnetron sputtering: A comparison of using liquid and polymer electrolytes. *Mater. Chem. Phys.* **120**, 421–425 (2010).

171. Newman, J. & Balsara, N. P. *Electrochemical Systems*. (John Wiley & Sons, Incorporated, 2021).

172. Landesfeind, J., Hattendorff, J., Ehrl, A., Wall, W. A. & Gasteiger, H. A. Tortuosity Determination of Battery Electrodes and Separators by Impedance Spectroscopy. *J. Electrochem. Soc.* **163**, A1373 (2016).

173. Limthongkul, P., Jang, Y.-I., Dudney, N. J. & Chiang, Y.-M. Electrochemically-driven solid-state amorphization in lithium-silicon alloys and implications for lithium storage. *Acta Mater.* **51**, 1103–1113 (2003).

174. Obrovac, M. N. & Krause, L. J. Reversible Cycling of Crystalline Silicon Powder. *J. Electrochem. Soc.* **154**, A103 (2006).

175. Wang, Y. *et al.* Effects of polymeric binders on the cracking behavior of silicon composite electrodes during electrochemical cycling. *J. Power Sources* **438**, 226938 (2019).

176. Oumellal, Y. *et al.* The failure mechanism of nano-sized Si-based negative electrodes for lithium ion batteries. *J. Mater. Chem.* **21**, 6201–6208 (2011).

177. Haufe, S., Bernhard, R. & Pfeiffer, J. Revealing the Failure Mechanism of Partially Lithiated Silicon-Dominant Anodes Based on Microscale Silicon Particles. *J. Electrochem. Soc.* **168**, 080531 (2021).

178. Schweidler, S. *et al.* Volume Changes of Graphite Anodes Revisited: A Combined Operando X-ray Diffraction and In Situ Pressure Analysis Study. *J. Phys. Chem. C* **122**, 8829–8835 (2018).

179. Whittingham, M. S. Lithium Batteries and Cathode Materials. *Chem. Rev.* **104**, 4271–4302 (2004).

180. Zhuo, Z. *et al.* Breathing and oscillating growth of solid-electrolyte-interphase upon electrochemical cycling. *Chem. Commun.* **54**, 814–817 (2018).

181. Cao, C., Steinrück, H.-G., Shyam, B. & Toney, M. F. The Atomic Scale Electrochemical Lithiation and Delithiation Process of Silicon. *Adv. Mater. Interfaces* **4**, 1700771 (2017).

182. Miao, J., Wang, B. & Thompson, C. V. First-order amorphous-to-amorphous phase transitions during lithiation of silicon thin films. *Phys. Rev. Mater.* **4**, 043608 (2020).

183. Ohzuku, T., Matoba, N. & Sawai, K. Direct evidence on anomalous expansion of graphite-negative electrodes on first charge by dilatometry. *J. Power Sources* **97–98**, 73–77 (2001).

184. Veith, G. M. *et al.* Direct Determination of Solid-Electrolyte Interphase Thickness and Composition as a Function of State of Charge on a Silicon Anode. *J. Phys. Chem. C* **119**, 20339–20349 (2015).

185. Veith, G. M. *et al.* Determination of the Solid Electrolyte Interphase Structure Grown on a Silicon Electrode Using a Fluoroethylene Carbonate Additive. *Sci. Rep.* **7**, 6326 (2017).

186. Stetson, C. *et al.* Evolution of solid electrolyte interphase and active material in the silicon wafer model system. *J. Power Sources* **482**, 228946 (2021).

187. Yu, H. *et al.* High-energy 'composite' layered manganese-rich cathode materials via controlling Li2MnO3 phase activation for lithium-ion batteries. *Phys. Chem. Chem. Phys.* **14**, 6584–6595 (2012).

188. Wang, C. *et al.* Direct observation of chemomechanical stress-induced phase transformation in high-Ni layered cathodes for lithium-ion batteries. *Matter* **6**, 1265–1277 (2023).

189. Xu, B., Qian, D., Wang, Z. & Meng, Y. S. Recent progress in cathode materials research for advanced lithium ion batteries. *Mater. Sci. Eng. R Rep.* **73**, 51–65 (2012).

190. Chen, K.-H. *et al.* Dead lithium: mass transport effects on voltage, capacity, and failure of lithium metal anodes. *J. Mater. Chem. A* **5**, 11671–11681 (2017).

191. Choi, Y. H. *et al.* Development of Standardized Battery Pack for Next-Generation PHEVs in Considering the Effect of External Pressure on Lithium-Ion Pouch Cells. *SAE Int. J. Altern. Powertrains* **7**, 195–206 (2018).

192. Masias, A., Marcicki, J. & Paxton, W. A. Opportunities and Challenges of Lithium Ion Batteries in Automotive Applications. *ACS Energy Lett.* **6**, 621–630 (2021).

193. Choi, J. W. & Aurbach, D. Promise and reality of post-lithium-ion batteries with high energy densities. *Nat. Rev. Mater.* **1**, 1–16 (2016).

194. Liu, Y.-T., Liu, S., Li, G.-R. & Gao, X.-P. Strategy of Enhancing the Volumetric Energy Density for Lithium–Sulfur Batteries. *Adv. Mater.* **33**, 2003955 (2021).

195. Wang, X. *et al.* Understanding Volume Change in Lithium-Ion Cells during Charging and Discharging Using In Situ Measurements. *J. Electrochem. Soc.* **154**, A14 (2006).

196. Freunberger, S. A. True performance metrics in beyond-intercalation batteries. *Nat. Energy* **2**, 1–4 (2017).

197. Cannarella, J. & Arnold, C. B. State of health and charge measurements in lithium-ion batteries using mechanical stress. *J. Power Sources* **269**, 7–14 (2014).

198. Bitzer, B. & Gruhle, A. A new method for detecting lithium plating by measuring the cell thickness. *J. Power Sources* **262**, 297–302 (2014).

199. Berckmans, G. *et al.* Cost Projection of State of the Art Lithium-Ion Batteries for Electric Vehicles Up to 2030. *Energies* **10**, 1314 (2017).

200. Schmuch, R., Wagner, R., Hörpel, G., Placke, T. & Winter, M. Performance and cost of materials for lithium-based rechargeable automotive batteries. *Nat. Energy* **3**, 267–278 (2018).

201. Beaulieu, L. Y., Beattie, S. D., Hatchard, T. D. & Dahn, J. R. The Electrochemical Reaction of Lithium with Tin Studied By In Situ AFM. *J. Electrochem. Soc.* **150**, A419 (2003).

202. Kushima, A., Huang, J. Y. & Li, J. Quantitative Fracture Strength and Plasticity Measurements of Lithiated Silicon Nanowires by In Situ TEM Tensile Experiments. *ACS Nano* **6**, 9425–9432 (2012).

203. Pharr, M., Suo, Z. & Vlassak, J. J. Measurements of the Fracture Energy of Lithiated Silicon Electrodes of Li-Ion Batteries. *Nano Lett.* **13**, 5570–5577 (2013).

204. Wu, H. & Cui, Y. Designing nanostructured Si anodes for high energy lithium ion batteries. *Nano Today* **7**, 414–429 (2012).

205. Jain, R. *et al.* Nanostructuring versus microstructuring in battery electrodes. *Nat. Rev. Mater.* **7**, 736–746 (2022).

206. Zhao, Z. *et al.* Liquid Metal Remedies Silicon Microparticulates Toward Highly Stable and Superior Volumetric Lithium Storage. *Adv. Energy Mater.* **12**, 2103565 (2022).

207. Highly elastic binders integrating polyrotaxanes for silicon microparticle anodes in lithium ion batteries. https://www.science.org/doi/10.1126/science.aal4373 doi:10.1126/science.aal4373.

208. Yoon, D.-H., Marinaro, M., Axmann, P. & Wohlfahrt-Mehrens, M. Study of the Binder Influence on Expansion/Contraction Behavior of Silicon Alloy Negative Electrodes for Lithium-Ion Batteries. *J. Electrochem. Soc.* **167**, 160537 (2020).

209. Park, H.-I., Park, Y. K., Kim, S. K., Jang, H. D. & Kim, H. Hollow Graphene as an Expansion-Inhibiting Electrical Interconnector for Silicon Electrodes in Lithium-Ion Batteries. *ACS Appl. Mater. Interfaces* **13**, 35759–35766 (2021).

210. Yoon, I., Abraham, D. P., Lucht, B. L., Bower, A. F. & Guduru, P. R. In Situ Measurement of Solid Electrolyte Interphase Evolution on Silicon Anodes Using Atomic Force Microscopy. *Adv. Energy Mater.* **6**, 1600099 (2016).

211. Xu, K. Nonaqueous liquid electrolytes for lithium-based rechargeable batteries. *Chem. Rev.* **104**, 4303–4417 (2004).

212. Fong, R., Sacken, U. von & Dahn, J. R. Studies of Lithium Intercalation into Carbons Using Nonaqueous Electrochemical Cells. *J. Electrochem. Soc.* **137**, 2009 (1990).

213. Zhao, E., Gu, Y., Fang, S., Yang, L. & Hirano, S. Systematic Investigation of Electrochemical Performances for Lithium-Ion Batteries with Si/Graphite Anodes: Effect of Electrolytes Based on Fluoroethylene Carbonate and Linear Carbonates. *ACS Appl. Energy Mater.* **4**, 2419–2429 (2021).

214. Ha, Y. *et al.* Evaluating the Effect of Electrolyte Additive Functionalities on NMC622/Si Cell Performance. *J. Electrochem. Soc.* **169**, 070515 (2022).

215. Xu, C. *et al.* Improved Performance of the Silicon Anode for Li-Ion Batteries: Understanding the Surface Modification Mechanism of Fluoroethylene Carbonate as an Effective Electrolyte Additive. *Chem. Mater.* **27**, 2591–2599 (2015).

216. Michan, A. L. *et al.* Fluoroethylene Carbonate and Vinylene Carbonate Reduction: Understanding Lithium-Ion Battery Electrolyte Additives and Solid Electrolyte Interphase Formation. *Chem. Mater.* **28**, 8149–8159 (2016).

217. Kim, J., Chae, O. B. & Lucht, B. L. Perspective—Structure and Stability of the Solid Electrolyte Interphase on Silicon Anodes of Lithium-ion Batteries. *J. Electrochem. Soc.* **168**, 030521 (2021).

218. Nguyen, C. C. & Lucht, B. L. Comparative Study of Fluoroethylene Carbonate and Vinylene Carbonate for Silicon Anodes in Lithium Ion Batteries. *J. Electrochem. Soc.* **161**, A1933 (2014).

219. Jin, Y. *et al.* Understanding Fluoroethylene Carbonate and Vinylene Carbonate Based Electrolytes for Si Anodes in Lithium Ion Batteries with NMR Spectroscopy. *J. Am. Chem. Soc.* **140**, 9854–9867 (2018).

220. Yoon, I., Jurng, S., Abraham, D. P., Lucht, B. L. & Guduru, P. R. Measurement of mechanical and fracture properties of solid electrolyte interphase on lithium metal anodes in lithium ion batteries. *Energy Storage Mater.* **25**, 296–304 (2020).

221. Jung, R. *et al.* Consumption of Fluoroethylene Carbonate (FEC) on Si-C Composite Electrodes for Li-Ion Batteries. *J. Electrochem. Soc.* **163**, A1705 (2016).

222. Wetjen, M. *et al.* Differentiating the Degradation Phenomena in Silicon-Graphite Electrodes for Lithium-Ion Batteries. *J. Electrochem. Soc.* **164**, A2840–A2852 (2017).

223. Xu, K. Electrolytes and Interphases in Li-Ion Batteries and Beyond. *Chem. Rev.* **114**, 11503–11618 (2014).

224. Rynearson, L., Rodrigo, N. D., Jayawardana, C. & Lucht, B. L. Electrolytes Containing Triethyl Phosphate Solubilized Lithium Nitrate for Improved Silicon Anode Performance. *J. Electrochem. Soc.* **169**, 040537 (2022).

225. Shui Zhang, S. An unique lithium salt for the improved electrolyte of Li-ion battery. *Electrochem. Commun.* **8**, 1423–1428 (2006).

226. Chen, Z., Liu, J. & Amine, K. Lithium Difluoro(oxalato)borate as Salt for Lithium-Ion Batteries. *Electrochem. Solid-State Lett.* **10**, A45 (2006).

227. Benning, S., Chen, C., Eichel, R.-A., Notten, P. H. L. & Hausen, F. Direct Observation of SEI Formation and Lithiation in Thin-Film Silicon Electrodes via in Situ Electrochemical Atomic Force Microscopy. *ACS Appl. Energy Mater.* **2**, 6761–6767 (2019).

228. Wetjen, M. *et al.* Morphological Changes of Silicon Nanoparticles and the Influence of Cutoff Potentials in Silicon-Graphite Electrodes. *J. Electrochem. Soc.* **165**, A1503–A1514 (2018).

229. Kasnatscheew, J. *et al.* A Tutorial into Practical Capacity and Mass Balancing of Lithium Ion Batteries. *J. Electrochem. Soc.* **164**, A2479 (2017).

230. Li, D. *et al.* In situ measurement of mechanical property and stress evolution in a composite silicon electrode. *J. Power Sources* **366**, 80–85 (2017).

231. Verbrugge, M. *et al.* Fabrication and Characterization of Lithium-Silicon Thick-Film Electrodes for High-Energy-Density Batteries. *J. Electrochem. Soc.* **164**, A156 (2016).

232. Wilkinson, D. P. & Wainwright, D. In-situ study of electrode stack growth in rechargeable cells at constant pressure. *J. Electroanal. Chem.* **355**, 193–203 (1993).

233. Arisetty, S., Jimenez, N. & Raghunathan, K. In Situ Thickness Measurements During Cycling of Li-Ion Pouch Cells with Silicon Negative Electrodes. *J. Electrochem. Soc.* **169**, 080515 (2022).

234. Pegel, H. *et al.* Volume and thickness change of NMC811|SiOx-graphite large-format lithium-ion cells: from pouch cell to active material level. *J. Power Sources* **537**, 231443 (2022).

235. Louli, A. J., Ellis, L. D. & Dahn, J. R. Operando Pressure Measurements Reveal Solid Electrolyte Interphase Growth to Rank Li-Ion Cell Performance. *Joule* **3**, 745–761 (2019).

236. Leung, P. K. *et al.* Real-time displacement and strain mappings of lithium-ion batteries using three-dimensional digital image correlation. *J. Power Sources* **271**, 82–86 (2014).

237. Luo, J. *et al.* In-situ measurements of mechanical and volume change of LiCoO2 lithium-ion batteries during repeated charge–discharge cycling by using digital image correlation. *Measurement* **94**, 759–770 (2016).

238. Rieger, B. *et al.* Multi-scale investigation of thickness changes in a commercial pouch type lithium-ion battery. *J. Energy Storage* **6**, 213–221 (2016).

239. A Practical Guide for Using Electrochemical Dilatometry as Operando Tool in Battery and Supercapacitor Research - Escher - 2022 - Energy Technology - Wiley Online Library. https://onlinelibrary-wiley-com.proxy.lib.umich.edu/doi/full/10.1002/ente.202101120.

240. Prado, A. Y. R., Rodrigues, M.-T. F., Trask, S. E., Shaw, L. & Abraham, D. P. Electrochemical Dilatometry of Si-Bearing Electrodes: Dimensional Changes and Experiment Design. *J. Electrochem. Soc.* **167**, 160551 (2020).

241. Li, M., Wang, Z., Fu, J., Ma, K. & Detsi, E. In situ electrochemical dilatometry study of capacity fading in nanoporous Ge-based Na-ion battery anodes. *Scr. Mater.* **164**, 52–56 (2019).

242. Lohrberg, O., Maletti, S., Heubner, C., Schneider, M. & Michaelis, A. Understanding Li Plating and Stripping Behavior in Zero-Excess Li Metal Batteries Using Operando Dilatometry. *J. Electrochem. Soc.* **169**, 030543 (2022).

243. Jimenez, N. P., Balogh, M. P. & Halalay, I. C. High Porosity Single-Phase Silicon Negative Electrode Made with Phase-Inversion. *J. Electrochem. Soc.* **168**, 040507 (2021).

244. Qian, J., Wiener, C. G., Zhu, Y. & Vogt, B. D. Swelling and plasticization of polymeric binders by Li-containing carbonate electrolytes using quartz crystal microbalance with dissipation. *Polymer* **143**, 237–244 (2018).

245. Wang, Y. *et al.* Mechanical Property Evolution of Silicon Composite Electrodes Studied by Environmental Nanoindentation. *Adv. Energy Mater.* **8**, 1702578 (2018).

246. Wetjen, M. *et al.* Morphological Changes of Silicon Nanoparticles and the Influence of Cutoff Potentials in Silicon-Graphite Electrodes. *J. Electrochem. Soc.* **165**, A1503 (2018).

247. Li, J., Yang, F., Xiao, X., Verbrugge, M. W. & Cheng, Y.-T. Potentiostatic intermittent titration technique (PITT) for spherical particles with finite interfacial kinetics. *Electrochimica Acta* **75**, 56–61 (2012).

248. Yu, P., Popov, B. N., Ritter, J. A. & White, R. E. Determination of the Lithium Ion Diffusion Coefficient in Graphite. *J. Electrochem. Soc.* **146**, 8 (1999).

249. Takami, N., Hoshina, K. & Inagaki, H. Lithium Diffusion in Li4/3Ti5/3O4 Particles during Insertion and Extraction. *J. Electrochem. Soc.* **158**, A725 (2011).

250. Min, J., Gubow, L. M., Hargrave, R. J., Siegel, J. B. & Li, Y. Direct measurements of size-independent lithium diffusion and reaction times in individual polycrystalline battery particles. *Energy Environ. Sci.* (2023) doi:10.1039/D3EE00953J.

251. Cui, S. *et al.* Optimized Temperature Effect of Li-Ion Diffusion with Layer Distance in Li(NixMnyCoz)O2 Cathode Materials for High Performance Li-Ion Battery. *Adv. Energy Mater.* **6**, 1501309 (2016).

252. Tang, S. B., Lai, M. O. & Lu, L. Li-ion diffusion in highly (003) oriented LiCoO2 thin film cathode prepared by pulsed laser deposition. *J. Alloys Compd.* **449**, 300–303 (2008).

253. Prosini, P. P., Lisi, M., Zane, D. & Pasquali, M. Determination of the chemical diffusion coefficient of lithium in LiFePO4. *Solid State Ion.* **148**, 45–51 (2002).

254. Balke, N. *et al.* Nanoscale mapping of ion diffusion in a lithium-ion battery cathode. *Nat. Nanotechnol.* **5**, 749–754 (2010).

255. Guan, P., Liu, L. & Lin, X. Simulation and Experiment on Solid Electrolyte Interphase (SEI) Morphology Evolution and Lithium-Ion Diffusion. *J. Electrochem. Soc.* **162**, A1798 (2015).

256. Wu, B. *et al.* Influence of the SEI Formation on the Stability and Lithium Diffusion in Si Electrodes. *ACS Omega* **7**, 32740–32748 (2022).

257. Hollricher, O., Schmidt, U. & Breuninger, S. RISE Microscopy: Correlative Raman-SEM Imaging. *Microsc. Today* **22**, 36–39 (2014).

258. Zeng, Z. *et al.* In situ measurement of lithiation-induced stress in silicon nanoparticles using micro-Raman spectroscopy. *Nano Energy* **22**, 105–110 (2016).